JETP Letters, Vol. 80, No. 5, 2004, pp. 293–297. Translated from Pis'ma v Zhurnal Éksperimental'noĭ i Teoreticheskoĭ Fiziki, Vol. 80, No. 5, 2004, pp. 339–343.

Linear and Nonlinear Optical Spectroscopy of Gadolinium Iron Borate $GdFe_3(BO_3)_4$

A. M. Kalashnikova[1, *], V. V. Pavlov[1], R. V. Pisarev[1], L. N. Bezmaternykh[2], M. Bayer[3], and Th. Rasing[4]

[1] *Ioffe Physicotechnical Institute, Russian Academy of Sciences, St. Petersburg, 194021 Russia*
**e-mail: kalashnikova@mail.ioffe.ru*
[2] *Institute of Physics, Siberian Division, Russian Academy of Sciences, Krasnoyarsk, 660036 Russia*
[3] *Experimental Physics II, Dortmund University, Dortmund, 44227 Germany*
[4] *NSRIM Institute, University of Nijmegen, 6525 the Netherlands*

Received July 20, 2004

The optical spectra and the second-harmonic generation (SHG) are studied in a noncentrosymmetric $GdFe_3(BO_3)_4$ magnet. In the region of weak absorption ($\alpha \sim 20$–400 cm^{-1}) below ~3 eV, three absorption bands are distinguished, which can be unambiguously assigned to forbidden electronic transitions from the ground $^6A_1$ state of the Fe^{3+} ion to its excited states $^4T_1$ (~1.4 eV), $^4T_2$ (~2 eV), and $^4A_1$, ^4E (~2.8 eV). Intense absorption begins in the region above 3 eV ($\alpha \sim 2$–4×10^5 cm^{-1}), where two bands at ~4.0 and 4.8 eV are observed, which are caused by allowed electric dipole charge-transfer transitions. The spectral features of SHG in the 1.2–3.0-eV region are explained by a change in the SHG efficiency caused by a change in the phase mismatch. It is shown that in the weak absorption region, phase matching can be achieved for SHG. © *2004 MAIK "Nauka/Interperiodica".*

PACS numbers: 42.65.Ky; 71.20.Eh; 78.20.Ci; 78.20.Hp

Substances and structures in which several subsystems with different order parameters can be distinguished have attracted attention since the 1960s and are called multiferroics [1–4]. These parameters can be spontaneous magnetization and antiferromagnetic vector in magnets, spontaneous electric polarization in ferroelectrics, spontaneous deformation in ferroelastics, etc. In multiferroics, interaction between subsystems is possible when certain spatial and temporal symmetry conditions are fulfilled. Cross-interactions in multiferroics open up new possibilities for the development of devices based on the mutual control of magnetic, electric, and deformation states. Initial attempts to develop competitive devices proved to be unsuccessful due to the weakness of the interactions observed. However, quite recently several studies were reported that demonstrated a revival of interest in multiferroics. Materials and multiphase heterostructures with "giant" effects were synthesized [5–10], which opens up the outlook for applications of multiferroics in information systems as sensors and in spintronic devices.

Rare-earth iron borates with the general formula $RFe_3(BO_3)_4$, where R is a rare-earth element, are characterized by an unusual combination of a number of physical properties and can be assigned, according to some of these properties, to multiferroics. They are crystallized into the trigonal huntite structure described by the noncentrosymmetric space group R32 (no. 155) with three formula units in the unit cell, $Z = 3$ [11]. Note that crystals with the huntite structure have the same point group 32, as crystalline quartz but, of course, differ from quartz in their chemical composition and, hence, in their physical properties. A change in temperature induces structural and magnetic phase transitions in iron borates, but their character is not clear at present in most cases [11–14]. Magnetic ordering can, in principle, occur both in the iron and rare-earth sublattices, and these sublattices also determine the optical properties of rare-earth iron borates.

Trivalent Fe^{3+} ions in the $RFe_3(BO_3)_4$ crystal structure occupy the 9*d* octahedral sites with the local symmetry *2*, which form one-dimensional (1D) helicoid chains extended along the trigonal axis [11]. The octahedral sites of the Fe^{3+} ion are typical of many other oxide iron compounds including, for example, centrosymmetric iron borate $FeBO_3$, rare-earth orthoferrites $RFeO_3$, and ferrite garnets $R_3Fe_5O_{12}$. However, a significant difference between the crystalline structures of huntite and these materials, and especially the noncentrosymmetric arrangement of magnetic ion sites and the noncentrosymmetric structure of huntite itself should result in a number of substantial differences between the optical properties of rare-earth iron borates and the oxides of trivalent iron studied earlier. Note that, in the huntite structure, as in quartz, the second-harmonic generation (SHG) is allowed in the electric dipole approximation [15]. For the point group 32, the $yyy = -xxy = -xyx = -yxx$, $xyz = -yzx$, and $xzy = -yzx$

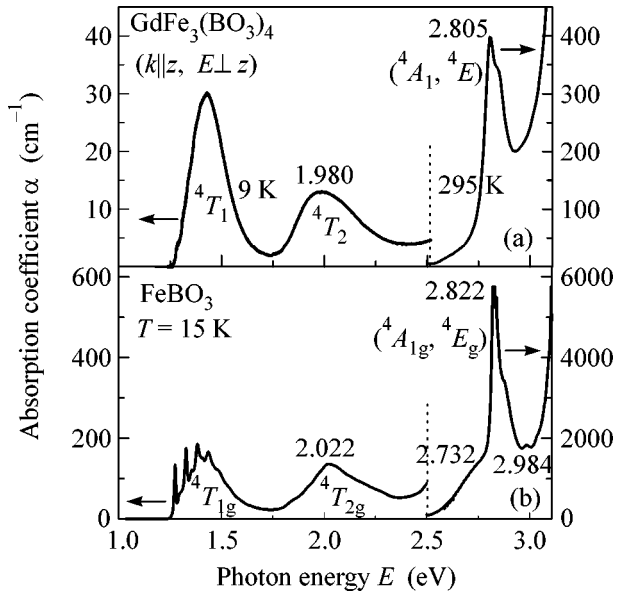

Fig. 1. Absorption spectra of (a) gadolinium iron borate $GdFe_3(BO_3)_4$ at T = 9 and 295 K and (b) iron borate $FeBO_3$ at T = 15 K.

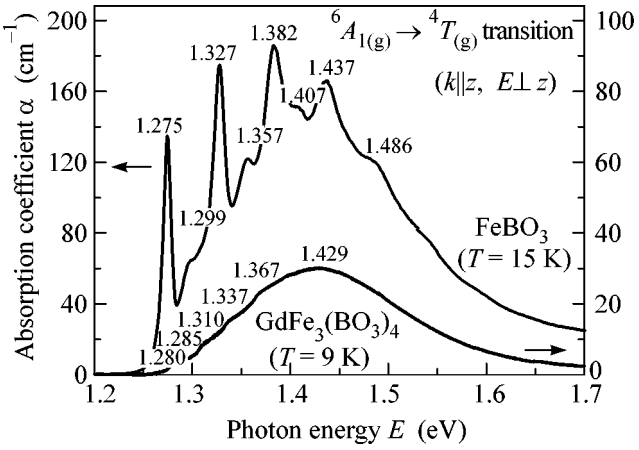

Fig. 2. Absorption spectra of $GdFe_3(BO_3)_4$ and $FeBO_3$ at the ${}^6A_1({}^4A_{1g}) \longrightarrow {}^4T_1({}^4T_{1g})$ transition.

components of the susceptibility $\chi_{ijk}(2\omega)$ of the second harmonic are nonzero [3].

In this paper, we report a comparative study of optical absorption, birefringence, and SHG in gadolinium iron borate $GdFe_3(BO_3)_4$. We also present the results of the ellipsometric study of this material in the region between 0.6 and 5.4 eV, performed in the reflection geometry. This allowed us to determine the dispersion of the main optical parameters in a broad spectral range. The results obtained suggest that it is possible to produce phase matching for SHG in this magnetic material, which, as far as we know, was not investigated earlier for other magnetic materials [16].

The $GdFe_3(BO_3)_4$ single crystals were grown by the method described in [13]. Optical studies were performed with plane-parallel oriented plates of thickness from 0.1 to 1.0 mm. The absorption spectra were recorded using a Cary 2300 spectrophotometer and a Spex monochromator. The SHG spectra were studied in the transmission geometry at the normal incidence of the fundamental radiation on a sample. The method described in [17] was used. The ellipsometric study was performed using an ellipsometer at several angles of the incidence of light on a sample, which allowed us to determine with good accuracy the ordinary and extraordinary refractive indices n_o and n_e, the absorption coefficients k_o and k_e, and the birefringence $\Delta n = n_o - n_e$.

The linear absorption spectra of gadolinium iron borate and iron borate are shown in Fig. 1. They are qualitatively similar on the whole. Absorption in the region below 3.0 eV is comparatively weak, and it was studied in the transmission geometry along the optical axis. In this region three absorption bands are observed, which correspond to the electronic transitions between the $(3d)^5$ states of the shell of the Fe^{3+} ion in the octahedral crystal field produced by oxygen O^{2-} ions [18]. Because the transitions from the ${}^6A_1$ ground state to the excited ${}^4T_1$ and ${}^4T_2$ states and the degenerate $({}^4A_1, {}^4E)$ state are forbidden by the spin-selection rules, the intensity of the corresponding absorption bands is comparatively low. Moreover, the intensity of these transitions in $GdFe_3(BO_3)_4$ is substantially lower than in $FeBO_3$ and other trivalent iron oxides. Figure 2 shows the absorption spectra in the region of the first ${}^6A_1 \longrightarrow {}^4T_1$ transition for gadolinium iron borate and $FeBO_3$. The Fe^{3+} ion in both these materials is located in the octahedral environment consisting of six O^{2-} ions, which produce a crystal field and cause the splitting of the degenerate states of a free ion. In our case, this is the ${}^4G$ state [18]. The Fe–O bond lengths in these compounds are close and are 2.028 Å in $FeBO_3$ [19] and 2.026(2) Å, 2.044(2) Å, and 1.950(2) Å (the average bond length is 2.007 Å) in $GdFe_3(BO_3)_4$ [11]. The values of the parameter $10Dq$ of the cubic crystal field are also close, as was confirmed by the coincidence of the positions of the absorption bands of these compounds with an accuracy of 1–2%. Two observations are surprising: (i) the absence of the fine structure in the region of the first transition in gadolinium iron borate. We cannot yet explain this unexpected fact; and (ii) a substantial decrease in the intensity of absorption bands in gadolinium iron borate by approximately a factor of six for the first transition, by a factor of ten for the second transition, and by a factor of fifteen for the third transition, although, unlike $FeBO_3$, the Fe^{3+} ion in this iron borate is located in the noncentrosymmetric environment. The difference between the absorption-band intensities increases in the approach to the fundamental absorption edge determined by the allowed transitions. Even more illustrative is a comparison of iron borates with orthof-

errites $R\mathrm{FeO}_3$, in which the Fe–O bonds vary from 2.006 to 2.014 Å [20]. According to our measurements, the maximum absorption coefficient for the first transition in orthoferrites is $\alpha \simeq 400\ \mathrm{cm}^{-1}$.

One can see from Fig. 3b that absorption above 3.0 eV is stronger, and it should be assigned to the allowed electric dipole transitions. In oxides of 3*d* transition metals, these are charge-transfer transitions [21]. In the cluster model, this is the electron transfer from the oxygen ion to the iron ion, while in the band model, this is an electronic transition from the valence band formed predominantly by the oxygen 2*p* orbitals to the conduction band formed predominantly by the 3*d* orbitals. One can see from Fig. 3a that the observed transitions are polarized, resulting in the crystallographic birefringence $\Delta n = n_o - n_e$ and in linear dichroism $\Delta k = k_o - k_e$. In the relatively transparent region, $\Delta k \simeq 0$ and $\Delta n \simeq 0.1$; i.e., birefringence is rather strong, and the crystal is negative. Note for comparison that birefringence in crystal quartz in the visible region has the opposite sign and is on the order of $\Delta n \sim 0.06$–0.07 [22]; i.e., it is somewhat lower than in gadolinium iron borate.

In the region of intense absorption, two absorption bands are observed at ~4.0 and 4.8 eV. Let us compare these spectra with the spectra of other iron oxides. The intense absorption bands of FeBO_3 lie in the region from 3.38 to 3.75 eV [23], while in orthoferrites such bands are located, according to our data, at even lower energies, namely, 3.16, 3.9, and 4.4 eV. This redshift of the allowed electric dipole transitions qualitatively explains the increase in the intensity of the forbidden *d*–*d* transition in passing from gadolinium iron borate to FeBO_3 and orthoferrites, because forbidden transitions borrow the intensity of allowed transitions; the smaller their separation, the greater the degree of borrowing. Therefore, although the Fe–O bond lengths are almost the same in different materials and, hence, the local crystal fields are close, the optical properties of these materials can be substantially different. A significant difference between the spectra of iron borates and orthoferrites is already manifested in the fact that the former are transparent at a sample thickness of a few hundred micrometers in the green spectral region at 2.4 eV (see Fig. 1), while the latter are transparent only at thicknesses on the order of a hundred micrometers in the red spectral region at 2.0 eV [24]. In both cases, the absorption bands are caused by the transitions in the 3*d* shell of the Fe^{3+} ion in the region below ~3.0 eV and by the charge-transfer transitions at ~3.0 eV. In our opinion, the great difference in the absorption spectra of iron borates and orthoferrites is mainly explained by the difference in their crystal structures. The Fe–O–Fe bonds in orthoferrites form a three-dimensional network, whereas this bond in gadolinium iron borate, is in fact, one-dimensional and is realized only along the octahedral chains extended along the trigonal axis while the chains are not coupled to each other [11].

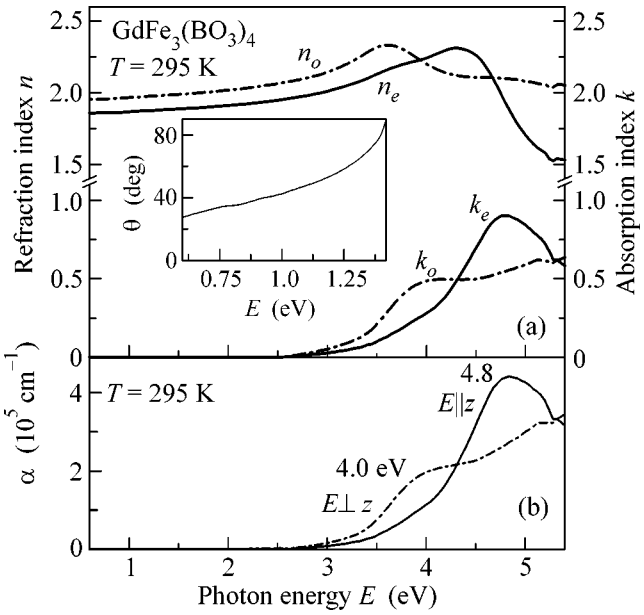

Fig. 3. (a) Dispersion of the ordinary (dot-and-dash curve) and extraordinary (solid curve) refractive indices and absorption coefficients of $GdFe_3(BO_3)_4$ at $T = 295$ K. Inset: dependence of the phase-matching angle θ on the pump energy. (b) Absorption spectra for light propagating along (dot-and-dash curve) and perpendicular to (solid curve) the optical axis.

It is known that most magnetic materials are centrosymmetric media, and SHG is forbidden in the electric dipole approximation. Nevertheless, SHG can be observed in magnetic materials with various centrosymmetric and noncentrosymmetric structures due to the break of the inversion center caused by magnetic ordering or the inclusion of magnetic dipole transitions into the three-photon process of harmonic generation [16]. Iron borates crystallize into the R32 noncentrosymmetric structure, and hence, SHG is allowed in the electric dipole approximation. We studied SHG in the transmission geometry, in which light propagated along the optical axis $\mathbf{k} \parallel z$ in a sample of thickness $t = 100$ μm. Figure 4 shows the SHG intensity $I_{2\omega}$ normalized to the squared fundamental radiation intensity I_ω^2. The inset in Fig. 4 shows the azimuthal dependence of the SHG intensity $I_{2\omega} \sim (\chi_{xxx} \cos 3\varphi)^2$, where φ is the angle between the crystal axes in the basal plane of a trigonal crystal and the polarization vector of the fundamental light wave. The results were obtained in the region of comparatively weak absorption. The SHG signal drastically decreases when absorption increases to $\alpha \simeq 400\ \mathrm{cm}^{-1}$ at the ${}^6A_1 \longrightarrow ({}^4A_1, {}^4E)$ transition (see Fig. 1) and then vanishes as absorption further increases in the region above ~3.0 eV.

The decrease in the SHG signal with increasing absorption is also explained by a change in the coherence length, which is predominantly determined in the

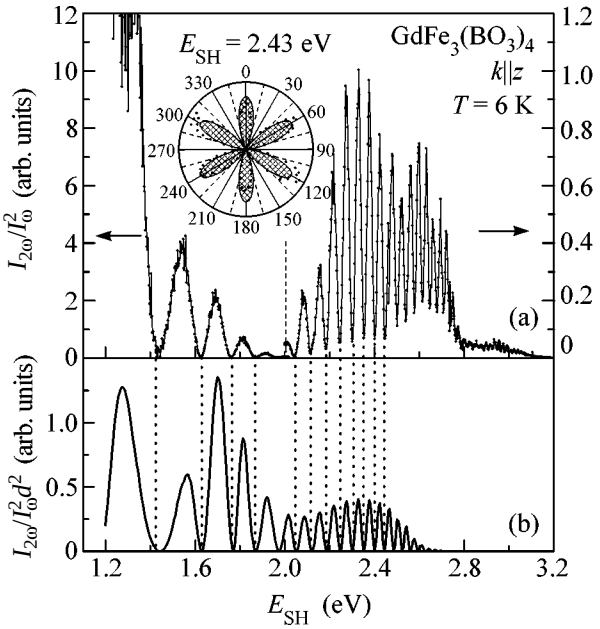

Fig. 4. (a) Spectral dependence of SHG in $GdFe_3(BO_3)_4$ at T = 6 K. Inset: azimuthal dependence of the SHG signal for the energy E_{SH} = 2.43 eV. (b) Spectral dependence of the SHG intensity calculated by expression (1).

transparency region by the dispersion of the refractive index and gradually decreases from ~15 to 0.9 μm in the region from 0.6 to 1.6 eV (from 1.2 to 3.2 eV for the second harmonic).

The oscillatory spectral dependence of the SHG intensity can be explained by the mechanism of Maker fringes observed upon changing the angle of incidence of fundamental radiation on a crystal [25, 26]. In our case, oscillations are caused by a change in the SHG efficiency that is not due to a change in the effective path length of light in the crystal but due rather to a change in the phase mismatch $\Delta\kappa = 2\kappa_\omega - \kappa_{2\omega}$ when the fundamental frequency varied, where $\kappa = n_\omega\omega/c$ is the wavenumber at the corresponding frequency. In this case, the dependence of the SHG intensity on the light frequency is described by the expression [15]

$$I_{2\omega} \sim \frac{d^2 I_\omega^2(2\omega)^2}{n_\omega^2 n_{2\omega}} L^2 \frac{\sin^2(\Delta\kappa L/2)}{(\Delta\kappa L/2)^2}, \qquad (1)$$

where $d_{ijk} = \frac{1}{2}\chi_{ijk}^{(2\omega)}$, and L is the crystal thickness. The function $I_{2\omega}/I_\omega^2 d^2$ calculated by expression (1) is presented in Fig. 4b. We also took into account in the calculation the absorption of the SHG signal. One can see from this figure that the periodicities of the experimental and calculated spectra coincide.

Figure 3a shows that $GdFe_3(BO_3)_4$ crystals have large birefringence $\Delta n \simeq 0.1$, allowing the realization of phase matching of the first type (*ooe*) in $GdFe_3(BO_3)_4$ for the efficient SHG. The inset in Fig. 3 presents the dependence of the phase-matching angle on the pump energy. In particular, the phase-matching angle for a pump energy of 1.17 eV from a Nd:YAG laser is $\theta \simeq 52°$. In our opinion, the above conclusion about the possibility of realizing phase matching in the magnetic material permits the extension of studies of the relation between the magnetic and nonlinear optical properties.

We thank H.-J. Weber and O. Schöps for their help in measuring the absorption spectra. This work was supported in part by the Russian Foundation for Basic Research, Deutsche Forschungsgemeinschaft, and the European program "Dynamics."

REFERENCES

1. *Magnetoelectric Interaction Phenomena in Crystals*, Ed. by A. J. Freeman and H. Schmid (Gordon and Breach, London, 1975).
2. G. A. Smolenskiĭ and I. E. Chupis, Usp. Fiz. Nauk **137**, 415 (1982) [Sov. Phys. Usp. **25**, 475 (1982)].
3. R. R. Birss, *Symmetry and Magnetism* (North-Holland, Amsterdam, 2000).
4. H. Schmid, *Magnetoelectric Effects in Insulating Magnetic Materials*, reprinted from *Introduction to Complex Mediums for Optics and Electromagnetics*, Ed. by W. S. Weigloger and A. Lakhtakia (SPIE Press, Bellingham, WA, 2003).
5. M. Fiebig, C. Degenhardt, and R. V. Pisarev, Phys. Rev. Lett. **88**, 027203 (2002).
6. T. Kimura, T. Goto, H. Shintani, *et al.*, Nature **429**, 392 (2004).
7. J. Wang, J. B. Neaton, H. Zheng, *et al.*, Science **299**, 1719 (2003).
8. Th. Lottermoser, Th. Lonkai, U. Amman, *et al.*, Nature **430**, 541 (2004).
9. G. Srinivasan, E. T. Rasmussen, B. J. Levin, and R. Hayes, Phys. Rev. B **65**, 134402 (2002).
10. C. W. Nan, L. Lin, N. Cai, *et al.*, Appl. Phys. Lett. **81**, 3831 (2002).
11. J. A. Campá, C. Cascales, E. Guitiérres-Puebla, *et al.*, Chem. Mater. **9**, 237 (1997).
12. Y. Hinatsu, Y. Doi, K. Ito, *et al.*, J. Solid State Chem. **172**, 438 (2003).
13. A. D. Balaev, L. N. Bezmaternykh, I. A. Gudim, *et al.*, J. Magn. Magn. Mater. **258–259**, 532 (2003).
14. R. Z. Levitin, E. A. Popova, R. M. Chtsherbov, *et al.*, Pis'ma Zh. Éksp. Teor. Fiz. **79**, 531 (2004) [JETP Lett. **79**, 423 (2004)].
15. R. W. Boyd, *Nonlinear Optics* (Academic, San Diego, 1992).
16. M. Fiebig, V. V. Pavlov, and R. V. Pisarev, J. Opt. Soc. Am. B (in press).
17. M. Fiebig, D. Fröhlich, St. Leute, and R. V. Pisarev, Appl. Phys. B **66**, 265 (1998).

18. A. B. P. Lever, *Inorganic Electronic Spectoscopy*, 2nd ed. (Elsevier, Amsterdam, 1984).
19. *Landolt–Börnstein, Numerical Data and Functional Relationships in Science and Technology* (Springer, Berlin, 1993), Group III, Vol. 27h.
20. M. Marezio, J. P. Remeika, and P. D. Derneir, Acta Crystallogr. B **26**, 2008 (1970).
21. A. I. Likhtenshteĭn, A. S. Moskvin, and V. A. Gubanov, Fiz. Tverd. Tela (Leningrad) **24**, 3596 (1982) [Sov. Phys. Solid State **24**, 2049 (1982)].
22. *Handbook on Physical Constants*, Ed. by I. S. Grigoriev and E. Z. Meĭlikhov (Énergoatomizdat, Moscow, 1991; CRC, Boca Raton, 1997).
23. A. V. Malakhovskii and I. S. Edelman, Phys. Status Solidi B **74**, K145 (1976).
24. F. J. Kahn, P. S. Pershan, and J. P. Remeika, Phys. Rev. **186**, 891 (1969).
25. P. D. Maker, R. W. Terhune, M. Nisenoff, and C. M. Savage, Phys. Rev. Lett. **8**, 21 (1962).
26. J. Jerphagnon and S. K. Kurtz, J. Appl. Phys. **41**, 1667 (1970).

Translated by M. Sapozhnikov

JETP Letters, Vol. 80, No. 5, 2004, pp. 298–302. Translated from Pis'ma v Zhurnal Éksperimental'noĭ i Teoreticheskoĭ Fiziki, Vol. 80, No. 5, 2004, pp. 344–348.

Shock-Wave Generation upon Axicon Focusing of Femtosecond Laser Radiation in Transparent Dielectrics

A. A. Babin, A. M. Kiselev, D. I. Kulagin, K. I. Pravdenko, and A. N. Stepanov*

Institute of Applied Physics, Russian Academy of Sciences, Nizhni Novgorod, 603950 Russia

**e-mail: step@ufp.appl.sci-nnov.ru*

Received July 15, 2004

It is shown experimentally that the axicon focusing of intense femtosecond laser pulses in transparent dielectrics leads to efficient excitation of shock waves. A method is developed for measuring the dynamics of shock waves, which uses a frequency-chirped probe pulse and has high spatial (~1 μm) and time (~10 ps) resolutions. The initial stage of the evolution of an intense (up to 10 GPa) shock wave is studied by this method. © *2004 MAIK "Nauka/Interperiodica".*

PACS numbers: 67.57.Lm; 76.60-k

One of the important features of the interaction of focused femtosecond laser pulses with matter is the possibility of a strong spatial localization of energy release in a material due to a minor role of heat conduction during the action of an ultrashort laser pulse. In addition, as the laser pulse is shortened, the energy density required to modify material is, as a rule, reduced [1, 2]. These properties are especially important for a number of applications, first of all for the precision laser machining of materials with micron and submicron accuracy. The interaction of an ultrashort laser pulse with condensed matter is almost always accompanied by shock-wave generation [3]. The study of the behavior of a material irradiated by a tightly focused laser beam poses the nontrivial problem of the observation of shock waves with high spatial (~1 μm) and time (~10 ps) resolutions. In this paper, we studied experimentally the dynamics of shock waves excited by intense femtosecond laser pulses focused by an axicon lens onto transparent dielectrics. For this purpose, we developed an original method to observe the shock-wave dynamics during a laser pulse with a high spatial resolution.

Figure 1 shows the scheme of our experimental setup for studying shock-wave generation. Shock waves were excited by ~100-fs, ~0.8-μm pulses from a Ti:sapphire laser [4] with a pulse repetition rate of 10 Hz. The femtosecond pulses were amplified using a standard scheme [5] in which a femtosecond pulse of a master oscillator is stretched in time, the obtained frequency-chirped pulse is amplified to the required energy, and then the amplified pulse is compressed in time. The laser pulse energy in our experiments did not exceed 10 mJ. The output laser beam of diameter d = 8 mm was directed on an axicon lens with the base angle $\beta = 20°$. It is known [6] that an axicon focuses a Gaussian radiation beam in a line directed along the axicon axis. The maximum radiation intensity on the axicon axis in our experiments was $I = (1–2) \times 10^{14}$ W/cm^2. A target made of a transparent dielectric [poly(methyl methacrylate) (PMMA)] was placed in the region of maximum radiation intensity and displaced from pulse to pulse in order to irradiate a given site of the target only by one laser pulse. It was shown earlier [7] that the axicon focusing of a femtosecond laser pulse produced a bright luminous filament inside a transparent dielectric, instead of which a long channel with a diameter of a few microns and a length of up to one centimeter remained after the end of the pulse. The luminous filament was interpreted as the formation of a plasma channel, which, as was shown, efficiently absorbs the laser pulse energy. Absorption of the laser radiation energy should result in the generation of an expanding cylindrical shock wave, which is studied in this paper.

We studied the dynamics of production of a plasma channel and shock-wave generation by the following method. A part of the frequency-chirped amplified laser pulse was deflected to provide for its temporal compression and passed, with a controllable delay, (perpendicular to the axicon axis) through the region where the

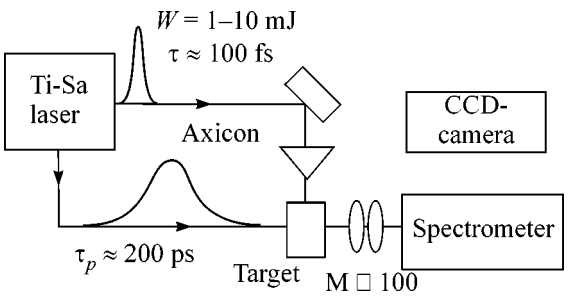

Fig. 1. Scheme of the experimental setup.

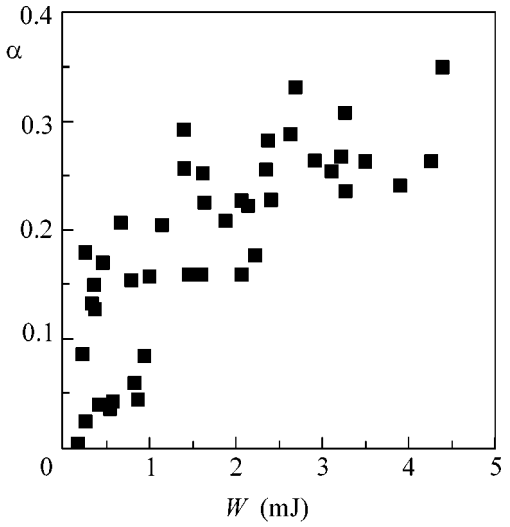

Fig. 2. Dependence of the fraction α of the femtosecond laser pulse energy absorbed in a PMMA sample on the pulse energy.

plasma channel was produced. The duration of the frequency-chirped probe pulse was $\tau_p \sim 200$ ps. Then, the probe pulse was projected with a ×100 magnification on the entrance slit of a spectrometer equipped with a 12-bit CCD camera (PCO, model Pixel Fly). Because the different wavelengths of the frequency-chirped pulse propagate through the interaction region at different instants of time, the horizontal axis in the spectrum at the exit slit of the spectrometer will be proportional to time (in the case of a linear frequency modulation), while the vertical axis corresponds to the spatial coordinate. Therefore, the spectrum displayed on the CCD monitor gives the spatiotemporal sweep of the transverse size of the region in which the plasma channel is produced, similarly to a picture obtained by means of a streak camera. The spatial resolution in our experiments was ~1 μm and was mainly determined by the numerical aperture of the microscope objective used to project the laser beam with magnification on the entrance slit of the spectrometer. The time resolution, determined by the spectral resolution of the spectrometer (by the entrance slit width providing the required signal level on the CCD camera), was ~10 ps. The energy of the incident femtosecond pulse and the pulse transmitted through a sample was measured with calibrated photodiodes.

As mentioned above, when some threshold intensity on the axicon axis was exceeded, a breakdown occurred in the target material, which was accompanied by the formation of a plasma channel. Figure 2 shows the fraction of the femtosecond pulse energy absorbed in the plasma channel as a function of the incident pulse energy. One can see that this fraction rapidly increases above the breakdown threshold, and already for $W \approx 4$ mJ, a significant fraction of the incident pulse energy (~30%) is absorbed in the plasma. Figure 3 demonstrates three spatiotemporal sweeps of the interaction region obtained on the CCD camera for three different delays of the probe pulse with respect to the intense femtosecond pulse producing the plasma channel (τ_d = 0, 0.5, and 1.0 ns). Each sweep was obtained during one laser pulse. The images in Fig. 3 were obtained by processing the initial frames to filter out a small-scale structure observed in the spatial distribution of the ×100-magnified probe pulse. The data were obtained for PMMA using ~2.5-mJ incident pulses. The first image ($\tau_d = 0$ s) demonstrates the channel formation. At the arrival time of the intense femtosecond pulse, the probe pulse is not absorbed. Then, after the end of the femtosecond pulse, absorption of radiation in the channel increases with a characteristic time of ~100–150 ps. The transverse size of the channel does not change on this time scale. The presence of weaker horizontal bands is caused by the finite aperture of the microscopic objective that was used to project the image on the entrance slit of the spectrometer [8]. The second image ($\tau_d = 0.5$ ns) shows the increase in the transverse size of the channel with time, which is caused by the expansion of the region of the material heated by the laser pulse into the surrounding unheated medium. Apart from the channel located at the central region, a second structure is observed, which has a greater transverse size and a diameter increasing in time—a shock wave expanding from the channel. For a large delay of the probe pulse (~2 ns), the channel diameter no longer increased, and the position of the shock-wave front became indiscernible. The channel size at large delays

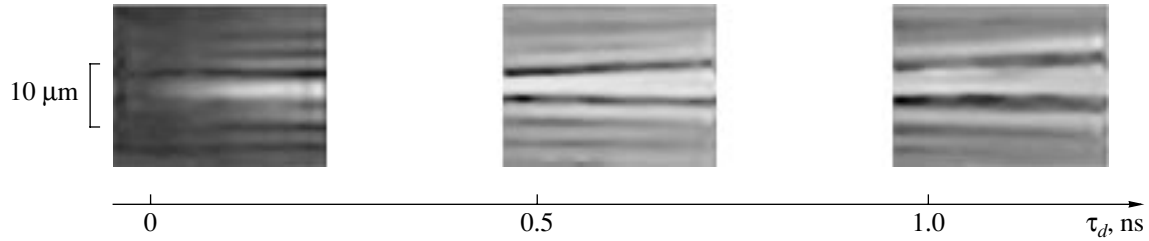

Fig. 3. Spatiotemporal sweeps of the image of the interaction region for different delays $\tau_d \approx 0$, 0.5, and 1.0 ns of the probe pulse with respect to the ~2.5-mJ femtosecond pulse.

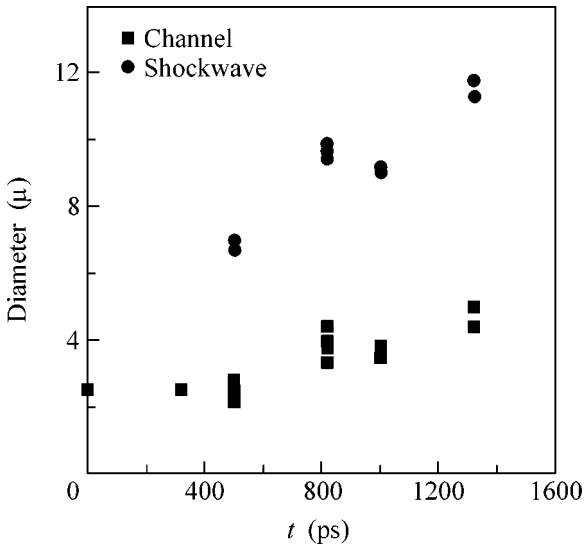

Fig. 4. Time dependences of the channel diameter and the shock-wave-front position. The pulse energy is ≈2–3 mJ.

corresponded to the channel size observed in the frames detected within a few seconds after the end of the intense femtosecond pulse.

Figure 4 shows the time dependences of the channel diameter and the position of the shock-wave front obtained from the CCD images discussed above. Note some specific features of these dependences: for $t <$ 0.5 ns, the channel diameter is independent of time. This is probably explained by the fact that the characteristic travel time of the acoustic perturbation is $t_s \sim r_k/c_s \sim 0.5$ ns (here, r_k is the channel radius and c_s is the sound speed in PMMA), i.e., is comparable to the channel size.

During the entire expansion time, the channel diameter approximately doubles, which results in the approximately four fold increase in the volume of the heated material (due to the cylindrical geometry of the experiment). Accordingly, the material density in the channel decreases by a factor of four after expansion. This probably indicates that PMMA (organic glass), which was initially a solid, decomposes upon heating caused by absorption of laser radiation energy by the plasma, and at least a part of the PMMA decomposition products are in a gas phase.

Our experimental method allows us to measure, in principle, both the velocity of material motion (via the dynamics of the channel diameter) and the shock-wave velocity during one laser pulse. This is sufficient for the construction of the shock adiabat of the material and the determination of its equations of state. The position of the shock-wave front was measured with an accuracy of ±15%; this value was mainly determined by aberrations appearing in the high-magnification imaging of small (a few microns) objects on the entrance slit of the spectrometer.

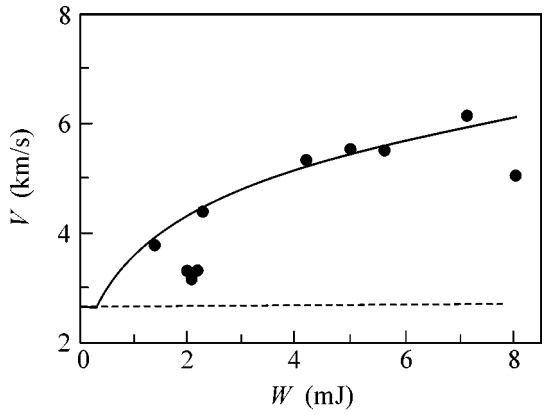

Fig. 5. Dependence of the shock-wave front velocity on the laser pulse energy. Circles are the experiment; the solid curve is the scaling for a cylindrical geometry; and the dashed straight line is the sound speed in PMMA.

Figure 5 shows the experimental dependence of the shock-wave velocity V on the energy of the femtosecond pulse producing the plasma channel. The dashed straight line in the figure indicates the sound speed in organic glass [9]. For the cylindrical geometry, the scaling of the shock-wave velocity with the absorbed energy has the form [10] $V \sim \sqrt[4]{\eta W}$, where η is the fraction of the absorbed energy (Fig. 2) and W is the laser pulse energy. This dependence is also presented in Fig. 5. By using the results of the shock-wave study in organic glass obtained in [11], we can find from the shock-wave velocity the dependence of pressure in the shock wave on the incident pulse energy (crosses in Fig. 6). One can see that this pressure rapidly increases

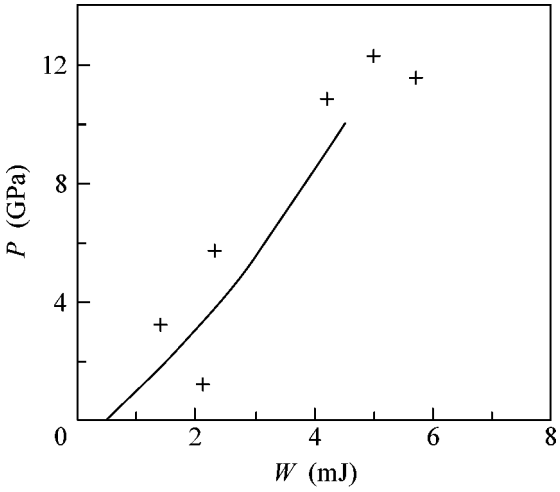

Fig. 6. Pressure inside the shock wave as a function of the laser pulse energy. Crosses are the estimate by the shock-wave velocity; the solid curve is the estimate of thermal pressure.

with the pulse energy and exceeds 10 GPa at maximum pulse energies. The shock wave is generated by the pressure produced by the heated target material in the plasma channel. The estimate of a thermal pressure, taking into account the measured absorbed energy of the incident pulse and using the ideal-gas model for the target material, is shown by the solid curve in Fig. 6. The estimate shows that the thermal pressure and pressure inside the shock wave are close to each other.

Consider now the dynamics of the increase in absorption of the probe pulse by the heated material in the plasma channel. Analysis of the images presented in Fig. 3 shows that, after the end of the femtosecond pulse producing the plasma channel, absorption gradually increases with a characteristic time of ~100–150 ps. This dependence can be interpreted in the following way. The plasma produced in the channel by the intense femtosecond pulse has, according to calculations [12], the concentration $n_e \approx 10^{19}$–10^{20} cm^{-3}, which should result in a noticeable absorption. However, the plasma lifetime is most likely to be much shorter than one picosecond [13]. Therefore, the time resolution of our experiments (~10 ps) does not allow us to detect absorption in the plasma. The observed increase of absorption with the characteristic time ~100–150 ps is probably determined by the decomposition of PMMA molecules due to their strong heating caused by absorption of the laser radiation energy, which is accompanied by the formation of strongly absorbing products of PMMA decomposition (carbonization of organic glass) [14]. The experimental data on the absorption dynamics give the dependence of the absorption increase rate in the plasma channel on the temperature of the material in the channel (Fig. 7). The material temperature was estimated by the fraction of the absorbed energy while taking the channel size into account. One can see from Fig. 7 that the absorption increase rate decreases with increasing material temperature. This result is somewhat unexpected because, if absorption is determined by the PMMA decomposition products, then, as is known from chemical kinetics [15], the concentration n of absorbing decomposition products should be described by the equation

$$dn/dt = N\nu^{-E/kT}, \quad (1)$$

where N is the initial concentration of PMMA molecules, ν is a constant, E is the activation energy of the reaction, and T is the temperature. It follows from Eq. (1) that the formation rate of absorbing decomposition products drastically increases with temperature; i.e., the increase in absorption rate in the plasma channel, which is proportional to the concentration of decomposition products, should also increase. This is inconsistent with the dependence presented in Fig. 7. This discrepancy can be explained by assuming that the activation energy decreases under extreme experimental conditions (at high temperatures and pressures) with increasing laser pulse energy. Such a decrease in the activation energy of the decomposition reaction (compared to the isothermal conditions described by Eq. (1)) was observed in shock-wave-compression experiments [15].

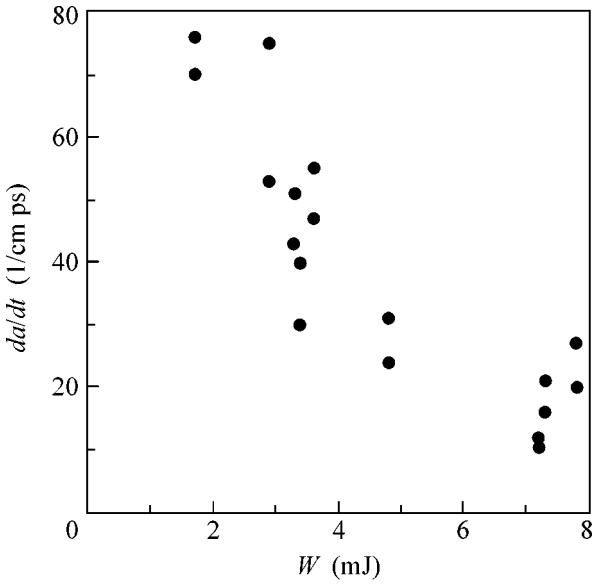

Fig. 7. Dependence of the absorption-increase rate in the channel on the material temperature.

Thus, we have studied the dynamics of a shock wave generated upon axicon focusing of intense femtosecond pulses onto PMMA. We used a method that allowed for the investigation of the dynamics during a single laser pulse with high spatial and time resolutions. We have shown that a few millijoule femtosecond laser pulse can generate shock waves with rather large amplitudes (>10 GPa). The absorption dynamics of the probe radiation show the complicated kinetics of target-material decomposition during shock-wave compression.

This work was supported by the Russian Foundation for Basic Research (project nos. 01-02-17512 and 02-02-17271).

REFERENCES

1. P. P. Pronko, S. K. Dutta, S. Squier, *et al.*, Opt. Commun. **114**, 106 (1995).
2. B. C. Stuart, M. D. Feit, S. Harman, *et al.*, Phys. Rev. B **53**, 1749 (1996).
3. F. Glezer, Ch. Shaffer, N. Nishimura, *et al.*, Opt. Lett. **22**, 1817 (1997).
4. A. A. Babin, A. M. Kiselev, A. M. Sergeev, and A. N. Stepanov, Kvantovaya Élektron. (Moscow) **31**, 623 (2001) [Quantum Electron. **31**, 623 (2001)].
5. D. Stricland and G. Mourou, Opt. Commun. **56**, 212 (1985).
6. V. V. Korobkin *et al.*, Kvantovaya Élektron. (Moscow) **13**, 265 (1986) [Sov. J. Quantum Electron. **16**, 178 (1986)].

7. A. A. Babin, A. M. Kiselev, K. I. Pravdenko, *et al.*, Usp. Fiz. Nauk **169**, 29 (1999) [Phys. Usp. **42**, 74 (1999)].
8. S. V. Garnov, V. I. Kononov, A. A. Malyutin, *et al.*, Laser Phys. **13**, 386 (2003).
9. *Handbook on Physical Constants*, Ed. by I. S. Grigor'ev and E. Z. Meĭlikhov (Énergoatomizdat, Moscow, 1991; CRC, Boca Raton, 1997).
10. Ya. B. Zel'dovich and Yu. P. Raĭzer, *Physics of Shock Waves and High-Temperature Hydrodynamic Phenomena*, 2nd ed. (Nauka, Moscow, 1966; Academic, New York, 1967).
11. A. A. Bakaeva, I. P. Dunaev, and R. F. Trunin, Fiz. Tverd. Tela (Leningrad) **7**, 1615 (1965) [Sov. Phys. Solid State **7**, 1307 (1965)].
12. D. I. Kulagin, *Technical Digest IQEC/LAT-YS 2002* (2002), p. 47.
13. P. Andebert, Ph. Daguzan, A. Dos Santos, *et al.*, Phys. Rev. Lett. **73**, 1990 (1994).
14. S. V. Shulepov, *Physics of Carbon–Graphite Materials* (Metallurgiya, Moscow, 1968) [in Russian].
15. G. I. Kanel', S. V. Razorenov, A. V. Utkin, and V. E. Fortov, *Impact-Wave Phenomena in Condensed Media* (Yanus-K, Moscow, 1996) [in Russian].

Translated by M. Sapozhnikov

JETP Letters, Vol. 80, No. 5, 2004, pp. 303–307. From Pis'ma v Zhurnal Éksperimental'noĭ i Teoreticheskoĭ Fiziki, Vol. 80, No. 5, 2004, pp. 349–353.

Quasi-One-Dimensional Anisotropic Heisenberg Model in a Transverse Magnetic Field¶

D. V. Dmitriev* and V. Ya. Krivnov

Joint Institute of Chemical Physics, Russian Academy of Sciences, Moscow, 117977 Russia

**e-mail: dmitriev@deom.chph.ras.ru*

Received July 7, 2004

The phase diagram of weakly coupled *XXZ* chains in a transverse magnetic field is studied using the mean-field approximation for the interchain coupling and known exact results for an effective one-dimensional model. The results are applied to the quasi-one-dimensional antiferromagnet Cs_2CoCl_4, and the value of interchain interaction in this compound is estimated. © *2004 MAIK "Nauka/Interperiodica".*

PACS numbers: 75.10.Jm

The effects induced by magnetic fields in low-dimensional magnets are the subject of intensive theoretical and experimental research [1]. One of the striking effects is the dependence of magnetic properties of quasi-one-dimensional (Q1D) antiferromagnets with anisotropic interactions on the direction of the applied magnetic field. For example, the behavior of these systems in a transverse magnetic field is drastically different in comparison with the case of a longitudinal field applied along the anisotropy axis. In particular, the transverse field induces a gap in the spectrum and the antiferromagnetic long-range order (AF LRO) in the perpendicular direction. A quantum phase transition takes place at some critical field, where the LRO and the gap vanish. The phase transition of this type has been observed in the Q1D antiferromagnet Cs_2CoCl_4 [2]. The simplest model of the one-dimensional anisotropic antiferromagnet in the transverse field is the spin-1/2 *XXZ* chain described by the Hamiltonian

$$\mathcal{H}_{1D} = J\sum (S_n^x S_{n+1}^x + S_n^y S_{n+1}^y + \Delta S_n^z S_{n+1}^z) - H\sum S_n^x, \quad (1)$$

where Δ is an anisotropy parameter, assumed to be $0 \le \Delta \le 1$.

It has been proposed [2] that low-energy properties of Cs_2CoCl_4 is described by (1) with $J = 0.23$ meV and $\Delta = 0.25$. In contrast to the case of the longitudinal field, the symmetry-breaking transverse field does not commute with the *XXZ* Hamiltonian and the exact integrability of (1) is destroyed. The model (1) has been investigated using different approximate approaches [3–6]. The scaling estimates at a small field [7] show that the transverse field generates the staggered magnetization $M_{st} = \langle (-1)^n S_n^y \rangle$ (AF LRO in the *Y* direction) and the gap in the spectrum m (at $H = 0$, the spectrum is gapless):

$$m \sim (H/J)^{\frac{1}{2-d}}, \quad d = \frac{\eta}{2} + \frac{1}{2\eta},$$
$$M_{st} \sim (H/J)^{\frac{\eta/2}{2-d}}, \quad \eta = 1 - \frac{1}{\pi}\arccos\Delta. \quad (2)$$

To study model (1), when the field H is not small, a mean-field approximation (MFA) has been proposed in [7] and elaborated in [8]. The MFA is based on the Jordan–Wigner transformation of spin-1/2 operators to the Fermi ones with the subsequent mean-field treatment of the four-fermion interaction term. As a result, the arising Hamiltonian is quadratic in Fermi-operators, and it is solved exactly. Transforming this MFA Hamiltonian back to spin variables, we obtain a spin-1/2 *XY* model in the longitudinal field:

$$\mathcal{H}_{XY} = J'\sum [(1-\gamma)S_n^x S_{n+1}^x + (1+\gamma)S_n^y S_{n+1}^y - hS_n^z], \quad (3)$$

where parameters J', γ, and h are determined by the MFA self-consistent conditions [7, 8].

Model (3) is exactly solvable, and its properties are well studied [9]. This model undergoes a $T = 0$ phase transition of the 2D Ising universality class at $h = 1$ corresponding to the MFA value of the critical field $H_c^{1D}(\Delta)$. In particular, in the vicinity of the critical field $M_{st} \sim |H_c^{1D}(\Delta) - H|^{1/8}$. A comparison of the MFA results with those obtained in precise numerical DMRG calculations shows high accuracy of the MFA at $H \gtrsim J$ [8]. The dependence $M_{st}(H)$ for $\Delta = 0.25$ obtained with use of the MFA and scaling estimate (2) is shown in Fig. 1 by a dashed line. This magnetization curve is qualitatively similar to that observed in neutron-scattering

¶ This article was submitted by the authors in English.

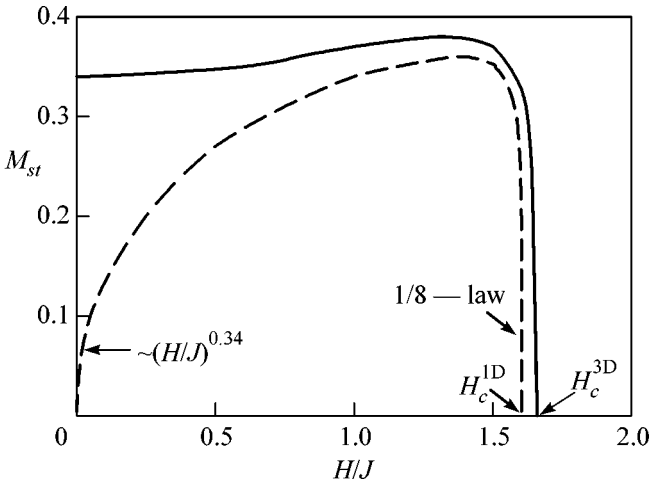

Fig. 1. The dependence of the $T = 0$ LRO parameter on magnetic field for a 1D chain (dashed line) and Q1D system (solid line) for $\Delta = 0.25$.

experiments on Cs_2CoCl_4. At the same time, there is essential difference in the low-field behavior of M_{st}. The experimental AF ordered moment is finite at $H = 0$, while $M_{st} \longrightarrow 0$ according to (2). This difference is due to weak interchain couplings in real systems, and these couplings form a 3D magnetically ordered moment below the Néel temperature T_N. Besides, interchain couplings extend the 1D ordered phase with $M_{st} \neq 0$ to finite temperatures. Therefore, to describe low-temperature properties of real Q1D compounds, it is necessary to take into account interchain interactions.

In this letter, we will consider the system of coupled parallel *XXZ* chains in a transverse field described by the Hamiltonian

$$\mathcal{H} = J\sum(S^x_{n,\mathbf{r}}S^x_{n+1,\mathbf{r}} + S^y_{n,r}S^y_{n+1,\mathbf{r}} + \Delta S^z_{n,\mathbf{r}}S^z_{n+1,\mathbf{r}}) + J_\perp\sum(S^x_{n,\mathbf{r}}S^x_{n,\mathbf{r}+\delta} + S^y_{n,\mathbf{r}}S^y_{n,\mathbf{r}+\delta} + \Delta S^z_{n,\mathbf{r}}S^z_{n,\mathbf{r}+\delta}) - H\sum S^x_{n,\mathbf{r}}, \quad (4)$$

where n and $\mathbf{r}$ label lattice sites along the chain and in perpendicular directions, δ is summed over two nearest-neighbor vectors in the transverse directions, and $J_\perp$ is a weak coupling between neighboring chains.

A standard method for treating model (4) is to use the mean-field approximation for interchain coupling and to treat the resulting effective 1D problem as exactly as possible [10, 11] (we call this approach as chain mean-field theory (CMFT) to distinguish it from the MFA for the 1D model (1)). We assume that AF order in each chain to be oriented along the *Y* direction and the uniform magnetization along the *X* axis as it occurs in the pure 1D model (1). The quasi-1D model contains another mechanism to generate the LRO. If one of the chains is AF ordered, the interchain couplings induce an effective staggered field on the nearest chains. In the CMFT, interchain coupling is replaced by effective fields and the Hamiltonian (4) reduces to an effective 1D Hamiltonian having the form

$$\mathcal{H}_{\text{eff}} = J\sum(S^x_nS^x_{n+1} + S^y_nS^y_{n+1} + \Delta S^z_nS^z_{n+1}) - (H - H_x)\sum S^x_n - H_y\sum(-1)^n S^y_n, \quad (5)$$

where fields H_x and H_y are determined by self-consistency relations

$$H_x = zJ_\perp\langle S^x_n\rangle, \quad H_y = zJ_\perp M_{\text{st}}, \quad (6)$$

z is the transverse coordination number.

At first, we consider the model (5) at $H = 0$ and $T = 0$. It can be easily shown that the self-consistency relation gives $\langle S^x_n\rangle = 0$ and the model (5) reduces to the *XXZ* chain in the staggered field. The low-energy properties of this model are described by a quantum sine-Gordon model [12]

$$\mathcal{H} = \mathcal{H}_0 + V,$$

$$\mathcal{H}_0 = \frac{v(\eta)}{2}\int dx\{(\partial_x\Phi)^2 + (\partial_x\Theta)^2\}, \quad (7)$$

$$V = -H_y\sqrt{2A(\eta)}\int dx\sin(\sqrt{2\pi\eta}\Theta),$$

where $\Phi(x)$ and $\Theta(x)$ are boson and dual fields, respectively, $v(\eta) = J\sin(\pi\eta)/(2 - 2\eta)$ is the sound velocity, and the coefficient $A(\eta)$ was found in [13].

The spectrum of $\mathcal{H}_0$ is gapless. The perturbation V has the scaling dimension $\eta/2$ and generates the mass gap

$$m = v\left(\frac{CH_y}{v}\right)^{\frac{1}{2-\eta/2}}, \quad (8)$$

where the constant C is [14]

$$C = \frac{\sqrt{2A}\pi\Gamma\left(1-\frac{\eta}{4}\right)}{2\Gamma\left(\frac{\eta}{4}\right)}\left(\frac{2}{\sqrt{\pi}}\frac{\Gamma\left(\frac{\eta}{8-2\eta}\right)}{\Gamma\left(\frac{2}{4-\eta}\right)}\right)^{2-\eta/2}. \quad (9)$$

The staggered magnetization M_{st} is related to mass gap m as [13]

$$M_{\text{st}} = \sqrt{2A}\langle\exp(i\sqrt{2\pi\eta}\Theta)\rangle = D\left(\frac{m}{v}\right)^{\eta/2}, \quad (10)$$

where

$$D = \frac{\sqrt{2A}\pi\Gamma\left(1-\frac{\eta}{4}\right)}{(16-4\eta)\sin\left(\frac{\pi\eta}{4-\eta}\right)\Gamma\left(\frac{\eta}{4}\right)} \times\left(\frac{\Gamma\left(\frac{2}{4-\eta}\right)\Gamma\left(\frac{8-3\eta}{8-2\eta}\right)}{4\sqrt{\pi}}\right)^{\frac{\eta}{2}-2}. \quad (11)$$

From Eqs. (8) and (10), we get

$$M_{st} = D\left(CD\frac{zJ_\perp}{v}\right)^{\frac{\eta/2}{2-\eta}}, \quad (12)$$

$$m = v\left(CD\frac{zJ_\perp}{v}\right)^{\frac{1}{2-\eta}}. \quad (13)$$

The AF LRO M_{st} survives at $T < T_N$. The Néel temperature T_N can be found using the random phase approximation (RPA). The RPA dynamical susceptibility of coupled chains in the disordered phase ($T > T_N$) is

$$\chi^{yy}(\omega, k, k_\perp) = \frac{\chi^{yy}_{1D}(\omega, k)}{1 - J_\perp(k_\perp)\chi^{yy}_{1D}(\omega, k)}. \quad (14)$$

The condition determined T_N is

$$zJ_\perp\chi^{yy}_{1D}(0, \pi) = 1. \quad (15)$$

The dynamical susceptibility of the 1D *XXZ* model at $T \ll J$ is known [15]

$$\chi^{yy}_{1D}(0, \pi) = \frac{B}{v}\left(\frac{v}{2\pi T}\right)^{2-\eta}, \quad (16)$$

where

$$B = A\sin(\pi\eta/2)\frac{\Gamma^2(1-\eta/2)\Gamma^2(\eta/4)}{\Gamma^2(1-\eta/4)}. \quad (17)$$

Using the condition (15), we extract the Néel temperature at $H = 0$:

$$T_N(H = 0) = \frac{v}{2\pi}\left(\frac{BzJ_\perp}{v}\right)^{\frac{1}{2-\eta}}. \quad (18)$$

We note that the ratio T_N/m does not depend on $J_\perp$ and is determined by 1D parameter η only.

An analysis of experimental data carried out in [2] has shown that the Q1D antiferromagnet Cs_2CoCl_4 consists of two interpenetrating sublattices with identical intrasublattice interactions. These sublattices are noninteracting on the CMFT level. Each sublattice has tetragonal symmetry and described by model (4) with $z = 4$. However, no direct experimental data on the value of the interchain interaction $J_\perp$ is available. The Néel temperature in Cs_2CoCl_4 at $H = 0$ is $T_N = 0.0813J = 0.217$ K [2]. Using these data, we can estimate the unknown value of $J_\perp$ in Cs_2CoCl_4. Substituting $\Delta = 0.25$ ($A = 0.1405$) in (18), we find

$$\frac{J_\perp}{J} = 0.0147. \quad (19)$$

This value is very small, so that our assumption about the Q1D behavior of the system is justified.

Further, using the found value of $J_\perp$, we can find the staggered magnetization M_{st} at $T = 0$. According to Eq. (12), $M_{st} = 0.348$. The experimental value of the AF ordered moment at $T \ll T_N$ is $M_{st} \approx 0.342$ [2]. Such a perfect coincidence confirms our estimate (19). Besides, the found value of $J_\perp$ gives us also the gap (13) $m = 0.78$ K. It is remarkable that even so small interchain coupling as in Eq. (19) causes so large value of LRO and the gap.

At $H = 0$ and $T = 0$, the AF LRO is generated by the interchain couplings. At $H > 0$, the "one-dimensional" mechanism is switched. The crude estimation of the value H^*, at which this mechanism becomes predominant, can be obtained by a comparison of (2) with (13),

$$H^* \sim J(zJ_\perp/J)^{\frac{2-d}{2-\eta}}. \quad (20)$$

At $H > H^*$ in Hamiltonian (5), the mean field H_x can be neglected in comparison with H, and, at $T = 0$, the main effect of H_y consists in a small shift of the critical field H_c^{1D} (see below).

At $H = H_c^{1D}$ and $H_y = 0$, the spectrum of model (5) is gapless. The perturbation $H_y\sum(-1)^n S_n^y$ has scaling dimension 1/8 and generates the mass gap $m \sim (H_y/J)^{8/15}$ and AF LRO $M_{st} \sim (H_y/J)^{1/15}$ in model (5). Self-consistency relations (6) therefore give

$$M_{st}(H_c^{1D}) \sim (zJ_\perp/J)^{1/14}, \quad m(H_c^{1D}) \sim (zJ_\perp/J)^{4/7}. \quad (21)$$

To estimate the Néel temperature $T_N(H)$ in the RPA, it is necessary to know the finite temperature staggered susceptibility $\chi^{yy}_{1D}(0, \pi)$ for the model (1) at $H > 0$. Unfortunately, it is unknown. Instead, we consider MFA model (3), for which the susceptibility can be found. As it was noted above, the MFA describes correctly the ground-state properties of the model (1) at $H \geq J$. We expect that the MFA gives a satisfactory description of (1) at low temperature ($T \ll J$) as well. The problem of finding $T_N(H)$ can be solved in the same manner as it was done by Carr and Tsvelik in [16] for

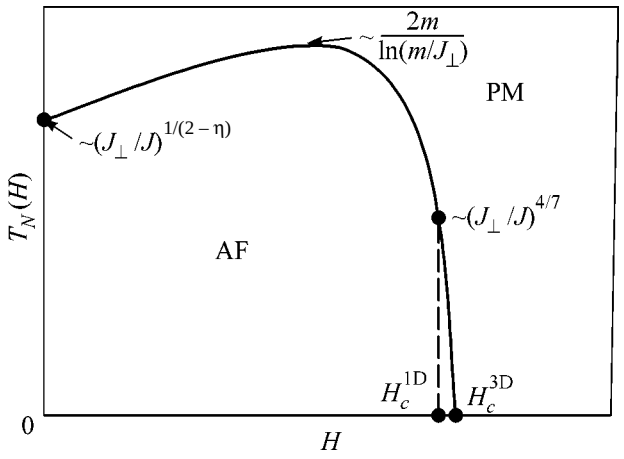

Fig. 2. Schematic phase diagram of model (4). The phase boundary separates the antiferromagnetic phase with $M_{st} \neq 0$ from the paramagnetic phase without AF LRO.

Q1D quantum Ising model, which, on the CMFT level, reduces to (3) with $\gamma = 1$.

We are mainly interested in the region of the fields near the critical field $H_c^{1D}(\Delta)$ or at $h \sim 1$ in terms of MFA Hamiltonian (3). Exactly at $h = 1$, where the model (3) is critical, the staggered susceptibility at $T \ll J$, according to [15] is,

$$\chi_{1D}^{yy}(0,\pi) = R(\gamma)\frac{\pi}{v_c}\left(\frac{v_c}{2\pi T}\right)^{7/4}\frac{\Gamma(7/8)\Gamma^2(1/16)}{\Gamma(1/8)\Gamma^2(15/16)}, \quad (22)$$

where sound velocity at the critical field $v_c = \gamma J'$ is determined from the MFA self-consistent equations [7] and

$$R(\gamma) = \frac{e^{1/4}2^{1/12}A^{-3}}{4}\frac{2\gamma^{3/4}}{1+\gamma} \quad (23)$$

with Glaisher constant $A \simeq 1.282$.

The Néel temperature in the RPA is

$$T_N(H_c^{1D}) = \frac{v_c}{2\pi}\left[\frac{\pi z J_\perp}{v_c}\frac{R(\gamma)\Gamma(7/8)\Gamma^2(1/16)}{\Gamma(1/8)\Gamma^2(15/16)}\right]^{4/7}. \quad (24)$$

For $\Delta = 0.25$, the critical field in the MFA is $H_c^{1D} \approx 1.6$ J and $v_c \approx 0.185$ J. Therefore, the estimated Néel temperature for Cs_2CoCl_4 is $T_N(H_c^{1D}) = 0.145$ K.

Near the critical field at $H \gtrsim H_c^{1D}$ (disorder region in the 1D model), the low-temperature staggered susceptibility is well approximated by the formula [1]

$$\chi_{1D}^{yy}(\omega,\pi-k) \approx \frac{\gamma^{3/4}}{1+\gamma}\frac{v(2m/v)^{1/4}}{v_c^2k^2 + m^2 - (\omega + i/\tau_c)^2}, \quad (25)$$

where the gap $m = |H - H_c^{1D}|$ and the phase relaxation time $\tau_c = (\pi/2T)e^{m/T}$ In this case, the RPA condition of phase transition (15) reads

$$m^2 + \tau_c^{-2} = \frac{(\gamma v_c)^{3/4}}{1+\gamma}(2m)^{1/4}zJ_\perp. \quad (26)$$

At first, we estimate the shift of the critical field $\delta H_c = H_c^{3D} - H_c^{1D}$ caused by interchain couplings. This shift is determined by the condition $T \longrightarrow 0$ in Eq. (26):

$$\delta H_c = 2^{1/7}\frac{(\gamma v_c)^{3/7}}{(1+\gamma)^{4/7}}(zJ_\perp)^{4/7}. \quad (27)$$

For $\Delta = 0.25$ and found value of $J_\perp$ (19), the shift of the critical field is about 3%. We note that, in the vicinity of the critical point H_c^{3D}, the low-energy properties of Q1D model (4) belong to the universality class of the (3 + 1)-dimensional classical Ising model.

Equation (26) gives also the behavior of Néel temperature near the 3D critical point $H_c^{3D} - H \ll \delta H_c$:

$$T_N(H) \approx 2(\delta H_c)\ln^{-1}\left(\frac{\delta H_c}{H_c^{3D} - H}\right). \quad (28)$$

At intermediate fields $H^* < H < H_c^{1D}$ (the 1D ordered region), the low temperature $T \ll m$ staggered susceptibility has an exponential form [1]

$$\chi_{1D}^{yy}(0,\pi) \sim (m/v)^{1/4}\xi_c\tau_c \sim \frac{v^{3/4}}{m^{1/4}T^{3/2}}e^{2m/T} \quad (29)$$

with correlation length $\xi_c = v\sqrt{\pi/2mT}\,e^{m/T}$ [1]. Thus, for $zJ_\perp \ll m(m/v)^{3/4}$, the RPA criteria (15) yields

$$T_N(H) \sim 2m(H)\ln^{-1}\left(\frac{m(H)}{zJ_\perp}\right). \quad (30)$$

Combining the found expressions for Néel temperature in different regions (18), (24), (28), and (30), we arrive at the phase diagram schematically shown in Fig. 2. Since the gap $m(H)$ in the AF ordered region has a maximum at some intermediate value of field [7, 8], then, according to Eq. (30), the function $T_N(H)$ also has a maximum as shown in Fig. 2. This fact was experimentally observed in Cs_2CoCl_4 [2].

This work was supported by the Russian Foundation for Basic Research, grant no. 03-03-32141.

REFERENCES

1. S. Sachdev, *Quantum Phase Transitions* (Cambridge Univ. Press, Cambridge, 1999).
2. M. Kenzelmann, R. Coldea, D. A. Tennant, *et al.*, Phys. Rev. B **65**, 144432 (2002).

3. J. Kurmann, H. Tomas, and G. Muller, Physica A (Amsterdam) **112**, 235 (1982); G. Muller and R. E. Shrock, Phys. Rev. B **32**, 5845 (1985).
4. S. Mori, J.-J. Kim, and I. Harada, J. Phys. Soc. Jpn. **64**, 3409 (1995).
5. Y. Hieida, K. Okunishi, and Y. Akutsu, Phys. Rev. B **64**, 224 422 (2001).
6. A. Langari, Phys. Rev. B **69**, 100 402 (2004).
7. D. V. Dmitriev, V. Ya. Krivnov, A. A. Ovchinnikov, and A. Langari, JETP **95**, 538 (2002); D. V. Dmitriev, V. Ya. Krivnov, and A. A. Ovchinnikov, Phys. Rev. B **65**, 172 409 (2002).
8. J.-S. Caux, F. H. L. Essler, and U. Low, Phys. Rev. B **68**, 134 431 (2003).
9. E. Barouch and B. M. McCoy, Phys. Rev. A **3**, 786 (1971).
10. D. J. Scalapino, Y. Imry, and P. Pincus, Phys. Rev. B **11**, 2042 (1975).
11. H. J. Schulz, Phys. Rev. Lett. **77**, 2790 (1996).
12. I. Affleck and M. Oshikawa, Phys. Rev. B **60**, 1038 (1999).
13. S. Lukyanov and A. Zamolodchikov, Nucl. Phys. B **493**, 571 (1997).
14. Al. B. Zamolodchikov, Int. J. Mod. Phys. A **10**, 1125 (1995).
15. H. J. Schulz and C. Bourbonnais, Phys. Rev. B **27**, 5856 (1983).
16. S. T. Carr and A. M. Tsvelik, Phys. Rev. Lett. **90**, 177 206 (2003).

JETP Letters, Vol. 80, No. 5, 2004, pp. 308–311. Translated from Pis'ma v Zhurnal Éksperimental'noĭ i Teoreticheskoĭ Fiziki, Vol. 80, No. 5, 2004, pp. 354–357.

Interrelation between Magnetic and Structural Phases in $La_{1-x}Sr_xMnO_3$ (x = 0.175) Manganite Single Crystal

Kh. G. Bogdanova[1, *], A. R. Bulatov[1], V. A. Golenishchev-Kutuzov[2], A. V. Kapralov[2], V. E. Leont'ev[1], and A. A. Potapov[2]

[1] *Kazan Physicotechnical Institute, Kazan Scientific Center, Russian Academy of Sciences, Kazan, 420029 Tatarstan, Russia*
**e-mail: acustica@dionis.kfti.knc.ru*

[2] *Kazan State Power Engineering University, Kazan, 420066 Tatarstan, Russia*

Received July 12, 2004

Investigation of the temperature and magnetic-field dependences of the electrical conductivity and the velocity and damping of the transverse ultrasonic waves at a frequency of 770 MHz revealed the temperature and magnetic hysteresises of the elastic parameters and the electrical resistivity. This is explained by the influence of magnetization on the structural phase transition in a manganite sample. The two-phase crystal structure influences the magnetization process and the behavior of resistivity in the vicinity of the concentrational intersection of the magnetic and structural phase transitions. *© 2004 MAIK "Nauka/Interperiodica".*

PACS numbers: 62.65.+k; 75.50.Pp

Strong interactions between the electron, magnetic, and lattice subsystems in lanthanum manganites $La_{1-x}R_xMnO_3$ (R = Ca, Ba, Sr) account for a variety of physical phenomena observed in these systems, including structural transformations, magnetic phase transitions, and insulator–metal transitions, depending on the concentration of R ions and on temperature [1]. It was established that the colossal magnetorestance (CMR) observed in these manganites occurs upon the transition from the state of a paramagnetic insulator to a ferromagnetic metal in the applied magnetic field [2]. However, the nature of CMR in these compounds still remains unclear, since the proposed model of a two-phase magnetic state [3] does not explain the whole diversity of the experimental facts. Moreover, it becomes more evident that the nature of this phenomenon is not always described by a single mechanism and can depend in some manganite compositions not only on the magnetic phases, but on the dielectric phases as well.

The question concerning the influence of magnetization on the character of structural phase transitions and CMR has been discussed almost since the very discovery of CMR [1, 2]. At the same time, the effect of structural phases on the behavior of magnetization and CMR was studied to a lesser extent, although certain activity in this direction has been observed in recent years [4, 5].

These circumstances stimulated us to study the interrelation between the magnetic and structural order and the role of these interactions in the CMR phenomenon by means of high-frequency ultrasonic waves and magnetoresistance measurements. High-frequency ultrasound at frequency f = 770 MHz ($\lambda \cong 5$ μm) allows the phase and spatial inhomogeneities caused by the structural or magnetic fluctuations to be determined with a greater precision. In addition, the velocity and damping of ultrasonic waves are highly sensitive to the magnetic and structural phase transitions.

The investigation was performed on a single crystal of $La_{1-x}Sr_xMnO_3$ (x = 0.175) manganite, since it was assumed [1, 6] that the intersection of the structural and magnetic phase-transition temperatures in this system takes place for $0.17 \le x \le 0.18$ in a rather extended temperature interval (T = 180–280 K). However, the temperature of the structural transition in the manganite with x = 0.175 had to be refined. In addition, the sample with x = 0.175 needed evidence of microscopic structural inhomogeneities [7]. Therefore, it was expected that the mutual influence of the magnetic and structural orderings in this sample would be the strongest. Moreover, the compound with x = 0.175 exhibits the most pronounced CMR among all the lanthanum strontium manganites studied.

The single-crystal sample (grown in the group headed by A.M. Balbashov at the Moscow Power Institute) had the shape of a parallelepiped with the dimensions $5 \times 5 \times 8$ mm. The sample edges were parallel to within a few seconds of arc and the faces were oriented perpendicular to the axes [100], [010], and [001]. The ultrasonic pulses with a duration τ_u = 0.5–0.8 μs were excited and detected by a rod-shaped piezotransducers made of x-cut lithium niobate crystals. The velocity and damping of the transverse ultrasonic waves were studied as functions of the temperature (in the range T = 150–350 K) and the applied magnetic field (H = 0–10 kOe). The measurements were performed in the piezotransducer–sample–piezotrans-

ducer scheme, whereby the ultrasonic pulses propagated along the [100] axis (in the cubic representation). The resistivity of the sample as a function of the external factors (temperature and magnetic field) was measured using the conventional four-probe technique.

Obviously, in the case of such a high acoustic frequency, it is possible that acoustic anomalies may be caused by the spatial inhomogeneities in the sample composition. However, the X-ray microprobe analysis of the chemical composition, performed at the Institute of Metal Physics, Yekaterinburg for the La, Sr, and Mn atoms, revealed no inhomogeneities in the spatial distribution of these components in the sample to within 1 μm. The high chemical homogeneity of the sample is also confirmed by the small width of the magnetization and magnetic susceptibility curves [8], because any spatial inhomogeneity would lead to their temperature broadening. Thus, since the ultrasound wavelength was ~5 μm, the inhomogeneities in the chemical composition cannot be the reason of any acoustic anomalies in the sample studied.

The investigation of the propagation of transverse ultrasonic waves in the $La_{1-x}Sr_xMnO_3$ crystal with x = 0.175 revealed sharp variations in the velocity and damping of these waves in three temperature intervals: T = 297–307, 280–285, and 200–230 K (Figs. 1, 2). The acoustic anomalies in the region of 283 K showed no hysteresis and could be attributed to the phase transition from the paramagnetic (PM) to the ferromagnetic (FM) state, which was confirmed by the results of magnetic measurements performed for the same sample [8]. The changes in the velocity and damping exhibited hysteresises centered at 305 and 220 K and, hence, they could be assigned to the first-order phase transitions. We believe that a significant increase in the degree of damping with decreasing temperature in the interval T = 200–300 K is caused by the scattering of ultrasonic waves on the microscopic structural inhomogeneities observed earlier in [7]. Indeed, below 200 K, i.e., with the formation of the homogeneous structure, the damping decreases.

In the temperature range from 310 to 150 K, the velocity and damping of the ultrasonic waves varied in the applied magnetic field. The most pronounced variations of the elastic modulus (c_{44}) in the magnetic field were observed in the interval T = 200–300 K, where these changes also exhibited hysteresis. The magnetic-field-induced changes were observed even in the fields appreciably lower than 10 kOe. The application of a magnetic field also shifted the positions of maxima in the temperature dependences of the ultrasound velocity and damping near 300 K to lower temperatures.

Beginning at T = 305 K, we observed a decrease in the resistivity in magnetic fields H < 10 kOe (Fig. 3), with a hysteresis in the temperature interval T = 200–220 K. The CMR signal at H = 10 kOe exhibited two peaks, at T = 310 and 220 K.

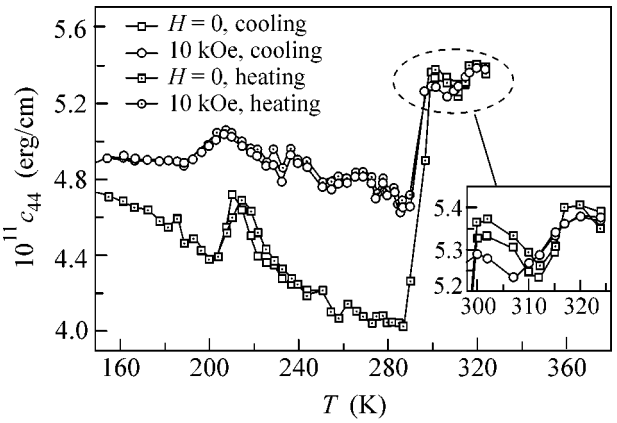

Fig. 1. The temperature dependence of the elastic modulus c_{44} in $La_{0.825}Sr_{0.175}MnO_3$ manganite. The inset shows the region of 295–325 K on a larger scale.

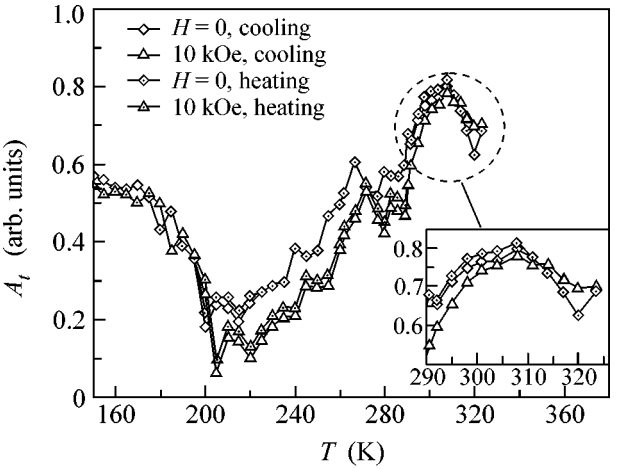

Fig. 2. The temperature dependence of the amplitude A_t of the transverse mode of ultrasonic oscillations in $La_{0.825}Sr_{0.175}MnO_3$ manganite. The inset shows the region of 295–325 K on a larger scale.

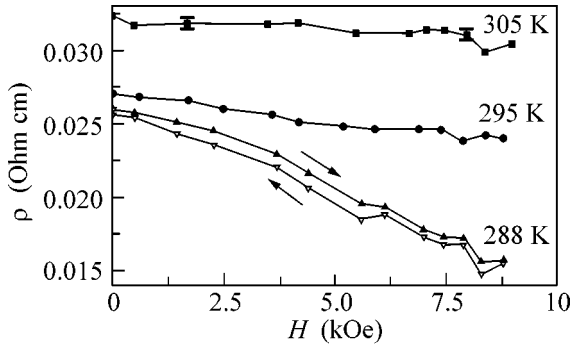

Fig. 3. Plots of the resistivity ρ versus magnetic field for $La_{0.825}Sr_{0.175}MnO_3$ manganite at T = 288, 295, and 305 K.

Thus, we can state that the sharp variations in the parameters of acoustic waves and resistivity observed in the regions of 305 and 220 K can be assigned to the first-order phase transitions, specifically, to the transitions from the rhombohedral to the orthorhombic structure in the PM and FM phases, respectively. The first of these transitions is strongly influenced by the appearance of a magnetic order. As follows from the data on the increase in T_c with increasing content of strontium ions [1], from the temperature dependence of the magnetization of the sample with $x = 0.175$ [9], and from the NMR data [9], the local regions where the magnetization exceeds the average magnetization of the sample appear even at $T \sim 310$ K. The growth of spontaneous magnetization leads to the reverse transition from the orthorhombic to the rhombohedral phase, as was assumed for a sample with $x = 0.170$ in a magnetic field [1]. The need for a magnetic field in the case of a sample with $x = 0.170$ is explained by the absence of spontaneous magnetization in this sample near the structural phase-transition temperature (T_s). In our case, the magnetization is initially present and the external field only increases the total magnetization of the sample.

The difference ΔE in elastic energies of the two structures is not very large, because $\Delta E = \frac{1}{2} cK(\Delta V/V)^2$, where V is the unit-cell volume, c is the elastic modulus, ΔV is a change in the unit-cell volume upon the structural phase transition, and $\kappa = \frac{1}{3}(c_{11} + 2c_{12})$. Therefore, using the known data for ΔV in a manganite crystal with the given composition [10], one obtains the value $\Delta E/k_B \sim 5.5$ K (k_B is the Boltzmann constant). As can be seen from Fig. 1, the change in the elastic modulus C_{44} in the vicinity of the structural phase transition does not exceed 10–15%, which approximately corresponds to the accuracy of the determination of the energy difference ΔE (the estimate of ΔE was obtained using the average value of c_{44}).

At the same time, a change in the magnetic energy per unit cell for the magnetization M and spin 3/2 in the case of Mn^{3+} ions amounts to $\Delta E_M/M\kappa_B \approx 6\kappa_B/T$ [11]. Since the transformation of the rhombohedral (R) to the orthorhombic (O) structure in the PM phase is incomplete, the field of spontaneous magnetization M is sufficient to provide a 3–5 K shift in the transition temperature. The orthorhombic structure is eventually established upon the second transition (i.e., in the FM phase) in the temperature interval $T = 200$–230 K. In a magnetic field $H \leq 10$ kOe, the degree of FM spin ordering increases, which enhances the increase in the ultrasonic wave velocity and the decrease in the damping of the transverse acoustic waves caused by the $R \longrightarrow O$ structural transition.

Near the intersection of the structural and magnetic phase transitions, microscopic inhomogeneities appear in the PM phase. These were characterized by us as magnetoelastic domains [7]. The presence of such domains can be considered as a two-phase magnetic and a two-phase structural states in the sample, which were determined by the temperature and the applied magnetic field. It is pertinent to drew an analogy with the behavior of ferroelectric relaxors, which also belong to the class of perovskites in which the coexistence of paraelectric and ferroelectric phases induces the formation of ferroelectric clusters in the paraelectric phase [12, 13]. Thus, the state of a manganite crystal with $x = 0.175$ in the temperature interval $T = 200$–310 K can be considered to be characteristic of the inhomogeneous restructured systems.

The formation of microscopic structural inhomogeneities influences, to a certain extent, the character of magnetization and especially the temperature dependence of the electrical conductivity and CMR. The appearance of elastic stresses at the domain boundaries will hinder, as was theoretically predicted in [14], the process of monodomenization with the formation of a homogeneous magnetic state in the sample. This is evidenced by the appearance of a magnetic hysteresis in the resistivity at temperatures corresponding to the two-phase structural state (Fig. 3).

The formation of a two-phase (R–O) structural state characteristic of the lanthanum–strontium manganite with $x = 0.175$ leads to an increase in the resistivity at $T = 300$–310 K as a result of the decrease in the charge-carrier transfer between the FM domains. This increase in the resistivity is one of the factors responsible for the growth in the amplitude of resistance variations in the magnetic field (Fig. 3). This is confirmed by a decrease in the resistance over a wide range of temperatures [8], by the two peaks observed in the temperature dependence of CMR, and by a small jump in T_c for the compositions in the vicinity of $x = 0.175$ [2].

Thus, we believe that two structural states, rhombohedral and orthorhombic, coexist in a single crystal of lanthanum strontium manganite $La_{1-x}Sr_xMnO_3$ with $x = 0.175$ over the entire temperature range from 220 to 300 K. The rhombohedral state is maintained due to the magnetic ordering of the sample. In turn, the presence of two structural phase states slows the growth of ferromagnetic ordering in the sample.

REFERENCES

1. A. Asamitsu, Y. Moritomo, R. Kumai, *et al.*, Phys. Rev. B **54**, 1716 (1996).
2. A. Urushibara, Y. Moritomo, T. Arima, *et al.*, Phys. Rev. B **51**, 14103 (1995).
3. E. Dagotto, Phys. Rep. **1**, 344 (2001).
4. J. Mira, J. Rivas, A. Moreno-Gobbi, *et al.*, Phys. Rev. B **68**, 092404 (2003).
5. F. Kordero, C. Castellano, R. Cantelli, *et al.*, Phys. Rev. B **68**, 012403 (2002).

6. Kh. G. Bogdanova, A. R. Bulatov, V. A. Golenishchev-Kutuzov, *et al.*, Akust. Zh. **48**, 596 (2002) [Acoust. Phys. **48**, 524 (2002)].
7. Kh. G. Bogdanova, A. R. Bulatov, V. A. Golenishchev-Kutuzov, *et al.*, Pis'ma Zh. Éksp. Teor. Fiz. **78**, 753 (2003) [JETP Lett. **78**, 305 (2003)].
8. Kh. G. Bogdanova, A. R. Bulatov, V. A. Golenishchev-Kutuzov, *et al.*, Fiz. Tverd. Tela (St. Petersburg) **45**, 284 (2003) [Phys. Solid State **45**, 298 (2003)].
9. N. A. Viglin, S. V. Naumov, and Ya. M. Mukovskiĭ, Fiz. Tverd. Tela (St. Petersburg) **43**, 1855 (2001) [Phys. Solid State **43**, 1934 (2001)].
10. R. Dabrowski, X. Xiong, Z. Bukowski, *et al.*, Phys. Rev. B **60**, 7006 (1999).
11. J. W. Tucker and V. W. Rampton, *Microwave Ultrasonics in Solid State Physics* (North-Holland, Amsterdam, 1972; Mir, Moscow, 1975).
12. D. Viehland, S. J. Jang, L. E. Cross, *et al.*, J. Appl. Phys. **68**, 2916 (1990).
13. Z. G. Lu and G. Calvarin, Phys. Rev. B **51**, 2694 (1995).
14. D. I. Khomskii and K. I. Kugel, Phys. Rev. B **67**, 134 401 (2003).

Translated by P. Pozdeev

JETP Letters, Vol. 80, No. 5, 2004, pp. 312–316. From Pis'ma v Zhurnal Éksperimental'noĭ i Teoreticheskoĭ Fiziki, Vol. 80, No. 5, 2004, pp. 358–362.

Exciton Effects in a Scaling Theory of Intermediate Valence and Kondo Systems¶

V. Yu. Irkhin[1, *] and M. I. Katsnelson[2]

[1] *Institute of Metal Physics, Yekaterinburg, 620219 Russia*

** e-mail: Valentin.Irkhin@imp.uran.ru*

[2] *University of Nijmegen, NL 6525 ED, Nijmegen, the Netherlands*

Received July 16, 2004

An interplay of the Kondo scattering and exciton effects (*d–f* Coulomb interaction) in intermediate valence systems and Kondo lattices is demonstrated to lead to an essential change of the scaling behavior in comparison with the standard Anderson model. In particular, a marginal regime can occur where characteristic fluctuation rate is proportional to flow cutoff parameter. In this regime, the "Kondo temperature" itself is strongly temperature-dependent, which may give a key to the interpretation of controversial experimental data for heavy fermions and related systems. © *2004 MAIK "Nauka/Interperiodica".*

PACS numbers: 71.27.+a; 71.28.+d; 75.30.Mb

There is an interesting class of rare-earth compounds such as $Ce_4Bi_3Pt_3$, SmB_6, and SmS under pressure (the "golden" phase), TmSe, and YbB_{12}, which were called earlier intermediate valence (IV) compounds and now are treated as "heavy-fermion (HF) semiconductors" or "Kondo insulators" (for a review, see [1, 2]). The various names emphasize different peculiarities of these compounds. As for electron energy spectrum, most of them are narrow gap semiconductors with an anomalously small energy scale (gap width) on the order of tens or hundreds of kelvins (see [2] and a review of earlier experiments in [3]). At the same time, they demonstrate an intermediate valence of rare earth ions (usually, between 2+ and 3+) in a number of properties, e.g., in the lattice constants (which are intermediate between those for isostructural compounds with di- and trivalent ions), core level spectra (which are a mixture of the spectra of di- and trivalent ions with comparable weights), and many others [1, 4, 5].

As well as for the HF metals, the origin of this small-energy scale is a key point for understanding the anomalous properties of the IV compounds. For the HF metals, it is commonly accepted now that they are Kondo lattices, which means that this energy scale (the Kondo temperature T_K) is a width of the Kondo resonance owing to spin-dependent scattering of conduction electrons by *f*-electron centers [6]. As a result of an interplay of the Kondo effect and interatomic magnetic interactions, the T_K value for a lattice can strongly differ from that for an isolated impurity [7], spin fluctuations being of crucial importance for the HF behavior. It is very natural to expect that these effects are important also for the IV compounds. At the same time, valence or *charge* fluctuations should be also considered. They are determined in part by the Coulomb ("Falicov–Kimball") interaction between conduction and localized electrons [8]. Taking into account these interactions together with the hybridization processes, it is possible to describe the IV state as a kind of exciton condensation [3, 9]. Note that, in the IV regime, the one-center spinless Falicov–Kimball model with hybridization is formally equivalent to the anisotropic Kondo problem, different valent states playing the role of pseudospin "up" and "down" states [10]. It is the degeneracy of quantum states for a scattering center, which is important for the formation of the Kondo resonance [11]. In the IV case, the divalent and trivalent states are degenerate by definition, so that this analogy is not surprising. Therefore, it is natural to consider the formation of the Kondo resonance for the IV compounds taking into account both spin and charge fluctuations, or, equivalently, both the "Kondo" and exciton ("Falicov–Kimball") effects. This is the aim of the present work. Since there is no clear demarcation between the IV and Kondo systems, it will be shown that the excitonic effects may be relevant also for the latter case.

To investigate the effects of interaction of current carriers with local moments, we use the Hamiltonian of the asymmetric infinite-*U SU*(*N*) Anderson model with inclusion of the Falicov–Kimball interaction (on-site *d–f* Coulomb repulsion *G*),

$$\mathcal{H} = \sum_{\mathbf{k}m} [t_{\mathbf{k}} c^{\dagger}_{\mathbf{k}m} c_{\mathbf{k}m} + V(c^{\dagger}_{\mathbf{k}m} f_{\mathbf{k}m} + f^{\dagger}_{\mathbf{k}m} c_{\mathbf{k}m}) + E_f f^{\dagger}_{\mathbf{k}m} f_{\mathbf{k}m}] + G \sum_{imm'} f^{\dagger}_{im} f_{im} c^{\dagger}_{im'} c_{im'}, \quad (1)$$

¶ This article was submitted by the authors in English.

where the on-site f–f Coulomb interaction is put to infinity, so that doubly occupied states are suppressed; $f^{\dagger}_{im} = |im\rangle\langle i0|$ are the Hubbard operator ($|im\rangle$ and $|i0\rangle$ are single-occupied and empty states); we neglect, for simplicity, the $\mathbf{k}$-dependence of the hybridization V. Note that similar calculations can be performed for realistic rare-earth ions, including the case of two magnetic configurations (see [12]).

Following [10], we treat coherent and incoherent cases. In the first case, a dispersion in the spectrum of f-electrons occurs. For simplicity, this is assumed to be proportional to the conduction electron spectrum, $E_{f\mathbf{k}} = E_f + \lambda\epsilon_{\mathbf{k}}$, $\epsilon_{\mathbf{k}} \propto t_{\mathbf{k}}$, $\lambda = -1$ (the f-band has a hole character). In the incoherent regime, $\lambda = 0$, so that f-electrons remain localized. Note that, in the presence of an energy gap, we always deal with the coherent regime.

The renormalization of Coulomb parameter G and hybridization V is obtained, similar to [10], from the two-particle Green's function

$$F^{\sigma}_{mm'}(E) = \langle\langle f^{\dagger}_{im} c_{im'} | c^{\dagger}_{im'} f_{im}\rangle\rangle_E, \qquad (2)$$

which determines the vertex. We obtain a singular correction with the structure

$$\delta F^{\sigma}_{mm'}(E) = GF^{\sigma}_{mm'}(E)\sum_{\mathbf{q}} \frac{n_{\mathbf{q}m'}}{E - t_{\mathbf{q}} + E_f}, \qquad (3)$$

where $n_{\mathbf{k}m} = \langle c^{\dagger}_{\mathbf{k}m} c_{\mathbf{k}m}\rangle$ is the Fermi function. In the coherent regime, a similar correction occurs from the dispersion of f-states. Correction (3) contains a logarithmic Kondo-like divergence, owing to charge fluctuations, which is cut at E_f (the latter quantity plays the role of the external field in the equivalent anisotropic Kondo model). Unlike the renormalization of E_f, the renormalizations of V and G do not contain the degeneracy factor of N.

The renormalization of E_f owing to spin-flip processes is obtained in the second order in hybridization (cf. [12–14])

$$\delta E_{fm} = V^2 \sum_{m' \neq m,\, \mathbf{q}} \frac{n_{\mathbf{q}m'}}{E_F - t_{\mathbf{q}}} + n\delta G. \qquad (4)$$

We have taken into account, in Eq. (4), the Hartree renormalization of f-level energy, which occurs in the coherent case, $E_f \longrightarrow E_f + Gn$, n being the concentration of conduction electrons; we put in numerical calculations $n = 1$, which corresponds to the Kondo regime.

To derive the scaling equations for the effective model parameters, we use the poor-man scaling approach [15]. Picking out in the integrals with the Fermi functions (3), (4), the contributions from the energy layer $C < E < C + \delta C$ near the Fermi level $E_F = 0$ ($C < 0$), and replacing $E_f \longrightarrow E_f(C)$, $V \longrightarrow V(C)$, $G \longrightarrow G(C)$, we obtain (cf. [10])

$$\frac{\partial E_f(C)}{\partial \ln|C|} = -\rho(N-1)V^2(C) + n\frac{\partial G(C)}{\partial \ln|C|}, \qquad (5)$$

$$\frac{\partial V(C)}{\partial \ln|C - E_f|} = -\frac{1-\lambda}{1+|\lambda|}\rho V(C)G(C), \qquad (6)$$

$$\frac{\partial G(C)}{\partial \ln|C - E_f|} = \frac{2\lambda}{1+|\lambda|}\rho G^2(C), \qquad (7)$$

where ρ is the bare conduction-electron density of states at E_F. Earlier [3], we have considered the exciton effects with neglecting spin fluctuations. We will see that the renormalization (4) results in new essential effects.

We have, from Eqs. (6) and (7)

$$\frac{G(C)}{G(0)} = \left[\frac{V(C)}{V(0)}\right]^{\alpha}, \quad \alpha = -\frac{2\lambda}{1+|\lambda|}, \qquad (8)$$

so that $G(C) = G(0)$ in the incoherent regime. From (6), we derive, in the incoherent and coherent cases, respectively,

$$V(C) = V(0)|D/w(C)|^{\rho G(0)}, \qquad (9)$$

$$V(C) = V(0)/[1 + G(0)\rho\ln|w(C)/D|], \qquad (10)$$

where $w(C) = C - E_f(C)$ and D is a cutoff parameter of the order of bandwidth (we put in numerical calculations $D = \rho^{-1} = 1$). Then, we have a closed equation for $w(C)$. In particular, for the incoherent regime,

$$\frac{\partial w(C)}{\partial C} = 1 + (N-1)\frac{\rho V^2(0)}{C}\left|\frac{D}{w(C)}\right|^{2\rho G(0)}. \qquad (11)$$

When E_f lies sufficiently below the Fermi level (the Kondo regime), the quantity $|w(C)|$ can become small with decreasing $|C|$. We can use this condition to define the boundary between IV and Kondo cases. The formal definition of IV systems is the absence of solutions to the equation $w(C) = 0$, which determines only the Kondo resonance (cf. [6, 16]). Physically, the Kondo lattice has a three-peak density of states (two Hubbard bands and the Kondo resonance), which is similar to the "doped Mott insulator" (note that, in the dynamical mean-field theory (DMFT), the Hubbard model is reduced to the Anderson impurity model [17]). On the other hand, IV state is similar to the phase of strongly correlated metal: the Kondo peak as a separate solution is absent.

For $G(0) = 0$, the boundary condition for the Kondo state is $|E_f(0)| > \Gamma = (N-1)\rho V^2(0)$. In the opposite IV case, $|w(C)|$ remains finite. For $G(0) \neq 0$, $V(C)$ increases during the renormalization process and the effective level width $\Gamma(C)$ becomes larger, so that the IV region becomes wider. A temperature dependence of the energy gap (an increase with decreasing temperature) in IV compounds was observed experimentally in

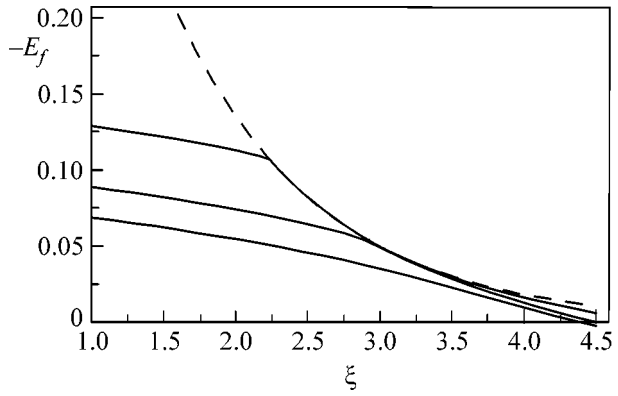

Fig. 1. Scaling trajectories $-E_f(\xi)$ for $V(0) = 0.1$, $G(0) = 0.1$, and $N = 2$ in the incoherent case as compared to the curve $|C|/D = \exp(-\xi)$ (dashed line). The parameter values (for the curves from below to above) are $E_f(0) = -0.08, -0.1, -0.14$.

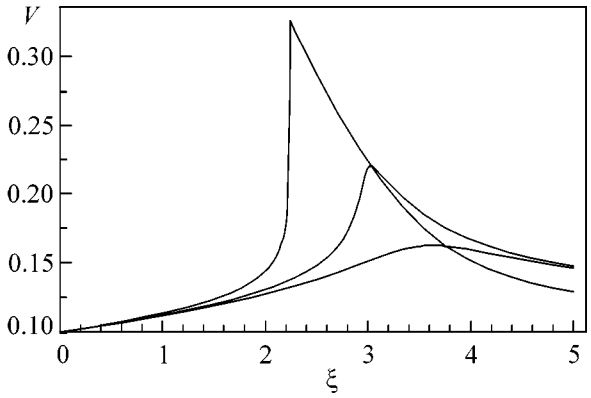

Fig. 2. Dependences $V(\xi)$ for the same parameter values as in Fig. 1 (for the curves from below to above).

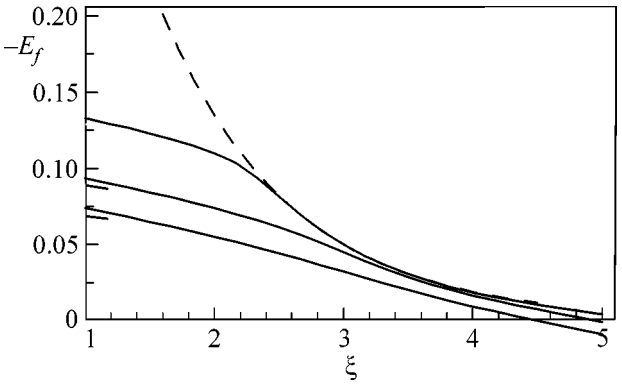

Fig. 3. Scaling trajectories $-E_f(\xi)$ for $V(0) = 0.05$, $G(0) = 0.05$, $N = 6$, $E_f(0) = -0.09, -0.11, -0.15$ in the coherent case.

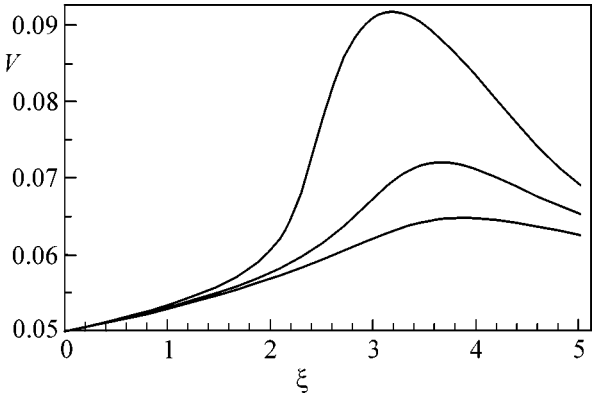

Fig. 4. Dependences $V(\xi)$ for the same parameter values as in Fig. 3.

SmB_6 [18], YbB_{12}, and Ce_4BiPt_3 [2]. According to our treatment, the dependence of the effective hybridization $V(C)$ is nonmonotonous: it passes through a maximum.

Now, we consider in more detail the incoherent case, which should be realized for diluted systems (the Anderson's localization prevents coherence at low temperatures). To present numerical results (Figs. 1–4), we use the variable $\xi = \ln|D/C|$. As follows from (9), in the Kondo case, the hybridization parameter $V(C)$ decreases practically by a jump when we approach the point $C = E_f(C)$ (see Fig. 2). With further decreasing of $|C|$, a considerable region arises where we have to high accuracy $C \cong E_f(C)$ (Fig. 1). More exactly, we have $\partial w(C)/\partial C \simeq 0$, so that we obtain, from (11), near the maximum of $w(C)$,

$$w(C) \simeq -D\left|(N-1)\rho V^2(0)/C\right|^{1/2\rho G(0)}. \qquad (12)$$

In this regime, $V(C) = |C/[(N-1)\rho]|^{1/2}$ and the effective s–f exchange parameter is $\rho I(C) = \rho V^2(C)/E_f(C) = -1/(N-1) = \text{const}$.

In a standard consideration, the condition $C = E_f(C)$ determines an energy scale for a crossover to the regime of a heavy-fermion (Kondo) local Fermi liquid [13]. The "marginal" situation with $E_f(C) \cong C$ in a whole interval of cutoff parameter C means an essentially non-Fermi-liquid (NFL) picture. A similar mechanism of NFL behavior in magnetic Kondo lattices was proposed in [7, 19], where a soft boson was obtained with the characteristic energy $\bar{\omega}(C) \cong |C|$. Note also that a regime with a rate on the order of parameter fluctuations $1/\tau_\phi(T) \propto T$ is typical near a quantum phase transition [20]. Our situation is reminiscent of this regime in the sense that the characteristic valence fluctuation frequency $\max(\rho V^2(T), |E_f(T)|)$ is proportional to T (after a natural replacement $|C| \longrightarrow T$).

Physically, a regime in which a typical energy scale is just the temperature means a *classical* (Maxwell–Boltzmann) electron gas (interacting with local momenta): the heat capacity is approximately constant, etc. Of course, in a pure form, this behavior is never observed, since, according to our results, it takes place only in a restricted temperature interval. However, we have a strong deviation from a simple scaling picture in which we just enter strong-coupling regime, the characteristic "Kondo" temperature being T-independent. In particular, the Wilson number is nearly constant, but differs considerably from that in the singlet state ($I_{ef} = -\infty$).

A similar "marginal" region in the dependence $E_f(C)$ occurs not only for the Kondo but also for the IV state near the critical line (in such a situation, the dependence $w(C)$ has a shallow minimum and $V(C)$ a sharp maximum; see Figs. 1, 2).

To estimate the Kondo temperature, we can use Haldane's arguments for the Anderson model with $N = 2$ [13]. The generalization to arbitrary N can be performed as (cf. [21])

$$T_K \simeq D(\rho|I|N)^{1/N}\exp(1/\rho NI), \quad I = V^2/E_f. \quad (13)$$

This expression is formally based on perturbation theory (two-loop scaling). However, Haldane noted that replacing in this formula both D and E_f by the characteristic energy scale $T^* = -C$, which is determined from the equation $C = E_f(C)$, yields the correct estimation for the Kondo temperature. As demonstrated above, in the presence of exciton effects (the Falicov–Kimball interaction G), a situation is possible in which this equation holds approximately in a whole energy interval. The energy scale T^*, where the marginal regime starts, is considerably changed by the exciton effects.

In the coherent case, the last term in Eq. (5) results in a smearing of the singularity, especially for small N. However, with increasing N, the dependence $E_f(C)$ (Fig. 3) becomes qualitatively similar to that in the incoherent case. On the other hand, the dependence $V(C)$ (Fig. 4) is essentially modified even for $N \longrightarrow \infty$. At $C \cong E_f(C)$, we have

$$1 = -(N-1)\rho V^2(C)/C - n[G(0)/V(0)]\partial V(C)/\partial C. \quad (14)$$

Solution to this Riccati equation is obtained in terms of the imaginary-argument Bessel and Macdonald functions $I_p(x)$ and $K_p(x)$ with $x = 2|(N-1)\rho V^2(0)C|^{1/2}/[nG(0)]$, $p = 0, 1$. For large N, the quantity $\partial V(C)/\partial C$ and, consequently, $V^2(\xi)/E_f(\xi)$ turn out to be practically ξ-linear near the maximum of $w(C)$. Thus, we have a *classical* electron liquid with singular interactions that have logarithmic energy dependences. With further decreasing $|C|$, we have, from Eq. (6),

$$\partial V(C)/\partial C \propto |C|^{-1/2} = |E_f(C)|^{-1/2} \quad (15)$$

so that the correction to $V^2(C)/E_f(C)$ is proportional to $|C|^{-1/2}$.

The d–f Coulomb interaction can strongly renormalize hybridization, which leads to the increase of a characteristic energy scale. In the incoherent regime, it is a width of the resonance; in the coherent one, the width of (indirect) gap or pseudogap [3]. The renormalization of the fluctuation rate $\rho V^2(C)$ can be very strong (about an order of magnitude for realistic parameters). The corresponding temperature dependences can be found in both regimes by the RG approach with the replacement $|C| \longrightarrow T$.

In standard treatments of HF systems, one picks usually anomalous magnetic contributions to thermodynamic properties and compares them with exact results in the one-impurity Kondo problem. In particular, the dependences of the crystal-field level width from both inelastic neutron scattering and nuclear magnetic resonance have the form $\Gamma(T) \propto T^{1/2}$. In the Kondo resonance model, such a behavior takes place above the Kondo temperature T_K, but in some cases (CeB_6, $CePd_3B_{0.6}$, and $YbBe_{13}$), the dependence $T^{1/2}$ takes place at very low temperatures of a few kelvins [22]. Further, the characteristic energy scale from γT-linear term in specific heat is of the order of tens of kelvins, whereas the temperature where γ starts to deviate from constant is just a few kelvins. Thus, there exists no unique energy scale. We have demonstrated that, indeed, the infrared behavior can be essentially different from that in the simple Anderson model owing to the spin dynamics (see [7, 19]) and charge fluctuations (exciton effects) considered in the present work.

Of course, the estimations performed are qualitative, since they are based on a continuation of a perturbative GellMann–Low scaling function to the strong coupling region. At the same time, the statement that exciton effects cannot be described by a universal temperature-independent T_K seems itself to be reliable. Recently, direct ways of observing the Kondo resonance (STM) were proposed [23]. As we know, they have not yet been applied to the IV systems. It would be interesting to compare the results for T_K of these new experimental methods with those from investigating thermodynamic properties.

The research described was supported in part by the Russian Foundation for Basic Research Program for Support of Scientific Schools (grant no. 747.2003.2), by the Program of the General Physics Division (grant no. 15), and by the Netherlands Organization for Scientific Research (grant no. NWO 047.016.005). The authors are grateful to the Department of Physics of Uppsala University for their hospitality during performance of the work.

REFERENCES

1. J. M. Lawrence, P. S. Riseborough, and R. D. Parks, Rep. Prog. Phys. **44**, 1 (1981).

2. P. S. Riseborough, Adv. Phys. **49**, 257 (2000).
3. V. Yu. Irkhin and M. I. Katsnelson, Sov. Phys. JETP **63**, 631 (1986).
4. *Valence Instabilities and Related Narrow-Band Phenomena*, Ed. by R. D. Parks (Plenum, New York, 1977).
5. *Proceedings of International Conference on Valence Fluctuations*; J. Magn. Magn. Mater. **47–48** (1985).
6. A. C. Hewson, *The Kondo Problem to Heavy Fermions* (Cambridge Univ. Press, Cambridge, 1993).
7. V. Yu. Irkhin and M. I. Katsnelson, Phys. Rev. B **56**, 8109 (1997).
8. R. Ramirez, L. M. Falicov, and J. C. Kimball, Phys. Rev. B **2**, 3383 (1970); C. E. T. Goncalves da Silva and L. M. Falicov, J. Phys. C **5**, 906 (1972).
9. K. W. H. Stevens, J. Phys. C **9**, 1417 (1976); J. Phys. C **11**, 985 (1978).
10. P. Schlottmann, Phys. Rev. B **22**, 613 (1980); Phys. Rev. B **22**, 622 (1980).
11. D. L. Cox and A. Zawadowski, Adv. Phys. **47**, 599 (1998).
12. V. Yu. Irkhin and Yu. P. Irkhin, JETP **80**, 334 (1995).
13. F. D. M. Haldane, Phys. Rev. Lett. **40**, 416 (1978).
14. V. Yu. Irkhin and M. I. Katsnelson, Z. Phys. B **75**, 67 (1989).
15. P. W. Anderson, J. Phys. C **3**, 2346 (1970).
16. N. E. Bickers, Rev. Mod. Phys. **59**, 845 (1987); O. Gunnarsson and K. Schönhammer, Phys. Rev. B **28**, 4315 (1983).
17. A. Georges *et al.*, Rev. Mod. Phys. **68**, 13 (1996).
18. T. S. Al'tshuler *et al.*, JETP Lett. **40**, 754 (1984).
19. V. Yu. Irkhin and M. I. Katsnelson, Phys. Rev. B **61**, 14 640 (2000).
20. S. Sachdev, *Quantum Phase Transitions* (Cambridge Univ. Press, Cambridge, 1999).
21. J. W. Rasul and A. C. Hewson, J. Phys. C **17**, 2555 (1984).
22. P. Panissod *et al.*, J. Phys. (Paris) **C49**, 685 (1988).
23. V. Madhavan *et al.*, Science **280**, 567 (1998).

JETP Letters, Vol. 80, No. 5, 2004, pp. 317–320. Translated from Pis'ma v Zhurnal Éksperimental'noĭ i Teoreticheskoĭ Fiziki, Vol. 80, No. 5, 2004, pp. 363–366.

Giant Fluctuations of Radiation Intensity of Two-Dimensional Electrons in Double Quantum Wells

M. V. Lebedev, O. V. Volkov, A. L. Parakhonskiĭ, V. A. Koval'skiĭ, and I. V. Kukushkin

Institute of Solid-State Physics, Russian Academy of Sciences, Chernogolovka, Moscow region, 142432 Russia

Received July 16, 2004

Giant fluctuations of the recombination-radiation intensity of two-dimensional electrons were studied in double quantum wells with different well and barrier widths in the regime of the integer quantum Hall effect. It was found that the giant fluctuations of photoluminescence intensity in double quantum wells with a narrow barrier (l < 150 Å) occur in a narrow magnetic-field interval, where the sum of electron concentrations in both wells corresponds to the integer filling factors 4, 8, and 12. It was established that, under these conditions, the coefficient C_{12} of correlation between the radiation intensities from different wells is close to unity. It is shown that, as the barrier width increases (l > 200 Å), the coefficient C_{12} decreases, changes sign, and goes to zero at l = 400 Å. © *2004 MAIK "Nauka/Interperiodica".*

PACS numbers: 11.25.Hf, 11.30.Pb

1. In our previous studies of the giant fluctuations of recombination radiation in a system of two-dimensional electrons under conditions of the quantum Hall effect, we focused on the photoluminescence spectra of single quantum wells (QWs) [1, 2]. It was established that, under the conditions when this effect was observed, the recombination processes correlated at macroscopic distances with a characteristic correlation length of 1–2 mm [2]. One of the possible explanations of this phenomenon is that a new coherent macroscopic state with a collective wave function arises in the electron system. Analysis of the spatial correlations between the recombination-radiation intensities at different points of the sample performed using two light guides [2] showed that, upon the artificial separation of a 2D system into two subsystems by a potential barrier in the sample plane, the collective character of the macroscopic wave function of the electron system is destroyed, and the correlations disappear. Apart from the possibility of forming a potential barrier in the 2D plane, there is an alternative possibility of separating electron systems in the perpendicular direction, which is realized in double quantum wells. The electron-tunneling time between the wells in the coupled double quantum wells (DQWs) can be varied by varying the barrier width and, hence, the electron systems can be effectively separated by destroying the collective wave function. In this work, the correlations between the photoluminescence intensities of two QWs are studied in the regime of giant fluctuations for different potential barrier widths between the wells.

2. The samples studied in this work were grown by molecular-beam epitaxy. An undoped GaAs/$Al_{0.3}Ga_{0.7}As$ superlattice with a total thickness of about 13000 Å was grown on a GaAs substrate, whereupon a system of two GaAs quantum wells with thicknesses L = 150–300 Å separated by barriers of different width (l = 50–600 Å) was formed. The double quantum wells were surrounded at two sides by 400-Å-thick $Al_{0.3}Ga_{0.7}As$ spacers and 650-Å-thick layers of doped $Al_{0.3}Ga_{0.7}As$ ($N \sim 10^{18}$ cm^{-3}). The 2D-electron mobility in the structures studied was 10^6 cm^2/(V s). The structure parameters are given in the table.

The photoexcitation was performed using a laser LED with a photon energy of 1.653 eV. A Kaderk monochromator provided a spectral resolution of 0.03 meV. The photoluminescence signal was detected using a CCD semiconductor detector. The sample was placed in a helium cryostat (at T = 1.5 K) inside a superconducting solenoid that produced a magnetic field of up to 12 T. The excitation of photoluminescence signals and their collection was accomplished using one of the light guides. To detect separately the photoluminescence (PL) signals of 2D electrons from different wells, we used the fact that the radiations from the wells with different widths or different electron densities are spectrally separated. With the object of unbalancing the electron densities in the wells, we used an additional He–Ne laser irradiation (with a wavelength of 633 nm).

Table

DQW no.	L_1, Å	L_2, Å	l, Å	N_S, cm^{-2}
1	220	300	50	7.3×10^{11}
2	250	250	200	4.3×10^{11}
3	150	150	200	4.8×10^{11}
4	250	300	400	4.7×10^{11}
5	200	200	600	8.3×10^{11}

0021-3640/04/8005-0317$26.00

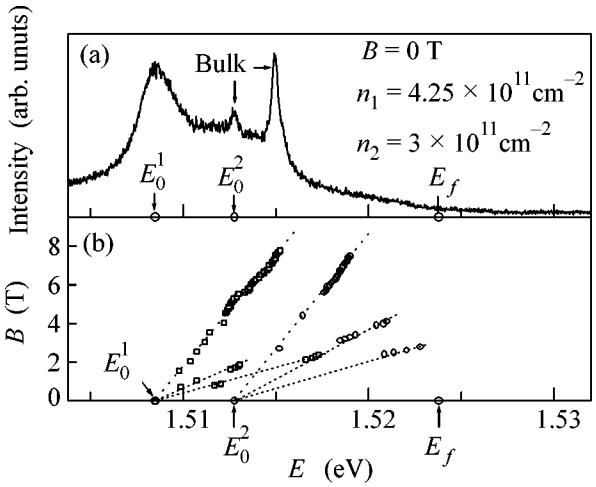

Fig. 1. (a) Zero-field photoluminescence spectrum measured for a double quantum well 220/50/300 at a temperature of 1.5 K, and (b) magnetic-field dependences of the Landau energy levels. Arrows indicate the lowest size-quantization energy levels E_0^1 and E_0^2 in the wells and the Fermi energy E_F.

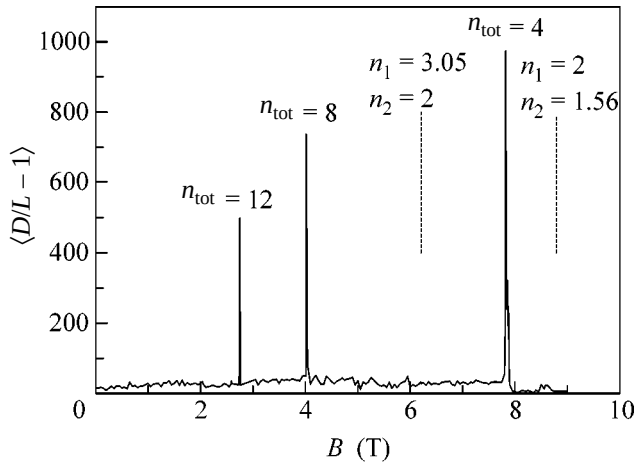

Fig. 2. Magnetic-field dependence of the variance-to-mean integrated intensity ratio measured for a double quantum well with the barrier width $l = 50$ Å. The noise variance is anomalously large when the total filling factor ($\nu_{tot} = \nu_1 + \nu_2$) becomes integer $\nu_{tot} = 4$ ($B \approx 8$ T), 8 ($B \approx 4$ T), and 12 ($B \approx 2.7$ T). The dotted lines indicate the values of magnetic field ($B = 6.21$ and 8.8 T) for which the filling factor in the first and second wells is $\nu = 2$.

This additional photoexcitation was mainly absorbed in the near-surface AlGaAs layer and reduced the electron concentration in the well that was situated closer to the structure surface [3]. Simultaneously with the recording of the PL spectra, they were mathematically processed. The mean intensities $\langle I_{1,2} \rangle$ obtained for the two wells in a measurement time, the variances $D_{1,2} = \langle \Delta I_{1,2}^2 \rangle$, the ratios $D_{1,2}/\langle I_{1,2} \rangle$ of the variance to the mean intensity, and the coefficient of correlation $C_{12} = \langle \Delta I_1 \Delta I_2 \rangle / (D_1 D_2)^{1/2}$ were estimated.

3. As in the case of a single quantum well (SQW), the giant fluctuations in the DQW structures were observed near the characteristic discontinuities in the spectral positions of the lines arising in the integer Hall-effect regime. In the structures with a narrow barrier ($l < 150$ Å), this regime occurred simultaneously for both wells, i.e., at the same magnetic field. A system of two-dimensional electrons in double quantum wells is characterized by two concentrations, because, due to the interwell tunneling, the symmetric and antisymmetric electronic states are energy-split [4, 5]. As a result, the degeneracy caused by the presence of two quantum wells is removed in the electron-energy spectrum, and the electron Fermi surface proves to consist of two circles corresponding to two different Fermi quasimomenta (and, hence, to two different electron concentrations) [5]. The narrower the barrier, the higher the tunneling probability, the greater the energy splitting, and the stronger the distinctions between the Fermi quasimomenta and between the electron densities. Both electron densities could be determined separately using the standard technique [6] of analyzing the Landau-level fans in the luminescence spectra recorded at a temperature of 1.5 K in a perpendicular magnetic field. As an example, Fig. 1 shows the photoluminescence spectrum measured for the structure with a barrier $l = 50$ Å in zero magnetic field and the field dependences of the Landau energy levels. These curves can be used to determine the energy positions E_0^1 and E_0^2 of the lowest size-quantization levels in the wells, the Fermi energy E_F, and the tunneling splitting. The concentrations of 2D electrons thus defined for both wells are 4.25×10^{11} and 3×10^{11} cm^{-2}, respectively. A similar procedure for determining the electron concentrations could be used for all the studied structures, as well as under the conditions of the additional illumination, in which case the concentration could be changed in only one of the wells. For this purpose, we used the light from a He–Ne laser to reduce the electron concentration in the quantum well situated closer to the sample surface [3].

In Fig. 2, the field dependences of the ratio of variance to the mean integrated intensity (integration over the entire spectrum) are shown for the structure with a barrier $l = 50$ Å. One can see from this figure that, as in the case of a single quantum well, anomalously large fluctuations of the radiative 2D-electron-recombination intensity are also observed for the double quantum wells, although in very narrow magnetic-field intervals, and the noise dispersion is maximal in the fields for which the total factor $\nu_{tot} = \nu_1 + \nu_2$ has the integer values 4, 8, and 12. The absence of singularities for the filling factors 6 and 10 suggests that the Landau levels are fourfold degenerate (in spin and pseudospin or in the well index [7]). One more important feature of the observed giant fluctuations is that the filling factors determined for each of the wells from two concentra-

tions are not integers at the resonance field values. At the same time, in fields corresponding to the integer filling factors of the "individual" wells, the noise has the usual Poisson character. Analogous results were also obtained for the structures with wider barriers (l < 200 Å), whereas the character of observed dependences is distinctly different for the samples with the widest barriers (l = 400 and 600 Å) (see below).

4. The use of quantum wells of different widths allowed us to measure separately the properties of recombination radiation from different wells. This was achieved due to the fact that, because of a heavy hole mass, holes were well separated among the wells at l > 50 Å, and the difference in the electron and hole size-quantization energies resulted in an appreciable spectral shift of emission lines from the different wells. As a result, the correlation analysis of only two lines in the emission spectrum suffices to determine the coefficient of correlation between the fluctuations measured in different wells. Similar correlation measurements could also be made for the structures with identical wells, but, only under the conditions where the electron concentrations were markedly different due to the additional photoexcitation by the He–Ne laser.

The spectrum and the ratio $D_{1,2}/\langle I_{1,2}\rangle$ (B = 7.82 T) measured at a temperature of 1.5 K for the sample with the barrier width l = 50 Å are shown in Fig. 3. The correlation C_{12} was calculated between the fluctuations of the recombination lines corresponding to the lower spin sublevels of the ground-state size-quantization subbands of each of the two wells (lines at 1.515 and 1.519 eV, respectively). The radiation intensities of both wells almost fully correlate (C_{12} = 0.98). The coefficient of correlation between the radiation intensities of one of the wells and its first excited subband (1SB) C_{0SB1} was also calculated. This value proved to be close to –1; i.e., the fluctuations in the ground and first excited subbands, in effect, anticorrelate. It should be noted that the minima of the $D_1/\langle I_1\rangle$ ratio correspond to the maxima of the luminescence lines in the first well; i.e., the fluctuations are caused, to a large extent, by a change in the positions of spectral lines. The luminescence fluctuations of the second well proceed without any significant changes in the line positions.

In the double quantum wells with barrier l = 200 Å, the giant intensity fluctuations were also observed in the luminescence spectra at ν_{tot} = 4, 8, and 12. In the course of recording the PL spectra of this system, negative C_{12} values (–0.56) were obtained near the filling factor ν_{tot} = 4. Inasmuch as the wells in this sample had identical widths, we applied an additional illumination from the He–Ne laser to achieve the desired spectral resolution for the emission lines from the different wells. In contrast to ν_{tot} = 4, the values of C_{12} were positive near the filling factor ν_{tot} = 8. The fact that the sign of the correlation coefficient C_{12} changes with the changing of the barrier width and filling factor suggests

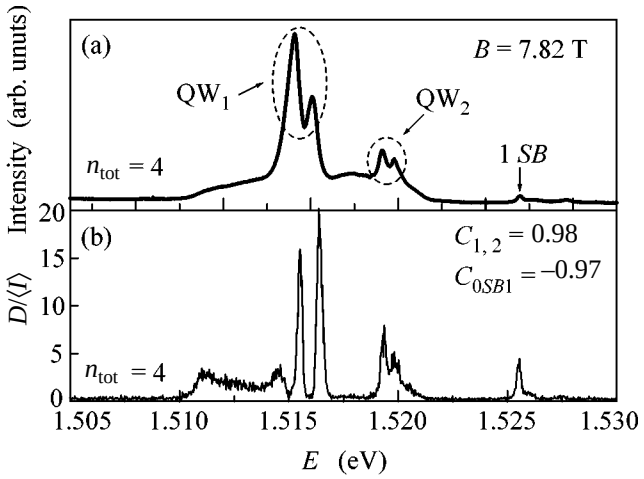

Fig. 3. (a) Luminescence and (b) noise spectra measured at B = 7.82 T for a double quantum well with the barrier width l = 50 Å (ν_{tot} = 4). The radiation intensities from both wells almost fully correlate with each other (C_{12} = 0.98) and anticorrelate with the radiation intensity from the first excited subband (C_{0SB1} = – 0.97).

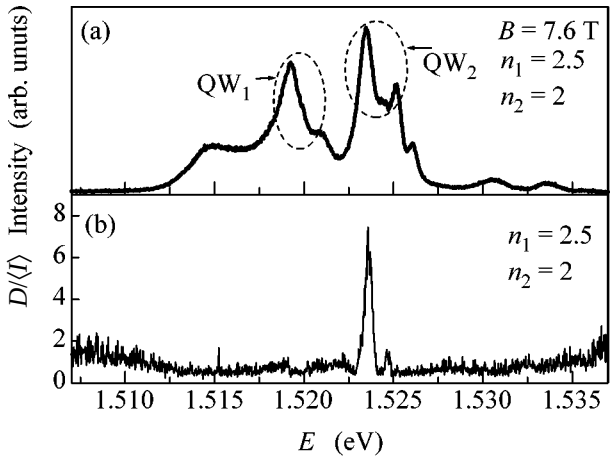

Fig. 4. The (a) luminescence and (b) noise spectra measured at B = 7.6 T for a double quantum well with the barrier width l = 600 Å. It is seen that only one of the wells produces noise (at ν_2 = 2), which illustrates the absence of correlation between the fluctuations of radiative recombination in the wells.

that the correlation effects depend in an oscillatory fashion on the interwell-tunneling probability. This fact may be indicative of the relationship between the observed phenomenon and the Josephson effect in the SNS structures and may also be evidence of the appearance of a new coherent macroscopic electronic state possessing a collective wave function in the regime of the quantum Hall effect.

In the structures with l = 400 Å, the intensity fluctuations in the two neighboring wells, as before, noticeably exceeded the Poisson noise, but the coefficient C_{12}

was close to zero; i.e., the fluctuations did not correlate. One cannot apply the term "total filling factor" to the double quantum wells with the widest (l = 600 Å) barrier, because the radiation-intensity fluctuations in the wells were independent of each other and developed when the filling factor for one of the wells was equal to 2, 4, or 6. The fluctuation amplitude in this structure was appreciably lower than in the structures with the narrower barriers, and only the fluctuations of the emission line with a maximum near 1.523 eV, corresponding to the 2D-electron recombination in the well situated farther from the surface, were mainly observed (Fig. 4).

5. Thus, the results obtained in this work show that, as the width of the potential barrier between two quantum wells increases, the character of giant luminescence-intensity fluctuations that have arisen under the conditions of the quantum Hall effect changes. In structures with a narrow (l = 50 Å) barrier, the fluctuations in two neighboring quantum wells fully correlate. As the barrier width increases from 50 to 200 Å for the filling factor $\nu_{tot} = 4$, the correlation coefficient C_{12} takes negative values, decreases in magnitude, and becomes virtually zero upon the further increase in the barrier width to 400 Å. One can assume that, in the case of a narrow potential barrier (l = 50 Å), the positive coefficient of correlation obtained for both $\nu_{tot} = 4$ and 8 stems from the collective wave function with the same phase in both neighboring wells. As the barrier width increases to l = 200 Å, a phase difference may arise between the layer wave functions, resulting in the anticorrelation of the noises from different wells. For the structures with barrier $l \geq 400$ Å, the overlap between the wave functions of the two neighboring wells is insignificant and C_{12} tends to zero. It is conceivable that the change in the sign of C_{12} in the structures with l = 200 Å upon the transition from $\nu_{tot} = 8$ to 4 is caused by the change in the symmetry of the electron wave function.

REFERENCES

1. O. V. Volkoy, I. V. Kukushkin, M. V. Lebedev, *et al.*, Pis'ma Zh. Éksp. Teor. Fiz. **71**, 558 (2000) [JETP Lett. **71**, 383 (2000)].
2. M. V. Lebedev, I. V. Kukushkin, and O. V. Volkov, Pis'ma Zh. Éksp. Teor. Fiz. **77**, 345 (2003) [JETP Lett. **77**, 295 (2003)].
3. I. V. Kukushkin, K. von Klitzing, K. Ploog, *et al.*, Phys. Rev. B **40**, 4179 (1989).
4. G. S. Boebinger, H. W. Jiang, L. N. Pfeiffer, and K. W. West, Phys. Rev. Lett. **64**, 1793 (1990).
5. J. P. Eisenstein, G. S. Boebinger, L. N. Pfeiffer, *et al.*, Phys. Rev. Lett. **68**, 1383 (1992).
6. S. V. Tovstonog, I. V. Kukushkin, L. V. Kulik, and V. E. Kirpichev, Pis'ma Zh. Éksp. Teor. Fiz. **76**, 592 (2002) [JETP Lett. **76**, 511 (2002)].
7. K. Moon, H. Mori, K. Yang, *et al.*, Phys. Rev. B **51**, 5138 (1995).

Translated by V. Sakun

JETP Letters, Vol. 80, No. 5, 2004, pp. 321–325. Translated from Pis'ma v Zhurnal Éksperimental'noĭ i Teoreticheskoĭ Fiziki, Vol. 80, No. 5, 2004, pp. 367–371.

The Meyer–Neldel Rule in the Processes of Thermal Emission and Hole Capture in Ge/Si Quantum Dots

A. I. Yakimov[1, *], A. V. Dvurechenskiĭ[1], A. I. Nikiforov[1], and G. Yu. Mikhalev[2]

[1] *Institute of Semiconductor Physics, Siberian Division, Russian Academy of Sciences, pr. Akademika Lavrent'eva 13, Novosibirsk, 630090 Russia*

**e-mail: yakimov@isp.nsc.ru*

[2] *Novosibirsk State University, ul. Pirogova 2, Novosibirsk, 630090 Russia*

Received June 16, 2004; in final form, July 19, 2004

The hole thermal-emission rates and the cross sections for hole capture to the bound states in Ge quantum dots in Si are determined by admittance spectroscopy. The capture cross sections and the activation energies for emission rate are found to be related to each other by the Meyer–Neldel rule with a characteristic energy of 27 ± 3 meV, which does not depend on the quantum-dot size. It is established that the capture cross section changes with temperature following the activation law. The experimental data are evidence of a unified multiphonon mechanism for the activation processes of hole transitions from the Ge quantum dots to the Si valence band and hole capture back into the quantum dots. © *2004 MAIK "Nauka/Interperiodica".*

PACS numbers: 73.20.Mf; 73.50.Pz

The charge-carrier excitation and recombination processes in heterostructures with quantum dots (QDs) play a key role in the operation of new-generation devices, such as lasers and photodetectors based on quantum effects in low-dimensional systems. If electrons are emitted from the bound states to the allowed band, energy can be absorbed, and if charge carriers are captured from the allowed band to the QD bound states, energy should be evolved. The main questions are (i) what is the source of this energy, (ii) to what excitations it is transferred, and (iii) what is the energy-transfer mechanism? For example, the capture to the local levels formed by the impurity centers and defects in semiconductors can be controlled by either the Auger processes or by the emission of a large number of phonons in one event, or by the cascade mechanism through the intermediate states (see [1] and references therein). In this study, we used admittance spectroscopy to determine the hole-capture cross sections and hole thermal-emission rates from the bound states in the Ge/Si QD layers to the continuous-spectrum states. The conclusion is drawn that the QD thermal ionization and the hole capture by QDs are multiphonon processes.

Samples were grown by molecular-beam epitaxy on the p^+-Si(001) substrates with a resistivity of 0.005 Ω cm doped with boron to a concentration of ~10^{19} cm^{-3}. Ge layers of different thicknesses d_{eff} (d_{eff} = 0, 6, 8, and 10 monolayers (MLs); 1 ML = 1.4 Å) were epitaxially introduced inside the p-Si layer (B concentration 5×10^{16} cm^{-3}; layer thickness 0.7 μm) at a distance of 0.4 μm from the substrate. The formation of Schottky diodes was completed by the vacuum deposition of a Ti film on the sample surface. The area of the Ti contact was 4.4×10^{-3} cm^2. The high-energy electron diffraction patterns of the surfaces of Ge island films (d_{eff} = 6, 8, and 10 ML) showed that the Ge nanoclusters had a pyramid shape. The average sizes of the Ge nanocluster bases in the growth plane, as determined by high-resolution electron microscopy, were 8, 10, and 15 nm for d_{eff} = 6, 8, and 10 ML, respectively. The height-to-base ratio was about 1 : 10. The sheet density of nanoclusters was $(3–4) \times 10^{11}$ cm^{-2}.

The admittance was measured using a Fluke PM6306 RCL Meter bridge in the frequency range 10–300 kHz at temperatures from 77 to 300 K. The amplitude of the ac component of the applied voltage was 25 meV.

By analogy with the deep-level transient spectroscopy (DLTS) of semiconductors [2, 3], admittance spectroscopy of structures with QDs is based on measuring the admittance arising upon the QD charge exchange due to the emission of charge carriers from QD to the allowed band and their capture to the localized states in QD. Let us consider this situation by an example of a Ti/p-Si/p^+-Si Schottky diode with a layer of Ge QDs introduced into the p-Si base region (Fig. 1). As the reverse bias U_b (positive and negative polarities of the Ti contact and p^+-Si substrate, respectively) changes, the hole energy levels in Ge QDs shift with respect to the Fermi level E_F in the p^+-Si layer, leading to a change in the hole filling factor in QDs. The ac component of the voltage applied to the diode stimulates the emission of holes from the levels located near E_F to the valence band of Si during the first half-period and the hole capture to the bound states in QDs during

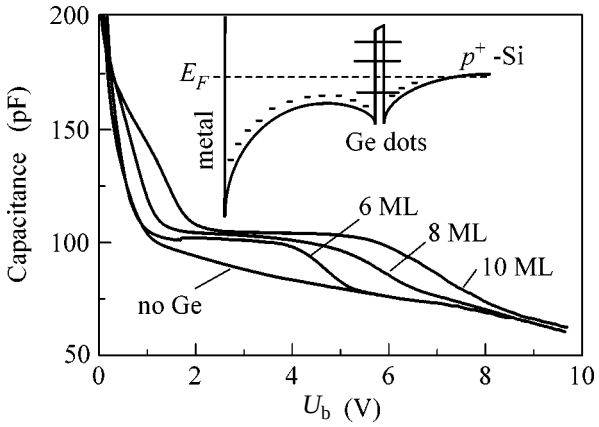

Fig. 1. Dependence of the capacitance on reverse bias for samples with deposited Ge layers of different thickness. Measurements at room temperature at frequency f = 100 kHz. Thicknesses of Ge layers are given in monolayers. Inset shows the valence-band profile of a Si Schottky diode with a layer of Ge QDs built into the base.

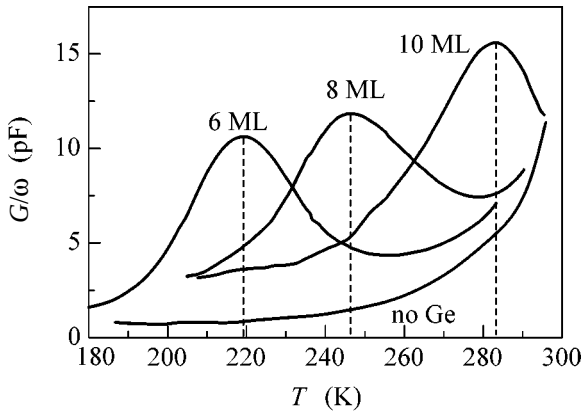

Fig. 2. Temperature dependences of the conductance of the samples with deposited Ge layers of different thickness. Measurements are at U_b = 2 V at frequency f = 50 kHz.

the second half-period. According to the detailed balancing principle, the thermal emission rate can be written as [2, 3]

$$e_n(T) = (1/g_t)\sigma_p(T)\langle v_{th}\rangle N_v \exp\left(-\frac{E_i}{k_B T}\right), \qquad (1)$$

where g_t is the degeneracy factor, σ_p is the effective cross section for hole capture into QDs, $\langle v_{th}\rangle$ is the average thermal velocity of the holes, N_v is the effective density of states in the Si valence band, E_i is the hole energy level in a Ge QD (counted from the valence band top in Si), k_B is the Boltzmann constant, and T is temperature. In the general case, the temperature dependence of the capture cross section can follow the activation law [1, 4–6]: $\sigma_p(T) = \sigma_{p0}\exp(-E_\sigma/k_B T)$. Taking into account this circumstance and using the expressions $N_v = 2(2\pi m^* k_B T/h^2)^{3/2}$ and $\langle v_{th}\rangle = (8k_B T/\pi m^*)^{1/2}$ (where m^* is the effective mass of the density of states and h is Planck's constant), we can write

$$e_n(T) = \frac{16\pi m^* k_B^2}{g_t h^3}\sigma_{p0}T^2 \exp\left(-\frac{E_a}{k_B T}\right), \qquad (2)$$

where $E_a = E_i + E_\sigma$. In experiments, the temperature dependence of the admittance G is measured at a fixed reverse bias U_b and frequency f of the probe ac voltage. The dynamic admittance, which is related to the charge exchange in QDs, should be highest at the temperature T_m satisfying the condition [7]

$$e_n(T_m) \simeq \omega/2, \qquad (3)$$

where $\omega = 2\pi f$. At lower temperatures, when $e_n(T) \ll \omega$, holes are frozen at the QD levels; therefore, the admittance is low. At high temperatures, the corresponding hole levels are depleted and do not contribute to the conductance. As a result, G tends to zero again. By determining T_m experimentally at different fixed frequencies ω, we can find the temperature dependence of the thermal emission rate $e_n(T)$ and then, plotting the dependences of $\ln(e_n/T_m^2)$ on T_m^{-1} according to expression (2), determine the activation energy E_a and the preexponential factor for the capture cross section σ_{p0}.

Figure 1 shows the capacitance–voltage (C–V) characteristics of the samples with deposited Ge layers of different thickness d_{eff}. The measurements were performed at room temperature at a frequency f = 100 kHz. The dependence of the capacitance on reverse bias for the sample without a Ge layer shows no specific features and has the form of the conventional C–V characteristic of a Schottky contact with a p-type semiconductor. The capacitance–voltage curves of the samples with Ge QDs show characteristic steps caused by the additional capacitance that is due to a change of the charge in the QD layer [8–10]. At zero bias, QDs accumulate holes and become positively charged. At $U_b > 4$, 5, and 6 V for d_{eff} = 6, 8, and 10 ML, respectively, holes escape from QDs and the latter become neutral.

Figure 2 shows the temperature dependences of the conductance normalized to frequency for different samples. The curves were measured at U_b = 2 V and f = 50 kHz. As in the case of C–V characteristics, the conductance of the sample without Ge QDs shows no specific features. For the Schottky diodes with QDs, the $G(T)$ curves contain maxima, which shift to higher temperatures with increasing QD size. Let us rewrite Eq. (2) in the form

$$T_m = \frac{E_i + E_\sigma}{k_B \ln(T_m^2 A/e_n(T_m))}, \qquad (4)$$

where $A = 16\pi m^* k_B^2 \sigma_{p0}/g_t h^3$. It can be seen from Eq. (4) that the increase in the value of T_m corresponding to the highest conductance can be explained either by a shift of the hole-level energy E_i in QDs from the top of the Si valence band with increasing QD size (d_{eff}) or by a decrease in the capture cross section. Looking ahead (see Figs. 5, 6), we note that both of these factors are at work.

Figure 3 shows the temperature dependences of the conductance of the sample with d_{eff} = 6 ML. Similar curves were obtained for the samples with Ge layers of other thicknesses. The behavior of $G(T)$ can be qualitatively explained as follows. At a fixed bias U_b, the hole level in QD coinciding with the Fermi level in the p^+-Si substrate undergoes charge exchange. The rate of hole emission from this level decreases with decreasing temperature; therefore, with a decrease in the probe-voltage frequency, the condition for the maximum conductance (3) is satisfied at lower temperatures (Fig. 3a).

With an increase in reverse bias, the holes localized at deeper QD levels, for which condition (3) at a fixed frequency is satisfied at higher temperatures, contribute to the conductance. For this reason, the conductance peak in Fig. 3b shifts to higher temperatures with increasing U_b. At $U_b > 4$ V, Ge QDs become completely depleted and the maximum on the $G(T)$ curve, which is related to the charge exchange in QDs, disappears. At the same bias, the end of the plateau is observed on the C–V characteristic of the sample with d_{eff} = 6 ML (Fig. 1).

Figure 4 shows the typical dependences $e_n/T_m^2(T_m^{-1})$ for d_{eff} = 8 ML, plotted in semilogarithmic coordinates. The activation energies E_a of the hole-emission rate were found from the slope of the approximating straight lines, and the preexponential factor of the capture cross section σ_{p0} was determined from the point of intersection of the approximating lines and the ordinate axis. The resulting values of E_a are shown in Fig. 5. We should note two circumstances. First, the activation energy tends to change discretely with variation in the reverse bias. This is especially pronounced for the sample with d_{eff} = 8 ML. Apparently, such a behavior is due to the discrete spectrum of holes in Ge QDs. Second, the value of E_a for all samples exceeds the available theoretical and experimental values of the hole-level energies in Ge QDs with sizes considered here. For example, the ground-state hole energy in a Ge QD with a lateral size of 15 nm (d_{eff} = 10 ML) is about 400 meV [11–14], whereas the maximum activation energy in the emission rate is ≈700 meV. This means that $E_\sigma \approx$ 300 meV; i.e., the temperature dependence of the capture cross section follows the activation law. Previously, the same values of E_σ (≈300 meV) were obtained for structures with InAs/GaAs QDs by DLTS [5]. According to the existing theoretical concepts [1, 4] the strong (activation) temperature dependence of the capture

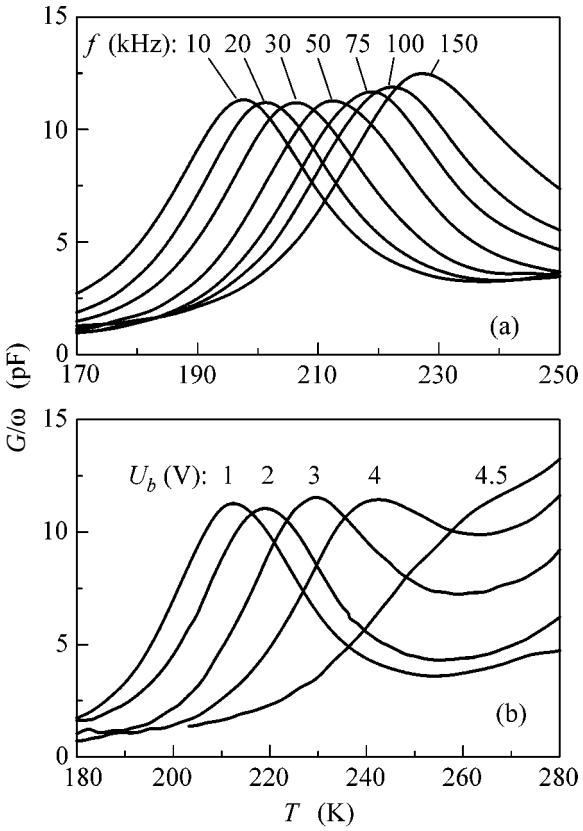

Fig. 3. Temperature dependences of the conductance of the sample containing a Ge layer with thickness d_{eff} = 6 ML. Measurements with (a) a fixed reverse bias U_b = 1 V and different probe voltage frequencies and (b) a fixed frequency f = 50 kHz and different reverse biases.

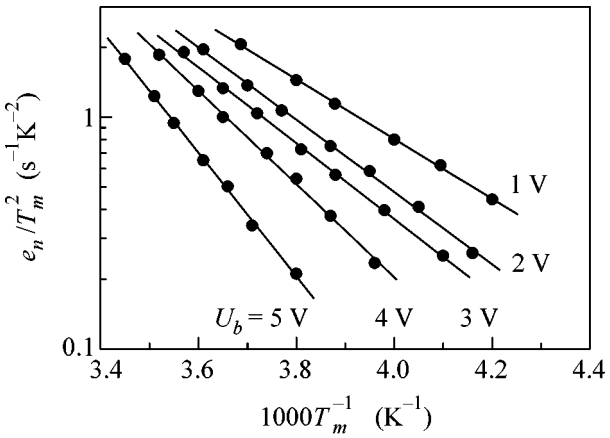

Fig. 4. Temperature dependence of the emission rate normalized to squared temperature, e_m/T_m^2, for the sample with d_{eff} = 8 ML, plotted in the Arrhenius coordinates for different reverse biases.

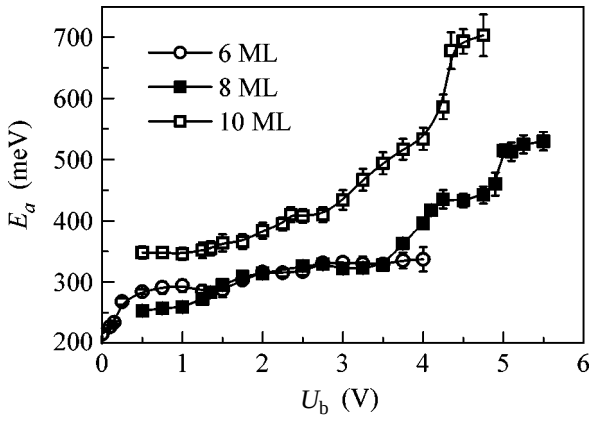

Fig. 5. Dependences of the activation energy of the rate of hole emission from Ge QDs to the Si valence band on the reverse bias for samples with deposited Ge layers of different thicknesses.

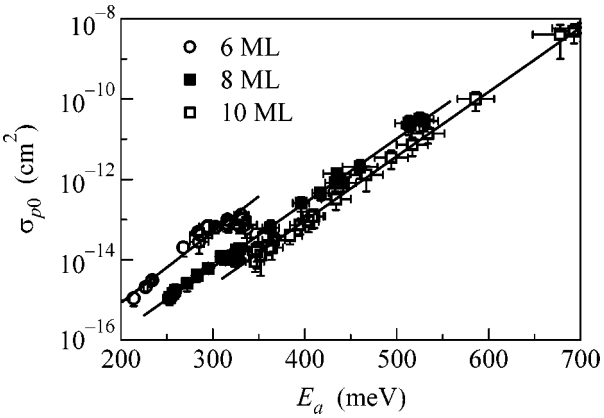

Fig. 6. Dependence of the capture cross section σ_{p0} on the activation energy of the hole emission from Ge QDs to the Si valence band, which demonstrates that the Meyer–Neldel rule is valid for samples with deposited Ge layers of different thicknesses.

cross section is evidence of a multiphonon capture mechanism. Within this model, thermal lattice vibrations lead to fluctuations of the depth and width of the potential well and, therefore, change the position of the electron energy level in this well. There is a nonzero probability for the fluctuating level to appear inside the continuous spectrum of the allowed band, after which a free electron may pass to this level. Then, the vibrational excitation of the system will relax over the entire volume of the crystal. In this case, the activation energy for capture is the minimum excitation energy of a lattice configuration that ensures the local-level entry into the band of delocalized states.

The most important result of this study is the revelation of a relationship between the capture cross section and the activation energy of the emission rate obeying the Meyer–Neldel rule. The Meyer–Neldel relation, which was established for the conductance of powder semiconductors [15], represents the exponential dependence of the activation energy E_a for a thermally activated process on the preexponential factor ν_0 of the same process: $\nu_0 = \nu_{00}\exp(E_a/E_0)$. This relation is valid for a great variety of phenomena in many different systems, for example, annealing metastable defects in *a*-Si:H [16]; conduction in *a*-Si:H [17], *a*-Si:Me alloys [18], porous Si [19], and fullerenes [20]; and electron ejection from traps associated with defects in binary and ternary alloys [21].

Figure 6 shows the experimental values of σ_{p0} corresponding to different values of E_a. The Meyer–Neldel relation $\sigma_{p0} = \sigma_{00}\exp(E_a/E_0)$ is valid for σ_{p0} ranging within seven orders of magnitude. The value of σ_{00} decreases with increasing d_{eff} and takes the values $(2.9 \pm 1.4) \times 10^{-19}$, $(1.1 \pm 0.4) \times 10^{-19}$, and $(4.1 \pm 1.7) \times 10^{-20}$ cm^2 for $d_{\text{eff}} = 6$, 8, and 10 ML, respectively. However, the characteristic energy E_0, determined from the slope of the $\sigma_{p0}(E_a)$ curves, is independent of the QD size (d_{eff}) and has the same value $E_0 = 27 \pm 3$ meV for all samples with QDs.

Most mechanisms (such as the dispersion transport [16], the statistical shift of the Fermi level and the temperature shift of percolation thresholds [22, 23], and the defect-controlled relaxation [24], etc.) that are used to explain the validity of the Meyer–Neldel relation for various disordered systems imply the exponential distribution of the trap energies [25] or potential barrier heights [24] in a system. Since the density of states in QDs is an oscillating rather than an exponential function of energy, these mechanisms are invalid in the case under consideration. It is also very difficult to explain within the framework of these models why the energy E_0 is independent of d_{eff}. In addition, the change in the parameter σ_{00} with the retention of the E_a value contradicts the conclusions drawn in [24, 25].

In our opinion, the experimental results obtained by us can be more adequately described by the mechanism of many-particle excitations proposed in [26–28]. In this case, the Meyer–Neldel rule is a natural consequence of the linear relationship between the free energy, enthalpy, and entropy of the many-quasiparticle system. If such excitations are phonons (which, apparently, holds true for the system studied), then $E_0 = E_{\text{ph}}/\ln N$, where E_{ph} is the phonon energy and N is the number of phonons involved in a thermally activated process [27]. Thus, to a logarithmic correction, the characteristic energy E_0 is nothing but the phonon energy. The energy of an optical phonon in Ge is equal to 38 meV and only weakly depends on the QD size if the latter is much larger than the interatomic distance. Indeed, this value is close to the experimental value of E_0 (27 meV). Using the relation between E_0 and E_{ph}, we obtain a reasonable estimate: $N = 4$.

Thus, both processes in layers of Ge/Si QDs—the emission of holes from QDs and their capture into QDs—can be described in terms of the same multiphonon mechanism.

This study was supported by the Russian Foundation for Basic Research (project no. 03-02-16526) and the program of the President of the Russian Federation in support of young doctors of science (grant no. MD-28-2003-02).

REFERENCES

1. V. N. Abakumov, V. I. Perel', and I. N. Yassievich, *Nonradiative Recombination in Semiconductors* (S.-Peterb. Inst. Yad. Fiz. Ross. Akad. Nauk, St. Petersburg, 1997) [in Russian].
2. D. V. Lang, J. Appl. Phys. **45**, 3023 (1974).
3. K. Dmowski, B. Lepley, E. Losson, and M. El Bouabdellati, J. Appl. Phys. **74**, 3936 (1993).
4. C. H. Henry and D. V. Lang, Phys. Rev. B **15**, 989 (1977).
5. H. L. Wang, F. H. Yang, S. L. Feng, *et al.*, Phys. Rev. B **61**, 5530 (2000).
6. N. P. Stepina, R. Beyer, A. I. Yakimov, *et al.*, Phys. Low-Dimens. Semicond. Struct. **11/12**, 261 (2001).
7. W.-H. Chang, W. Y. Chen, M. C. Cheng, *et al.*, Phys. Rev. B **64**, 125315 (2001).
8. P. N. Brunkov, S. G. Konnikov, V. M. Ustinov, *et al.*, Fiz. Tekh. Poluprovodn. (St. Petersburg) **30**, 924 (1996) [Semiconductors **30**, 492 (1996)].
9. P. N. Brounkov, A. Polimeni, S. T. Stoddart, *et al.*, Appl. Phys. Lett. **73**, 1092 (1998).
10. A. I. Yakimov, A. V. Dvurechenskii, A. I. Nikiforov, and O. P. Pchelyakov, Phys. Low-Dimens. Semicond. Struct. **3–4**, 99 (1999).
11. A. I. Yakimov, A. V. Dvurechenskii, Yu. Yu. Proskuryakov, *et al.*, Appl. Phys. Lett. **75**, 1413 (1999).
12. A. I. Yakimov, A. V. Dvurechenskii, V. V. Kirienko, *et al.*, Phys. Rev. B **61**, 10868 (2000).
13. A. I. Yakimov, A. V. Dvurechenskii, A. I. Nikiforov, and Yu. Yu. Proskuryakov, J. Appl. Phys. **89**, 5676 (2001).
14. A. V. Dvurechenskii, A. V. Nenashev, and A. I. Yakimov, Nanotechnology **13**, 75 (2002).
15. W. Meyer and H. Neldel, Z. Tech. Phys. (Leipzig) **12**, 588 (1937).
16. W. B. Jackson, Phys. Rev. B **38**, 3595 (1988).
17. W. E. Spear, D. Allan, P. Le Comber, and A. Ghaith, Philos. Mag. B **41**, 419 (1980).
18. M. Yamaguchi, J. Non-Cryst. Solids **77/78**, 535 (1985).
19. Y. Lubianiker and I. Balberg, Phys. Rev. Lett. **78**, 2433 (1997).
20. J. C. Wang and Y. F. Chen, Appl. Phys. Lett. **73**, 948 (1998).
21. K. L. Narasimhan and B. M. Arota, Solid State Commun. **55**, 615 (1985).
22. W. Rehm, R. Fischer, J. Stuke, and H. Wagner, Phys. Status Solidi B **78**, 539 (1977).
23. F. Djamdji and P. G. Le Comber, Philos. Mag. B **56**, 31 (1987).
24. R. S. Crandall, Phys. Rev. B **43**, 4057 (1991).
25. Y. F. Chen and S. F. Huang, Phys. Rev. B **44**, 13775 (1991).
26. A. Yelon and B. Movaghar, Phys. Rev. Lett. **65**, 618 (1990).
27. A. Yelon, B. Movaghar, and H. M. Branz, Phys. Rev. B **46**, 12 244 (1992).
28. G. Boisvert, L. J. Lewis, and A. Yelon, Phys. Rev. Lett. **75**, 469 (1995).

Translated by Yu. Sin'kov

JETP Letters, Vol. 80, No. 5, 2004, pp. 326–329. Translated from Pis'ma v Zhurnal Éksperimental'noĭ i Teoreticheskoĭ Fiziki, Vol. 80, No. 5, 2004, pp. 372–375.

Correlations in the Director-Orientation Fluctuations in the Presence of Microscopic Impurities in a Nematic Liquid Crystal

A. N. Vasilev[1, *], I. P. Pinkevich[1], and T. J. Sluckin[2]

[1]*Department of Theoretical Physics, Faculty of Physics, Shevchenko State University, Kiev, 03022 Ukraine*
**e-mail: vasilev@univ.kiev.ua*

[2]*School of Mathematics, University of Southampton, Southampton, SO17 1BJ, United Kingdom*

Received June 28, 2004; in final form, July 20, 2004

The model of a spatially restricted liquid-crystal system with microscopic impurities homogeneously distributed in the system is considered. The thermodynamic correlations of the director-orientation fluctuations and the correlations of the scalar order parameter characterizing impurities in the system are investigated for this system. It is shown that the impurity correlations are weaker than in a pure isotropic liquid. The correlations in the director deviations depend essentially on the wavevector and can be substantially weakened in the presence of impurities. © *2004 MAIK "Nauka/Interperiodica".*

PACS numbers: 31.15.Kb; 61.30.-v; 61.30.Cr

In spite of the tangible progress made in recent years in the study of liquid crystals, some problems still remain topical and incompletely resolved [1–3]. The problem of calculating the correlation of the fluctuations of orientational order in nematic crystals in the presence of impurities may be related to the aforementioned problems. Taken alone, this problem is rather many-sided, and its solution is essentially determined by the type of impurity particles, their nature, and by several other factors [4]. In this work, a model is suggested for studying the correlation behavior of the director fluctuations in a liquid-crystal spatially restricted system with the geometry of a plane-parallel layer in the presence of thermodynamically equilibrium impurities homogeneously distributed in the system. Note that such systems without impurities were rather successfully studied in a number of works (see, e.g., [5]). We will study the microscopic impurities that are suggested to be interpret as an isotropic liquid subsystem in the nematic matrix.

For definiteness, we will consider a nematic liquid layer of thickness L confined between two identical surfaces. The z axis is directed perpendicular to the layer plane, and the confining surfaces have the coordinates $z = 0$ and L. The deformation energy of liquid crystal is taken in the form

$$F_{lq} = \frac{1}{2}\int (K_1(\mathrm{div}\mathbf{n})^2 + K_2(\mathbf{n}\,\mathrm{curl}\,\mathbf{n})^2 + K_3(\mathbf{n}\times\mathrm{curl}\,\mathbf{n})^2)dV, \quad (1)$$

where K_i (i = 1–3) are the Frank moduli and $\mathbf{n}$ is the director unit vector that depends, in the general case, on the spatial coordinate. Integration is over the sample volume. We also assume that the anchoring at the wall surfaces is rigid, so that the director at the surface is directed perpendicular to the walls.

Apart from this energy that is caused, as was mentioned above, by the distortion of the director orientation, one should also take into account the energy of isotropic impurities and their direct interaction with liquid crystal. In particular, the subsystem of isotropic liquid is characterized by the Hamiltonian

$$F_{il} = \frac{1}{2}\int (a\phi^2 + b(\nabla\phi)^2)dV, \quad (2)$$

where $\phi(\mathbf{r})$ is the scalar order parameter (e.g., deviation of density from its mean value), and the parameters a and b are the standard parameters of the Landau theory.

The natural question arises as to how one should characterize the interaction of a nematic matrix with isotropic impurities. In the model adopted, this interaction is considered as a process of director orientation in the gradient field of the order parameter. The corresponding term should be invariant about the direction inversion. There can be several such terms. However, it can easily be shown that they all lead to essentially similar effects. For this reason, to obtain qualitative results, we consider only one energy term that describes the interaction of the nematic with the impurities:

$$F_{il} = -W\int (\nabla\cdot\mathbf{n})(\mathbf{n}\nabla\phi)dV. \quad (3)$$

In this case, the parameter W characterizes the interaction between the nematic and impurities, and it can be, strictly speaking, either positive or negative.

Therefore, we will consider below the following total energy of the system:

$$F = F_{lq} + F_{il} + F_{ll}. \quad (4)$$

It is quite obvious that the homogeneous director distribution along the direction perpendicular to the nematic layer is statistically equilibrium for this system.

Of interest to us are the thermodynamic director fluctuations in such a system. With this in mind, we consider, as is customary, the director deviation from the equilibrium value. We choose the vector $\delta\mathbf{n}(\mathbf{r}) = (\delta n_x(\mathbf{r}), \delta n_y(\mathbf{r}), 0)$ as a quantity characterizing the director deviation (the z axis is chosen perpendicular to the plane of nematic layer). Next, we consider the energy increment (to a second approximation in the director deviation) caused by the director fluctuations. In particular, taking into account the boundary conditions for the director and the condition following from the minimization of the total Hamiltonian with respect to the scalar order parameter (its derivative with respect to the coordinate z at the boundary is zero), we represent the director deviation and the order parameter in the form of series

$$\delta n_\alpha(\mathbf{r}) = \sum_{m=1}^{\infty} \delta n_{\alpha,(m)}(x, y)\sin(\pi m z/L), \quad (5)$$

$$\phi(\mathbf{r}) = \sum_{m=1}^{\infty} \phi_m(x, y)\cos(\pi m z/L), \quad (6)$$

where $\alpha = \{x, y\}$. We then perform the Fourier transform in the layer plane, according to the relation

$$f(\mathbf{r}) = \frac{1}{S}\sum_{\mathbf{q}} f(\mathbf{q})\exp(i\mathbf{q}\mathbf{r}), \quad (7)$$

with the vector $\mathbf{r}$ lying in the layer plane and S determining the layer area. As a result, one has, in a single-constant approximation ($K_1 = K_2 = K_3 \equiv K$),

$$\delta F = \frac{L}{4S}\sum_{m=1}^{\infty}\sum_{\mathbf{q}}\Big(K(q^2 + \pi^2 m^2/L^2)|\delta\mathbf{n}_{(m)}(q)|^2 + b(q^2 + \pi^2 m^2/L^2 + a/b)|\phi_m(q)|^2 + \frac{2iW\pi m}{L}\mathbf{q}\delta\mathbf{n}_{(m)}(q)\phi_m^*(q)\Big). \quad (8)$$

Next, it is convenient to introduce the parameter

$$\boldsymbol{\eta}_{(m)}(\mathbf{q}) = \delta\mathbf{n}_{(m)} + \frac{iW\pi m\mathbf{q}\phi_m^*(q)}{KL(q^2 + \pi^2 m^2/L^2)}. \quad (9)$$

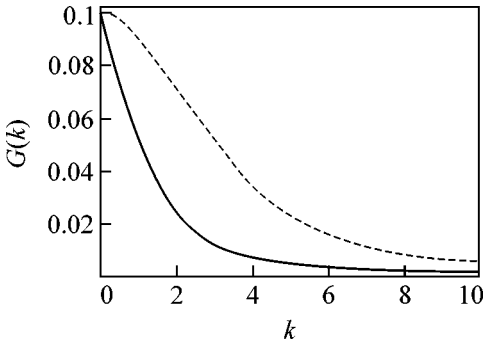

Statistical correlator $G(k) \sim \langle|\phi(k)|^2\rangle$ for (solid line) pure liquid and (dashes) in the presence of liquid crystal.

In this case, the free energy corresponding to an individual harmonic can be represented as

$$\delta F_{\mathbf{q},(m)} = \frac{L}{4S}\Big(K\Big(q^2 + \frac{\pi^2 m^2}{L^2}\Big)|\boldsymbol{\eta}_{(m)}(q)|^2 + b\Big(q^2 + \frac{\pi^2 m^2}{L^2} + a/b\Big) + \frac{W^2\pi^2 m^2 q^2}{KL^2(q^2 + \pi^2 m^2/L^2)}\Big)|\phi_m(q)|^2\Big). \quad (10)$$

Using this expression and the theorem on the energy equipartition among the degrees of freedom, one obtains the statistical mean for the order parameter fluctuations:

$$\langle|\phi_m(q)|^2\rangle = \frac{2k_B TS/L}{b(q^2 + \pi^2 m^2/L^2 + a/b) + \dfrac{W^2\pi^2 m^2 q^2}{KL^2(q^2 + \pi^2 m^2/L^2)}}. \quad (11)$$

One can readily see that the new features arise, as compared to a pure liquid.

To study the director correlations, it is reasonable to represent the director via the projections onto the layer plane in such a way that, say, the x axis coincides with the direction of the $\mathbf{q}$ vector (clearly, this representation is unique for each wavevector). Then, instead of the parameter $\boldsymbol{\eta}$, it is more suitable to introduce another (scalar) parameter, namely,

$$\nu_m(\mathbf{q}) = \phi_m(q) - \frac{iW\pi m q n_x^*(q)}{bL(q^2 + \pi^2 m^2/L^2 + q/b)}. \quad (12)$$

One can easily see that the correlators for different projections of the vector of director deviations are different. Namely, one has for energy

$$\delta F_{\mathbf{q},(m)} = \frac{L}{4S}\Big(\sum_{\alpha = x, y}\Big(K\Big(q^2 + \frac{\pi^2 m^2}{L^2}\Big)|\delta n_{\alpha,(m)}(q)|^2$$

$$+\frac{W^2\pi^2m^2q^2|\delta n_{\alpha,(m)}(q)|^2\delta_{\alpha,x}}{bL^2(q^2+\pi^2m^2/L^2+a/b)}\Bigg) \quad (13)$$

$$+b\left(q^2+\frac{\pi^2m^2}{L^2}+a/b\right)|\nu_m(q)|^2\Bigg).$$

In this expression, $\delta_{\alpha,\beta}$ is the Kronecker delta. It is then clear that no changes, as compared to a pure nematic, occur in the statistical correlations in the direction perpendicular to the wavevector **q**. In particular, one has in this case

$$\langle|n_{y,(m)}(q)|^2\rangle = \frac{2k_BTS}{KL(q^2+\pi^2m^2/L^2)}. \quad (14)$$

The correlations appreciably weaken along the wavevector direction. For the corresponding vector component, one has

$$\langle|n_{x,(m)}(q)|^2\rangle = \frac{2k_BTS/L}{K(q^2+\pi^2m^2/L^2)+\dfrac{W^2\pi^2m^2q^2}{bL^2(q^2+\pi^2m^2/L^2+a/b)}}. \quad (15)$$

Clearly, the dependence in the latter case is qualitatively the same as for the order parameter correlations of isotropic impurities.

Thus, when comparing the fluctuations of scalar order parameters in the system of interest with those in a pure liquid, one arrives at the conclusion that the presence of a nematic has a stabilizing effect on the fluctuation correlations. At the same time, impurities exert the same effect on the correlations of director orientation. However, in the latter case, this effect shows up only in the fluctuation wavevector direction. Considering that the Fourier transforms of the correlation functions determine the light-scattering intensity, and that the intensity of this scattering from the director fluctuations is an order of magnitude higher than for the light scattering from the density fluctuations, this result is of interest from the viewpoint of the experiments with light scattering in these systems.

In addition, one can see from Eq. (15) that the last term in the denominator is constant for the isotropic component of the system (i.e., impurity liquid) at the critical point defined by $a/b + \pi^2/L^2 = 0$ (this is a critical point of a restricted system; for the unrestricted system, this condition takes the form $a = 0$), for which reason one can speak about a change in the fluctuation correlation radius in the direction determined by the wavevector **q**.

From a practical point of view, of prime interest are the values of statistical correlators in the "laboratory" system. It is evident that these correlators are expressed in terms of a linear combination of the statistical correlators obtained above. One can thus expect that, when conducting an experiment (e.g., on light scattering by the system under consideration), some difficulties of a fundamental nature can arise, because, in this case, one would have to offset an addition that is small compared to the contribution introduced to the scattering intensity directly from the liquid-crystal subsystem. It may well be that this is precisely the reason why such measurements have not been carried out so far. Based on the data of this work, one can expect that the scattering peak in this case would be appreciably broader than in a pure substance.

Nevertheless, the relative simplicity of the suggested model allows its physical interpretation to be somewhat extended. For instance, it can evidently be applied at least to a partial description of the two-phase region of a nematic–isotropic liquid system. Here, a qualitative correlation is seen between the model results and the data (theoretical and experimental) obtained for such (and related) systems [4, 6]. In addition, of interest is an isotropic system with a relatively low concentration of strongly anisotropic molecules. In this case, one can deal with a binary solution or a liquid with impurities. The shift of critical parameters (temperature) as a function of the concentration (or other characteristics of the interaction between the subsystems) and the linear sizes (in the case of spatial confinement) is ordinarily the main effect to be studied [7]. With the correction for the critical indices, our results agree well with the data on both liquid-crystal [5, 7] and liquid (one-component and binary) [7–9] systems. Finally, the character of the correlation behavior of the system is in qualitative agreement with the Monte Carlo results obtained for a liquid-crystal system with impurities (concerning the critical-point shift) [10]. Although the impurities in that work were regarded as frozen-in, qualitative agreement should occur, because, considering the zero mean-statistical value of the order parameter of an isotropic subsystem and the random character of its fluctuations, the latter can be interpreted, with some reservations, as an external random field. At the same time, the models with such fields often serve as a base for studying the behavior of liquid systems in porous media (see, e.g., [11] and references therein). In this respect, the suggested model is not contradictory to the presently available data.

In spite of the aforementioned, the problem of the correlation behavior of the director fluctuations in a nematic liquid crystal with impurities calls for further investigation. In this respect, the refinement of the model by introducing the dependence of the Frank moduli on the mixture composition, as well as the inclusion of various types of interactions between the subsystems in the model, seems to be most promising. Nevertheless, the performance of an adequate experiment is likely the most complicated problem, because the majority of the aforementioned experimental works allow the practicability of the model to be checked only indirectly.

A.N.V. is grateful to the University of Southampton for hospitality and to the Royal Society, UK, for support.

REFERENCES

1. P. G. de Gennes and J. Prost, *The Physics of Liquid Crystals*, 2nd ed. (Mir, Moscow, 1982; Clarendon, Oxford, 1993).
2. A. Yu. Val'kov, V. P. Romanov, and A. N. Shalaginov, Usp. Fiz. Nauk **164**, 149 (1994) [Phys. Usp. **37**, 139 (1994)].
3. S. Singh, Phys. Rep. **324**, 107 (2000).
4. P. K. Mukherjee, Liq. Cryst. **22**, 239 (1997).
5. A. Yu. Val'kov, V. P. Romanov, and M. V. Romanov, Zh. Éksp. Teor. Fiz. **120**, 389 (2001) [JETP **93**, 344 (2001)].
6. P. K. Mukherjee, J. Chem. Phys. **116**, 9531 (2002).
7. M. A. Anisimov, *Critical Phenomena in Liquids and Liquid Crystals* (Nauka, Moscow, 1987) [in Russian].
8. N. B. Wilding, J. Phys.: Condens. Matter **9**, 585 (1997).
9. H. J. Singh, Chem. Eng. Data **45**, 131 (2000).
10. J. Ilnytskyi and S. Sokolowski, Phys. Rev. E **59**, 4161 (1999).
11. V. P. Voronov and V. M. Buleĭko, Zh. Éksp. Teor. Fiz. **113**, 1071 (1998) [JETP **86**, 586 (1998)].

Translated by V. Sakun

JETP Letters, Vol. 80, No. 5, 2004, pp. 330–334. From Pis'ma v Zhurnal Éksperimental'noĭ i Teoreticheskoĭ Fiziki, Vol. 80, No. 5, 2004, pp. 376–380.

On Electron Transport in ZrB_{12}, ZrB_2, and MgB_2 in Normal State¶

V. A. Gasparov[1, *], M. P. Kulakov[1], N. S. Sidorov[1], I. I. Zver'kova[1], V. B. Filipov[2], A. B. Lyashenko[2], and Yu. B. Paderno[2]

[1] *Institute of Solid State Physics, Russian Academy of Sciences, Chernogolovka, Moscow region, 142432 Russia*
** e-mail: vgasparo@issp.ac.ru*
[2] *Institute for Problems of Material Science, National Academy of Sciences of Ukraine, Kiev, Ukraine*
Received July 20, 2004

We report on measurements of the temperature dependence of resistivity, $\rho(T)$, for single-crystal samples of ZrB_{12}, ZrB_2, and polycrystalline samples of MgB_2. It is shown that the cluster compound ZrB_{12} behaves as a simple metal in the normal state, with a typical Bloch–Grüneisen $\rho(T)$ dependence. However, the resistive Debye temperature, $T_R = 300$ K, is three times smaller than T_D obtained from specific heat data. We observe the T^2 term in $\rho(T)$ of all these borides, which could be interpreted as an indication of strong electron–electron interaction. © *2004 MAIK "Nauka/Interperiodica".*

PACS numbers: 72.15.Gd; 74.60.Ec; 74.70.Ad

It is known that boron has a tendency to form cluster compounds. In particular, there are octahedral B_6 clusters in MeB_6, icosahedral B_{12} clusters in β-rhombohedral boron, and cuboctahedral B_{12} clusters in MeB_{12}. So far, several superconducting cubic hexa- (MeB_6) and dodecaborides (MeB_{12}) have been discovered [1] (*Me* = Sc, Y, Zr, La, Lu, Th). Many other cluster borides (*Me* = Ce, Pr, Nd, Eu, Gd, Tb, Dy, Ho, Er, Tm) were found to be ferromagnetic or antiferromagnetic [1, 2]. Even though the superconductivity in ZrB_{12} was discovered a long time ago ($T_c = 6$ K) [1], there has been little effort devoted to the study of electron transport and basic superconductive properties of dodecaborides. Only recently, electron transport of solid solutions $Zr_{1-x}Sc_xB_{12}$ [3] as well as the band structure calculations of ZrB_{12} [4] has been reported. Understanding the properties of cluster borides as well as the superconductivity mechanism in these compounds is very important.

In this letter, we address this problem. We present the results from measurement of the temperature dependences of resistivity, $\rho(T)$, for single crystals of ZrB_{12}. Comparative data from single crystals of ZrB_2 and polycrystalline samples of MgB_2 are also presented. The superconducting properties of ZrB_{12} will be published elsewhere.

Under ambient conditions, dodecaboride ZrB_{12} crystallizes in the fcc structure of the UB_{12} type (space group $Fm3m$), $a = 0.7408$ nm [5]. In this structure, the Zr atoms are located at interstitial openings in the close-packed B_{12} clusters [3]. In contrast, ZrB_2 shows a phase consisting of two-dimensional graphitelike monolayers of boron atoms with a honeycomb lattice structure, intercalated with Zr monolayers (with lattice parameters $a = 0.30815$ nm and $c = 0.35191$ nm [6]).

The ZrB_2 powder was produced by the boron carbide reduction of ZrO_2. The ZrB_{12} single crystals were obtained from a mixture of a certain amount of ZrB_2 and an excess of boron (50–95%). The resulting materials were subjected to a crucible-free RF-heated zone-induction melting process in an argon atmosphere. The obtained single-crystal ingots of ZrB_{12} and ZrB_2 have a typical diameter of about 5–6 mm and a length of 40 mm. A metallographic investigation detected that the ZrB_2 crystal is surrounded by a polycrystalline rim about 0.5 mm thick. The measured specific density of the ZrB_{12} rod is 3.60 g/cm^3, in good agreement with the theoretical density. The X-ray diffraction measurements confirmed that both ingots are single crystal. We found the cell parameters of ZrB_{12}, $a = 0.74072 \pm 0.00005$ nm, to be very close to the published values [5].

Polycrystalline MgB_2 and $CaMgB_2$ samples were sintered from metallic Mg or a mixture of Ca, Mg powders and boron pellets using a similar technique as was outlined in our earlier work [6]. This technique is based on the reactive liquid Mg, Ca infiltration of boron. X-ray diffraction patterns and optical investigation show large grains of single MgB_2 phase, with much smaller grains of semiconducting CaB_6 phase visible in-between. The density of MgB_2 grains was rather high, 2.4 g/cm^3, while the samples prepared from Mg infiltration had a smaller density of 2.2 g/cm^3. Only MgB_2

¶ This article was submitted by the authors in English.

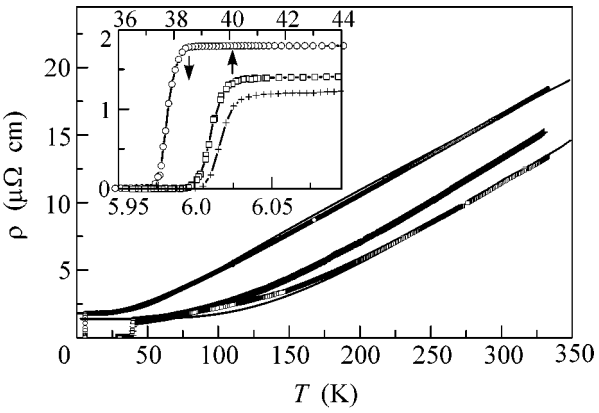

Fig. 1. Temperature dependence of the resistivity, ρ(*T*), of ZrB_{12} single-crystal (open circles), MgB_2 (squares), and $CaMgB_2$ (crosses) samples. The solid lines represent BG fits to the experimental data by Eq. (1).

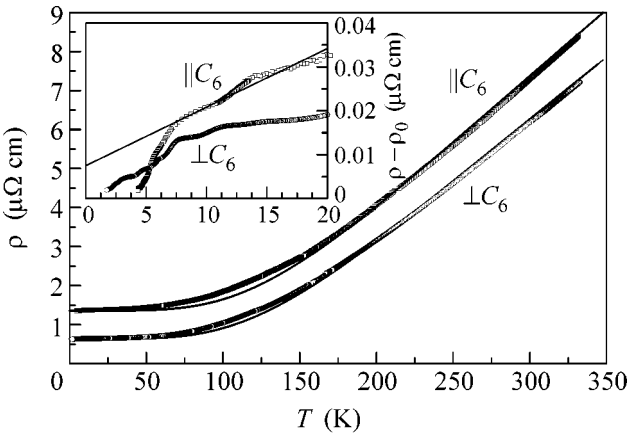

Fig. 2. Temperature dependence of ρ(*T*) of ZrB_2 single-crystal samples in basal plane (circles) and in the *c* direction (squares).

samples cut from large grains were studied. These samples will be denoted as $CaMgB_2$.

We used a spark erosion method to cut the samples into a parallelepiped with dimensions of about $0.5 \times 0.5 \times 8$ mm. Single-crystal samples were oriented along ⟨100⟩ for ZrB_{12} and in hexagonal [0001] and basal $[1\bar{1}00]$ directions for ZrB_2, respectively. The orientation process was performed using an X-ray Laue camera. The samples were lapped by diamond paste and subsequently etched: ZrB_{12} in hot nitrogen acid, ZrB_2 in mixture of $H_2O_2/HNO_3/HF$, and MgB_2 in 2% HCl plus water-free ethanol.

A standard four-probe ac (9 Hz) method was used for resistance measurements. We used Epotek H20E silver epoxy for the electrical contacts. The samples were mounted in a temperature variable liquid helium cryostat. Temperature was measured with platinum (PT-103) and carbon glass (CGR-1-500) sensors. The critical temperature measured by RF susceptibility [6] and ρ(*T*) was found to be $T_{c0} = 5.97$ K for ZrB_{12} samples and 39 K for MgB_2 polycrystalline samples, respectively.

We display the temperature dependence of the resistivity for ZrB_{12}, MgB_2, and $CaMgB_2$ in Fig. 1 and that of ZrB_2 in Fig. 2. To emphasize the variation of ρ(*T*) in a superconductive state, we plot these data in the inset of Fig. 1. The samples demonstrate a remarkably narrow superconducting transition with $\Delta T = 0.04$ K for ZrB_{12} and with $\Delta T = 0.7$ K for both MgB_2 samples. Such a transition is a characteristic of good quality samples.

Recently, we reported superconductivity at 5.5 K in the polycrystalline samples of ZrB_2 [6]. This was not confirmed in later studies [7]. As we can see from Fig. 2, no superconductivity was observed in single-crystal samples of ZrB_2 down to 1.3 K, while a pronounced slope change in ρ(*T*) is observed around 7 K. Such behavior could be associated with nonstoichiometry in the zirconium sublattice [8]. In ZrB_2, the Fermi level is located in the pseudogap. The presence of Zr defects in $Zr_{0.75}B_2$ leads to the appearance of a very intense peak in the density of states in the vicinity of the pseudogap and subsequent superconductivity [8]. We strongly believe that the observation of [6] was due to the nonstoichiometry of our samples. Superconductivity in nonstoichiometric samples is very common in other borides: $MoB_{2.5}$, $NbB_{2.5}$, Mo_2B, W_2B, and $BeB_{2.75}$ [9, 10].

It is worth noting that ZrB_{12} is mostly boron, and one could speculate that its resistivity should be rather high. In contrast, we observe that the room-temperature resistivity of ZrB_{12} is almost the same as for MgB_2 and ZrB_2 samples. The ρ(*T*) is linear above 90 K with the slope of ρ(*T*) more pronounced than in MgB_2 or ZrB_2. The residual resistivity ratio RRR of 9.3 for ZrB_{12} as well as RRR ≈ 10 for MgB_2 and ZrB_2 samples suggests that the samples are in the clean limit. One can predict a nearly isotropic resistivity for fcc ZrB_{12}, which can be described by the Bloch–Grüneisen (BG) expression of the electron–phonon *e–p* scattering rate [11]:

$$\rho(t) - \rho(0) = 4\rho_1 t^5 \int_0^{1/t} \frac{x^5 e^x dx}{(e^x - 1)^2} = 4\rho_1 t^5 J_5(1/t). \quad (1)$$

Here, ρ(0) is the residual resistivity, $\rho_1 = d\rho(T)/dT$ is the slope of ρ(*T*) at high T ($T > T_R$), $t = T/T_R$, T_R is the resistive Debye temperature, and $J_5(1/t)$ is the Debye integral. As we can see from Fig. 1, all data for ZrB_{12} fall very close to the theoretical BG function (solid line). To emphasize the variation of ρ(*T*) at low *T*, we plot these data as $\rho(T) - \rho(0)$ versus $t^5 J_5(1/t)$ in Fig. 3 on a log–log scale. The BG formula predicts a linear dependence of $\log[\rho(T) - \rho(0)]$ versus $\log[t^5 J_5(1/t)]$ with the slope

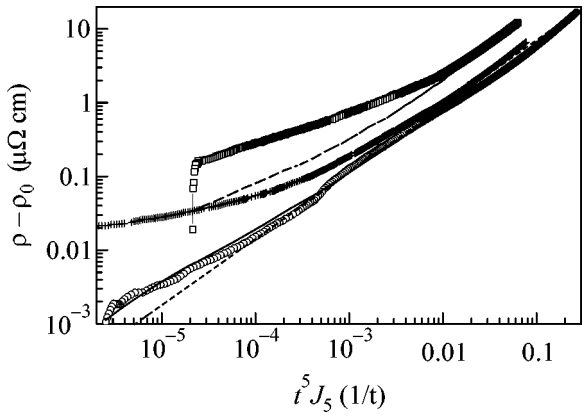

Fig. 3. The $\rho(T) - \rho(0)$ vs. reduced Debye integral $t^5J_5(1/t)$ for ZrB_{12} (open circles), ZrB_2 in the basal plane (crosses), and $CaMgB_2$ (squares). The dashed line is $\rho(T)$ of MgB_2 calculated in the two-band model [12].

equal to unity. We use T_R as a fitting parameter to achieve agreement at high temperatures. For comparison, we also present our $\rho(T)$ data of ZrB_2 and MgB_2 calculated in a clean case of the two-band model [12].

It is clear from Fig. 3 that, above 25 K, the BG model describes the $\rho(T)$ dependence of ZrB_{12} fairly well. It is remarkable that this description works well with constant T_R = 300 K. At the same time, T_D calculated from specific heat data [13] is three times higher. Furthermore, T_D increases from 800 to 1200 K as temperature varies from T_c up to room temperature. In order to shed light on this discrepancy, we used a model applied to LaB_6 of [14]. We can treat the boron sublattice as a Debye solid with T_R and the Zr ions as independent Einstein oscillators with characteristic temperature T_E. The effect of the Einstein mode on the resistivity of a metallic solid is discussed in [15]:

$$\rho_E(T) = \frac{KNe^{T_E/T}}{MT(e^{T_E/T} - 1)^2}. \quad (2)$$

Here, N is the number of oscillators per unit volume, K is a constant that depends on the electron density of the metal, and M is the atomic mass. We fit the data by summing Eqs. (1) and (2) and living KN/M, ρ_1, T_R as free parameters. Although the model calculations perfectly match the data (see solid line in Fig. 3), the T_E we obtain is unreasonably small (T_E = 50 K) and the difference between T_R and specific heat T_D becomes even worse, T_R = 270 K. We believe that this inconsistency of T_R and T_D can be explained by limitation of T_R by a cutoff phonon wave vector $q = k_BT/\hbar s$. The latter is limited by the Fermi surface (FS) diameter $2k_F$ [16] rather than the highest phonon frequency in the phonon spectrum.

According to band structure calculations [4], the FS of ZrB_{12} consists of an open sheet along the ΓL direction at point Γ with $k_{\Gamma X}$ = 0.47 Å^{-1}, a quasispherical sheet at point X ($k_{X\Gamma}$ = 0.37 Å^{-1}), and a small sheet at point K ($k_{K\Gamma}$ = 0.14 Å^{-1}). We suggest that T_R is limited by the small FS sheet. Unfortunately, the experimental FS model and the sound velocity are not yet known. Therefore, we cannot corroborate this suggestion by experimental FS.

As we can see from Fig. 3, the $\rho(T)$ of ZrB_2 and MgB_2 samples deviates from the BG model even more dramatically. Putti *et al.* [17] modified the BG equation, introducing variable power n for the $t^nJ_n(1/t)$ term in Eq. (1). The best fit to the data was obtained with n = 3, which, in fact, ignores the small-angle e–p scattering. Recently, Sologubenko *et al.* [18] reported a cubic T dependence in a, b plane resistivity below 130 K in the single crystals of MgB_2. This was attributed to the interband e–p scattering in transition metals.

However, we believe that there are strong objections to this modified BG model: (i) a cubic $\rho(T)$ dependence is a theoretical model for large-angle e–p scattering, and no evidence of it was observed in transition and nontransition metals; (ii) the numerous studies of the $\rho(T)$ dependence in transition metals have found it to be consistent with a sum of electron–electron e–e, T^2, and e–p, T^5, contributions to the low-T resistivity, which may easily be confused with a T^3 law [11, 19, 20]; and (iii) the interband σ–π e–p scattering plays no role in normal transport in the two-band model for MgB_2 [12].

In order to solve these problems, we added an e–e scattering T^2 term in Eq. (1) [19, 20] as a possible scenario. Indeed, keeping in mind that the BG term is proportional to T^5 at $T < 0.1T_R$, the $\rho(T)$ dependence may be presented in a simple way [19, 20]: $[\rho(T) - \rho(0)]/T^2 = \alpha + \beta T^3$. Here, α and $\beta = 497.6\rho_1/T_R^5$ are parameters of e–e and e–p scattering terms, respectively. Such a plot should yield a straight line with a slope of β, and its intercept with y-axis (T = 0) should be equal to α. Further, to be consistent with the BG law, the β parameter should lead to the same T_D as obtained from high-T log–log fit in Fig. 3, and both coefficients must be independent of $\rho(0)$. We determined $\rho(0)$ from the intercept of linear $\rho(T)$ versus T^2 dependence with the T = 0 axis and plotted the $[\rho(T) - \rho(0)]/T^2$ versus T^3 in Fig. 4. It is evident that the measured resistivity approaches a quadratic law at $T < 25$ K in ZrB_{12}, at $T < 100$ K in ZrB_2, and at $T < 150$ K in both MgB_2 samples.

The regime of applicability of a two-term fit is limited to temperatures below $0.1T_R$. At larger T, the e–p term increases more slowly than T^5 law, and this is why the data are no longer consistent with the two-term equation. From the intercept with T = 0 axis, we find very similar values of α for ZrB_{12} and ZrB_2 samples in the basal plane (α = 22 and 15 pΩ cm K^{-2}, respec-

tively), while α is about five times larger for the $CaMgB_2$ sample, 95 pΩ cm K^{-2}. The slopes of β give ρ_1 and T_R values largely consistent with high-temperature log–log fits for the ZrB_{12} and ZrB_2 samples.

However, low-T results for β and ρ_1 are far from consistent with high-T data for both MgB_2 and $CaMgB_2$ samples. Nevertheless, the magnitude of $T_R = 900$ K for MgB_2 extracted from log–log fit above 150 K is in excellent agreement with $T_D = 920$ K obtained from low-temperature specific heat measurements [21] and is considerably lower than the reported data based on T^3 dependence of $\rho(T)$ ($T_R = 1050$–1226 K, where the T^2 term was ignored) [7, 17, 18]. A similar fit for the theoretical curve is even more consistent with $T_R = 900$ K; however, we have to mention that violation of Matthiessen's rule in MgB_2 may mask the intrinsic $\rho(T)$ dependence [12].

In general, there are many scattering processes responsible for the T^2 term in $\rho(T)$ of metals: (i) size-, surface-, dislocation-, and impurity scattering-induced deviations from Matthiessen's rule (see references in [22]), (ii) *e–p* scattering for small cylindrical FS sheets relative to the phonon wave vector [16], (iii) inelastic electron impurity scattering (*e–i*) [23], (iv) the quantum interference between *e–i* and *e–p* scattering [24], and (v) *e–e* scattering [19, 20].

We can estimate some of these effects. We use the Drude law to obtain the residual electron mean free path $l = 4\pi v_F/\rho\omega_p^2$. Using a Fermi velocity of $v_\sigma = 3.2 \times 10^7$ cm/s and a plasma frequency $\omega_p^\sigma = 5.16 \times 10^{15}$ s^{-1} for MgB_2 σ-band [12], we obtain $l \approx 100$ nm. This implies that size effects are negligible for both MgB_2 samples and Zr borides. In agreement with ZrB_2 data (see Fig. 4), the α is proportional to $\rho(0)$ for inelastic *e–i* scattering [23, 24]. However, this term is 1.5 times lower for $CaMgB_2$ relative to MgB_2, which has the same $\rho(0)$.

We can try to estimate the contribution from the small FS sheets to α. The T^2 term was observed in $\rho(T)$ and electron scattering rates of Bi and Sb, which was attributed to a lack of one q component for *e–p* scattering on small cylindrical FS sheets [16]. The FS of MgB_2 is composed of two warped open cylinders running along the c axis that arise from σ boron orbitals [12, 25]. The FS of ZrB_2 consists of nearly ellipsoidal surfaces joined together at the corners [26, 27], which may also be responsible for the T^2 term in $\rho(T)$. We can use the sound velocity $s = 1.1 \times 10^6$ and 8×10^5 cm/s for MgB_2 and ZrB_2, respectively [28, 29], to estimate the lowest temperature, $T_{min} = \hbar k_F s/k_B$, when the phonon wave vector **q** matches the neck of a smaller σ tube in MgB_2 ($k_\sigma = 0.129$ Å^{-1} [25]) or the diameter of the ellipsoidal sheets in ZrB_2 ($k_F = 0.095$ Å^{-1} [26]). We obtain $T_{min} = 95$ and 60 K, respectively. Thus, we conclude

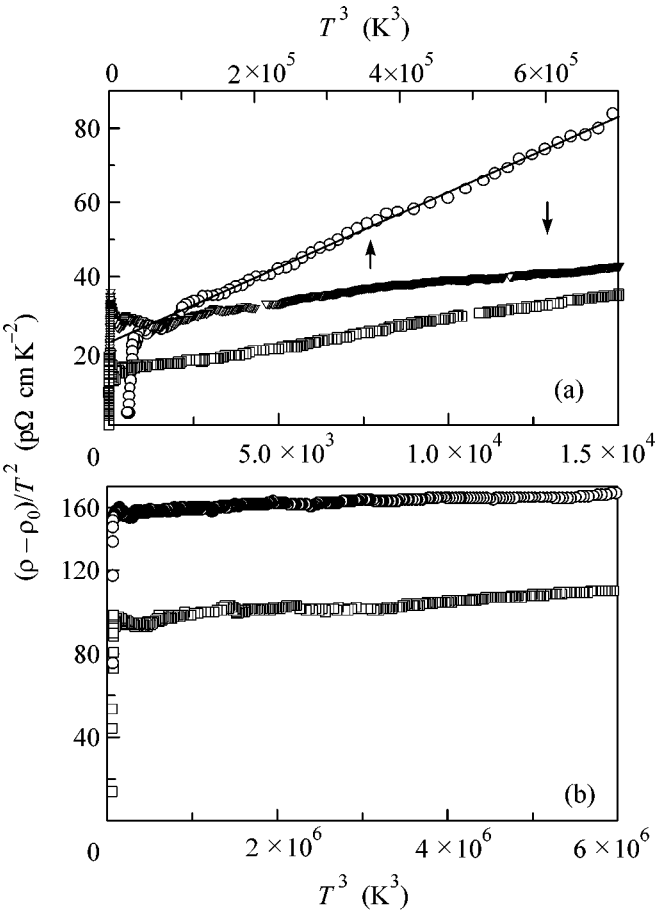

Fig. 4. Low-temperature behavior of $[\rho(T) - \rho(0)]/T^2$ versus T^3 for (a) ZrB_{12} (circles), ZrB_2 in the basal plane (squares), ZrB_2 along c (triangles) and (b) MgB_2 (circles) and $CaMgB_2$ (squares) samples.

that $q < k_F$ at $T < 100$ K in both diborides, which implies that the contribution of 2D FS sheets to α is negligible.

In general, only umklapp *e–e* scattering contributes to $\rho(T)$, whereas normal collisions are significant in compensated medals and in thermal resistivity [20]. Borides have rather high T_D, which depresses the *e–p* scattering, so that the *e–e* SR term is easier to observe. Notice, however, that the α value for MgB_2 is five times larger than the corresponding values in ZrB_{12} and ZrB_2. The latter values are, in turn, five times larger than in transition metals ($\alpha_{Mo} = 2.5$ pΩ cm K^{-2} and $\alpha_W = 1.5$–4 pΩ cm K^{-2} [19, 20]). Therefore, additional experiments must be performed for more pure samples before final conclusion about the origin of the T^2 term in borides can be drawn.

In conclusion, we present a study of the $\rho(T)$ of single crystals of ZrB_{12}, ZrB_2, and polycrystalline samples of MgB_2. Large differences between resistive and specific heat Debye temperatures have been observed for ZrB_{12}. The results provide evidence of a T^2 term for all

these borides at low T, the origin of which is not yet understood.

The very useful discussions with V.F. Gantmakher, A. Junod, I. Shein, and R. Huguenin, and help in preparation of the paper by L.V. Gasparov are gratefully acknowledged. This work was supported by the Russian scientific programs "Superconductivity of Mesoscopic and Highly Correlated Systems" (Volna 4G), "Synthesis of Fullerenes and Other Atomic Clusters" (grant no. 541-028), and "Surface Atomic Structures" (grant no. 4.10.99); by the Russian Ministry of Industry, Science, and Technology (grant no. MSh-2169.2003.2); by the Russian Foundation for Basic Research (grant no. 02-02-16874a); and by INTAS (grant no. 01-0617).

REFERENCES

1. B. T. Matthias, T. H. Geballe, K. Andres, *et al.*, Science **159**, 530 (1968).
2. Yu. B. Paderno, N. Shitsevalova, I. Batko, *et al.*, J. Alloys Compd. **219**, 215 (1995).
3. K. Hamada, M. Wakata, N. Sugii, *et al.*, Phys. Rev. B **48**, 6892 (1993).
4. I. R. Shein and A. L. Ivanovskii, Fiz. Tverd. Tela (St. Petersburg) **45**, 1363 (2003) [Phys. Solid State **45**, 1429 (2003)].
5. A. Leithe-Jasper, A. Sato, T. Tanaka, *et al.*, Z. Kristallogr. New Cryst. Struct. **217**, 319 (2002).
6. V. A. Gasparov, N. S. Sidorov, I. L. Zver'kova, and M. P. Kulakov, JETP Lett. **73**, 532 (2001).
7. B. Fisher, K. B. Chashka, L. Patlagan, *et al.*, Physica C (Amsterdam) **384**, 1 (2003).
8. I. R. Shein, N. I. Medvedeva, and A. L. Ivanovskiĭ, Fiz. Tverd. Tela (St. Petersburg) **45**, 1541 (2003) [Phys. Solid State **45**, 1617 (2003)].
9. Z. Fisk, AIP Conf. Proc. **231** (1991).
10. A. Yamamoto, C. Takao, T. Masui, *et al.*, Physica C (Amsterdam) **383**, 197 (2002).
11. J. M. Ziman, *Electrons and Phonons, Theory of Transport Phenomena in Solids* (Oxford Univ. Press, Oxford, 1960; Inostrannaya Literatura, Moscow, 1962).
12. I. I. Mazin, O. K. Andersen, O. Jepsen, *et al.*, Phys. Rev. Lett. **89**, 107002 (2002).
13. A. Junod *et al.* (2004) (in press).
14. D. Mandrus, B. C. Sales, and R. Jin, Phys. Rev. B **64**, 012302 (2001).
15. J. R. Cooper, Phys. Rev. B **9**, 2778 (1974).
16. V. F. Gantmakher, Rep. Prog. Phys. **37**, 317 (1974).
17. M. Putti, E. Galleani, D. Marr'e, *et al.*, Eur. Phys. J. B **25**, 439 (2002).
18. A. V. Sologubenko, J. Jun, S. M. Kazakov, *et al.*, Phys. Rev. B **66**, 014504 (2002).
19. N. V. Vol'kenshtein, V. P. Dyakina, and V. E. Startsev, Phys. Status Solidi **57**, 9 (1973).
20. V. A. Gasparov and R. Huguenin, Adv. Phys. **42**, 393 (1993).
21. A. Junod, Y. Wang, F. Bouquet, *et al.*, in *Studies of High Temperature Superconductors*, Ed. by A. Narlikar (Nova Science, Commack, N.Y., 2002), Vol. 38, p. 179.
22. J. van der Maas and R. Huguenin, J. Phys.: Condens. Matter **2**, 8137 (1990).
23. Yu. Kagan and A. P. Zhernov, Zh. Éksp. Teor. Fiz. **50**, 1107 (1966) [Sov. Phys. JETP **23**, 737 (1966)].
24. M. Yu. Reizer and A. V. Sergeev, Zh. Éksp. Teor. Fiz. **92**, 2291 (1987) [Sov. Phys. JETP **65**, 1291 (1987)].
25. A. Carrington, P. J. Meeson, J. R. Cooper, *et al.*, Phys. Rev. Lett. **91**, 037003 (2003).
26. T. Tanaka, Y. Ishizawa, E. Bannai, *et al.*, Solid State Commun. **26**, 879 (1978).
27. H. Rosner, J. M. An, W. E. Pickett, *et al.*, Phys. Rev. B **66**, 24521 (2002).
28. A. Shukla, M. Calandra, M. d'Astuto, *et al.*, Phys. Rev. Lett. **90**, 095506 (2003).
29. T. Aizawa, W. Hayami, and S. Otani, Phys. Rev. B **65**, 024303 (2001).

JETP Letters, Vol. 80, No. 5, 2004, pp. 335–338. Translated from Pis'ma v Zhurnal Éksperimental'noĭ i Teoreticheskoĭ Fiziki, Vol. 80, No. 5, 2004, pp. 381–384.

Resonance States of Gallium Impurity in Uniaxially Compressed Germanium

Ya. E. Pokrovskiĭ* and N. A. Khval'kovskiĭ

Institute of Radio Engineering and Electronics, Russian Academy of Sciences, Moscow, 125009 Russia

**e-mail: yaep@mail.cplire.ru*

Received July 20, 2004

To identify optical transitions that can excite long-wavelength stimulated radiation in uniaxially compressed Ga-doped germanium, the absorption and photoconduction spectra of this material were studied over a wide range of pressures in the [111] and [001] directions. It was found that some of the excited states of gallium impurity became resonant upon the buildup of pressure. The energy levels of these states reach the light-hole band, whereupon they enter this band and remain near its edge, showing up in the form of broad bands. No singularities confirming the existence of the impurity resonance states were observed in the spectra near the edge of the heavy-hole band. © *2004 MAIK "Nauka/Interperiodica".*

PACS numbers: 71.55.Cn

In [1], long-wavelength stimulated radiation was observed from gallium-doped germanium crystals ($N \approx 10^{14}$ cm^{-3}) prepared in the form of total internal-reflection cavities. The radiation appeared at low temperatures (4.2 K) in a strong (2–4 kV/cm) electric field upon crystal uniaxial compression with a pressure P of 4–10 kbar. It was assumed [2] that this effect is associated with the population of the impurity energy levels, split due to the crystal deformation and located in the light-hole band by hot holes. Calculations [3–5] confirmed that such resonance states could lie near the heavy-hole band edge. The subsequent interpretation [6–8] of the experimental results was based on the assumption that the acceptor spectra in uniaxially compressed Ge crystals are characterized by the local levels in the forbidden gap and resonance levels "attached" to the heavy-hole band edge. However, we are not aware of direct experiments confirming such an interpretation.

Similar states are known in silicon, whose absorption [9] and photoconductivity (PC) spectra have peaks corresponding to the transitions from the ground state $1S_{3/2}$ of group III acceptors to the $2P_{1/2}$ and $3P_{1/2}$ states in the valence-band branch split off by the spin–orbit interaction. These peaks are shifted to high energies from the narrow lines of the fundamental $P_{3/2}$ series by an energy close to the spin–orbit splitting (44 meV) and are broadened (≈0.5 meV) due to a short lifetime. However, Raman scattering studies [10] have proved that the $1S_{1/2}$ level of boron impurity is not a resonance level and lies in the forbidden gap at a distance of 23 meV from the valence-band edge. The subsequent calculations [11] gave a close position of this level. Our analysis of the impurity absorption and PC of uniaxially compressed Ga-doped germanium showed that the resonance states of this impurity really exist, but that their spectrum differs fundamentally from the one predicted in [3–5].

We studied Ga-doped germanium samples ($N \approx 10^{14}$ cm^{-3}) $1 \times 1 \times 10$ or $2 \times 2 \times 10$ mm in size, which were cut in the [111] and [001] directions. GaInSn alloy contacts (liquid state at room temperature) were applied to the ends of the samples. Excessive alloy was squeezed from under the contacts upon the compression of the samples between electrodes made of annealed copper. The PC noise in the samples with such contacts was determined by the background fluctuations at room temperature. To study the absorption and to normalize the PC spectra, a germanium photoresistor doped with Sb ($N \approx 10^{15}$ cm^{-3}) was located behind the sample. The photodetector aperture was limited by a short tube mounted in the immediate vicinity of the sample. This protected the detector from the radiation bypassed in the sample. The sample in a casette was immersed in the helium bath (4.2 K) of a cryostat with windows made from fused or crystalline quartz to limit the background intensity. This enabled us to increase manyfold the threshold sensitivity of both the detector and the samples in the photon energy range 7–12 and 10–30 meV. The spectra were studied using an LAFS-1000 Fourier spectrometer with Dacron optical splitters of thicknesses 12 and 6 μm.

In the impurity absorption and photoconductivity spectra, only allowed transitions from the populated states are seen. In the Ga-doped germanium at low temperatures, these are the transitions from the lower branch of the 1S state to the P states and to the valence band. Spectroscopic absorption studies can provide information on the energy spectrum restricted by these conditions. In this case, however, samples with a rather large optical thickness are required (either of a large

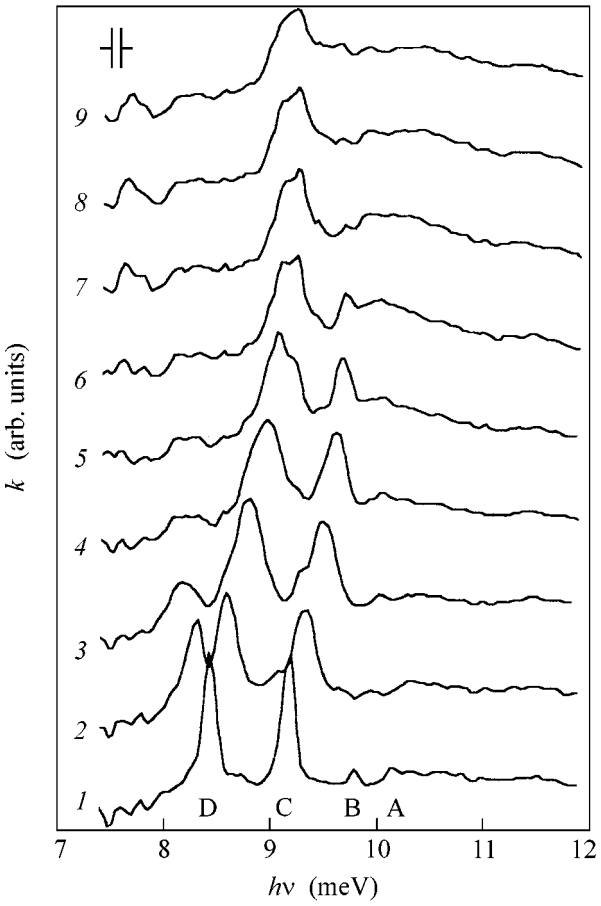

Fig. 1. Spectral dependences of the absorption coefficient k of the germanium sample ($2 \times 2 \times 10$ mm) doped with Ga with an concentration $N = 1.4 \times 10^{14}$ cm^{-3} under uniaxial compression in the [111] direction with pressure P (kbar): 0 (*1*), 0.23 (*2*), 0.47 (*3*), 0.7 (*4*), 0.93 (*5*), 1.16 (*6*), 1.4 (*7*), 1.6 (*8*), and 1.86 (*9*).

size or with a high impurity concentration). For the photoconductivity study, weak absorption in the sample is sufficient. However, in the photoelectric measurements, PC appears only upon the hole excitation to the valence band or to the local states that are close to it and capable of photothermal ionization. The results presented below were obtained by the most effective of these methods.

Figure 1 shows the absorption spectra of Ge(Ga) under low pressures applied in the [111] direction. For $P = 0$, the spectrum shows lines at the following energies $h\nu$ (meV): A(10.17), B(9.84), C(9.2), and D(8.44). The weak long-wavelength lines E(8) and F(6.74) are not seen in the figure. Considering that these lines appear upon hole excitation from the ground state, we will denote the final impurity states by the same letters. The ground-state energy of the Ga impurity in Ge is taken equal to 11.32 meV [10]. A theory of optical absorption and photoionization of group III acceptors in germanium was developed in [11]. Upon crystal compression, the ground state of the acceptor impurity splits into the lower ($1S_{1/2}$) and upper ($1S_{3/2}$) branches. The C state does not split, while the D state slightly splits upon compression in the [111] direction. The splitting of the D line into two components is due to the splitting of the ground state 1*S* and is observed up to $P \approx 1$ kbar. With increasing *P*, the thermal population of the upper branch decreases, and this component vanishes. A weak component splits off from the C line and shifts to lower energies [11], while the C component itself approaches the valence band ($P \approx 1$ kbar), reaches its edge ($P \approx 1.2$ kbar), and enters the allowed energy band ($P \approx 1.5$ kbar). It is seen that the decrease in the C-line intensity is accompanied by an increase in the absorption at the light-hole band edge, while the C line itself transforms into a broad band (≈1 meV) in the region of continuous spectrum and reduces its amplitude with an increase in pressure.

The subsequent evolution of the Ge impurity states with increasing pressure can be traced in the PC spectra (dashed curves in Fig. 2). One can see that the D line also approaches the light-hole band and is stabilized at the band edge at a distance of about 0.3 meV. With increasing pressure, this line is shifted toward low energies because of a decrease in the energy of the ground state $1S_{1/2}$. The band into which the C line transforms broadens upon an increase in *P* and finally turns into a step near 9 meV at high pressures. Simultaneously, the band slightly shifts deep in the light-hole band. At $P \approx$ 6 kbar a new broad band (marked by asterisk in Fig. 2) appears in the PC spectrum. This may be due to the splitting of the deep E or F state, whose upper energy levels reached the valence-band edge. It can be seen from Fig. 2 that all these bands are slightly shifted deep in the light-hole band even under high pressures. The studies in the region of 10–30 meV have revealed that the PC monotonically decreases upon an increase in the photon energy $h\nu$ until this energy becomes sufficient for the excitation to the heavy-hole band, after which the PC increases. The boundary between the PC regions corresponding to the light and heavy holes is clearly seen. It shifts to high energies in proportion to *P*. No local singularities indicating the presence of resonance impurity states in this spectral range were detected.

Splitting of the acceptor impurity states upon the compression of a germanium crystal in the [001] direction is more complicated (see [12] and literature cited therein) and more difficult to interpret. The PC spectra recorded upon the germanium deformation in this direction are presented in Fig. 3. It is seen that a number of peaks appearing under low pressures at the edge of continuous energy spectrum sequentially enter the light-hole band and transform into broad bands. With increasing *P*, only one of the D components remains outside the band, while all broad bands are concentrated in the energy interval near 2 meV above the D line. This interval is bounded by dashed curves in Fig. 3. As in the case of compression along the [111]

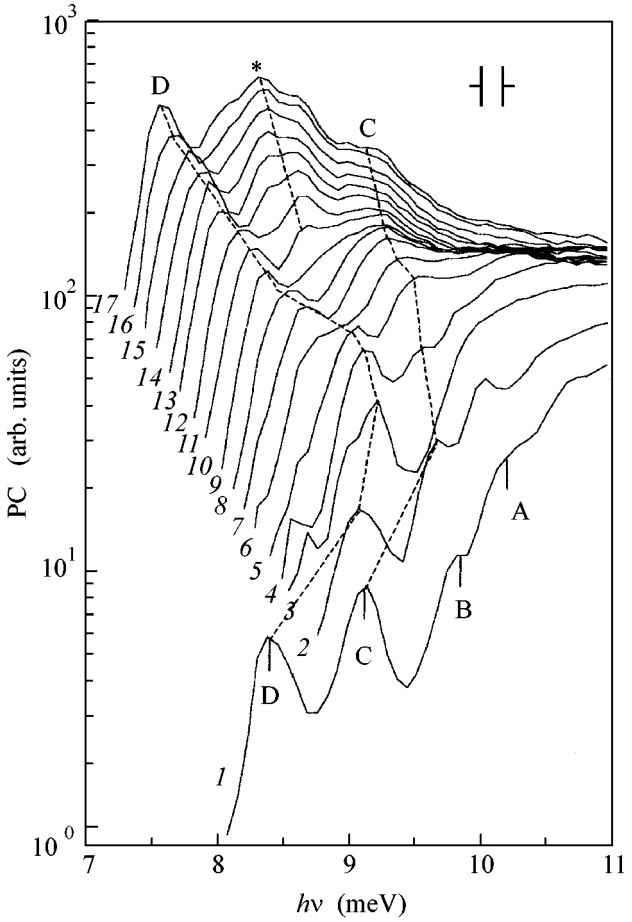

Fig. 2. Photoconductivity (PC) spectra of a Ge(Ga) sample ($1 \times 1 \times 10$ mm, 1.8×10^{14} cm^{-3}) [111] $\parallel P$ (kbar): 0 (*1*), 0.47 (*2*), 0.93 (*3*), 1.4 (*4*), 1.86 (*5*), 2.3 (*6*), 2.8 (*7*), 3.3 (*8*), 3.7 (*9*), 4.2 (*10*), 4.6 (*11*), 5.1 (*12*), 5.6 (*13*), 6.0 (*14*), 6.5 (*15*), 7.0 (*16*), and 7.4 (*17*). Dashed lines mark the energies of states C and D and a nonidentified state (asterisk).

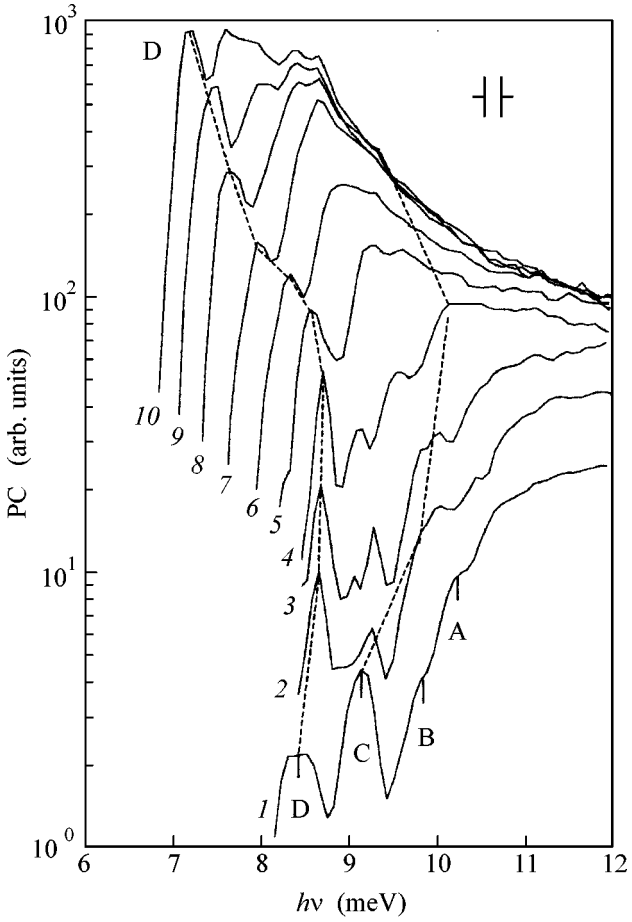

Fig. 3. PC spectra of a Ge(Ga) sample ($1 \times 1 \times 10$ mm, 5×10^{13} cm^{-3}) [001] $\parallel P$ (kbar): 0 (*1*), 0.93 (*2*), 1.4 (*3*), 1.86 (*4*), 2.3 (*5*), 2.8 (*6*), 3.3 (*7*), 3.7 (*8*), and 4.2 (*9*). Dashed lines single out the energy range where the excited states of the Ga impurity are seen.

direction, no local singularities are observed in the PC spectra at photon energies of 10–30 meV. The photoconductivity decreased monotonically until the heavy-hole PC appeared. An analogous result was obtained in [13] in the PC study of Ga-doped germanium compressed along the [001] direction. Although the positions calculated in [5] for the resonance states near the heavy-hole band edge were indicated in the spectra published in [13], no singularities in this energy range were seen in the figures. It is also possible that, due to a too high resolution in [13], strong interference in the sample did not permit one to trace the evolution of impurity states.

The obtained experimental results lead to the conclusion that the evolutions of the *P*-type states of the Ga impurity under the germanium axial compression in the [111] and [001] directions are similar. In the range of high pressures, where the stimulated emission can be excited [1, 2, 6–8], only the D state remains localized. The energy levels of other states are concentrated in the light-hole band near its edge, where these states show up as broad (≈1 meV) bands. Hence it follows that these states are resonant, i.e., lie inside the continuous energy spectrum and, thus, have short lifetimes ($\approx 10^{-11}$ s). This result contradicts the calculations [3–5]. It should be emphasized once again that the spectroscopic studies provide information only on the behavior of the *P*-type states to which the optical transitions from the acceptor ground state $1S_{1/2}$ are allowed. For example, the possibility of an alternative evolution of the *S*-type state cannot be ruled out. Consequently, the possible role of the resonance states can be clarified via investigation of the photoconductivity spectra and the absorption of spontaneous and stimulated radiation under identical conditions. It should be noted that the inverse population of the resonance states in the vicinity of the light-hole band edge can also result in the excitation of stimulated radiation. The appearance of such radiation at $P =$ 3.9 kbar in the [001] direction immediately after the Ga

impurity breakdown and for $h\nu \approx 10$ meV was reported in [14].

ACKNOWLEDGMENTS

We are grateful to V.P. Sinis for assistance in the experiments and to I.V. Altukhov, M.S. Kagan, and A.F. Polupanov for discussions of the results.

This study was supported by the Russian Foundation for Basic Research (project no. 04-02-1689) and EOARD (grant no. ISTC 2206p).

REFERENCES

1. I. V. Altukhov, M. S. Kagan, and V. P. Sinis, Pis'ma Zh. Éksp. Teor. Fiz. **47**, 136 (1988) [JETP Lett. **47**, 164 (1988)].
2. I. V. Altukhov, M. S. Kagan, K. A. Korolev, *et al.*, Zh. Éksp. Teor. Fiz. **101**, 756 (1992) [Sov. Phys. JETP **74**, 404 (1992)].
3. M. A. Odnoblyudov, A. A. Pakhomov, V. M. Chistyakov, *et al.*, Fiz. Tekh. Poluprovodn. (St. Petersburg) **31**, 1180 (1997) [Semiconductors **31**, 1014 (1997)].
4. M. A. Odnoblyudov, A. A. Prokof'ev, and I. N. Yassievich, Zh. Éksp. Teor. Fiz. **121**, 692 (2002) [JETP **94**, 593 (2002)].
5. V. Ya. Aleshkin, V. I. Gavrilenko, and D. V. Kozlov, Zh. Éksp. Teor. Fiz. **120**, 1495 (2001) [JETP **93**, 1296 (2001)].
6. I. V. Altukhov, M. S. Kagan, K. A. Korolev, *et al.*, Pis'ma Zh. Éksp. Teor. Fiz. **59**, 455 (1994) [JETP Lett. **59**, 476 (1994)].
7. I. V. Altukhov, M. S. Kagan, K. A. Korolev, *et al.*, Fiz. Tekh. Poluprovodn. (St. Petersburg) **30**, 1091 (1996) [Semiconductors **30**, 578 (1996)].
8. I. V. Altukhov, M. S. Kagan, K. A. Korolev, *et al.*, Zh. Éksp. Teor. Fiz. **115**, 89 (1999) [JETP **88**, 51 (1999)].
9. A. K. Ramdas and S. Rodrigues, Rep. Prog. Phys. **44**, 1287 (1981).
10. G. B. Wright and A. Mooradian, Phys. Rev. Lett. **18**, 608 (1967).
11. Sh. M. Kogan and A. F. Polupanov, Zh. Éksp. Teor. Fiz. **80**, 394 (1981) [Sov. Phys. JETP **53**, 201 (1981)].
12. R. L. Jones and P. Fisher, Phys. Rev. B **2**, 2016 (1970).
13. V. Y. Aleshkin, A. V. Gavrilenko, V. I. Gavrilenko, *et al.*, Phys. Status Solidi C **0**, 680 (2003).
14. Yu. P. Gousev, I. V. Altukhov, E. G. Chirkova, *et al.*, Appl. Phys. Lett. **75**, 757 (1999).

Translated by N. Wadhwa

JETP Letters, Vol. 80, No. 5, 2004, pp. 339–342. Translated from Pis'ma v Zhurnal Éksperimental'noĭ i Teoreticheskoĭ Fiziki, Vol. 80, No. 5, 2004, pp. 385–388.

The Effect of Uniaxial Static Pressure on the Behavior of an Aluminum Acceptor Impurity in Silicon

T. N. Mamedov[1,*], D. Andreica[2], D. G. Andrianov[3], D. Herlach[4], V. N. Gorelkin[5], K. I. Gritsai[1], V. A. Zhukov[1], A. V. Stoikov[1, 4], and U. Zimmermann[4]

[1]*Joint Institute for Nuclear Research, Dubna, Moscow region, 141980 Russia*

**e-mail: tmamedov@nu.jinr.ru*

[2]*University Babes–Bolyai, 3400 Cluj-Napoca, Romania*

[3]*State Research and Design Institute of Rare Metals "Giredmet," Moscow, 109017 Russia*

[4]*Paul Scherrer Institute, CH-5232 Villigen, Switzerland*

[5]*Moscow Institute of Physics and Technology, Dolgoprudnyĭ, Moscow region, 141700 Russia*

Received July 22, 2004

The effect of uniaxial compression on the behavior of shallow aluminum acceptor centers in silicon has been studied. The $_{\mu}$Al impurity atoms were created by implanting negative muons into silicon single crystals doped with phosphorus to 1.6×10^{13} cm^{-3} (sample 1) and 1.9×10^{13} cm^{-3} (sample 2). The muon polarization was studied in the temperature range 10–300 K. Measurements were performed in a magnetic field of 2.5 kG oriented perpendicularly to the muon spin. The samples were oriented so that the selected crystal axis ([111] and [100] in samples 1 and 2, respectively), the magnetic field, and the initial muon-spin polarization were mutually perpendicular. External pressure applied to the sample along the indicated crystal axis changed both the absolute value of the acceptor magnetic-moment relaxation rate and the character of its temperature dependence. © *2004 MAIK "Nauka/Interperiodica".*

PACS numbers: 71.55.Cn; 76.75.+i

INTRODUCTION

In recent years, a gap in the experimental investigation of the interactions between shallow acceptor impurities in the silicon crystal lattice was filled thanks to the use of polarized negative muon beams. This approach provided data on (i) the hyperfine interaction at the acceptor center (AC), (ii) the rate and mechanisms of magnetic-moment relaxation of this center, (iii) the scattering of free charge carriers (electrons and holes) by such centers in silicon crystals with the acceptor impurity concentration close to or higher than the critical value (n_c) corresponding to the semiconductor–metal transition, (iv) the interactions between impurities, and (v) the AC ionization mechanism and ionization rate in the nondegenerate *n*- and *p*-type silicon [1–4]. Although the impurities and defects in semiconductors have been studied for more than half a century, the above data on the behavior of shallow acceptor levels in silicon were obtained for the first time.

This paper presents the results of our investigation into the effect of uniaxial stress on the behavior of shallow aluminum acceptor centers in silicon crystals (see also [5, 6]). Interest in the investigation of the behavior of such acceptor impurities in strained silicon crystals is caused by a number of factors. As is known, the silicon crystal lattice in the epitaxially grown layers (e.g., on germanium or diamond substrates) and heterostructures occurs in a strained state. This state is analogous to that arising in a crystal compressed in the direction perpendicular to the surface of the substrate on which the crystal was grown. The possibility of using strained silicon doped with a donor or acceptor impurity for the creation of a prototype of the quantum computer is being extensively discussed [7, 8]. Another factor stimulating investigations into the behavior of acceptor impurities in strained silicon is the possibility of refining the AC Hamiltonian in semiconductors with diamond like crystal structure. In the general case, this Hamiltonian has a rather complicated form [9].

The first experimental evidence of the effect of silicon-crystal strain on the behavior of acceptor centers was obtained in EPR studies [10, 11]. The possibility of using polarized negative muons for studying acceptor impurities in silicon is thanks to the fact that, upon muon trapping, Si atom converts into a muonic atom $_{\mu}$Al that is analogous to an aluminum atom with respect of the electron shell structure. The muon-spin polarization depends on the electron-shell state (paramagnetic or diamagnetic) of the muonic atom (AC), on the hyperfine interaction in the AC, and on its interaction with the environment.

EXPERIMENTAL

Measurements were performed using a GPD spectrometer [12] placed at the μE1 muon channel of the

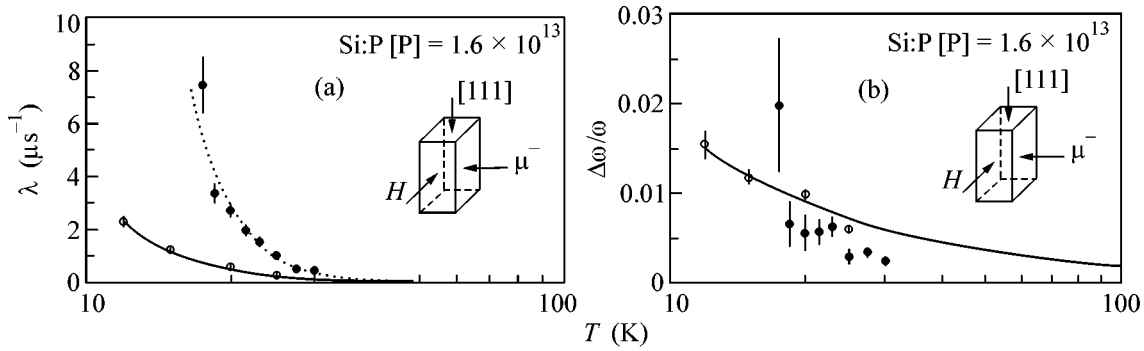

Fig. 1. Temperature dependences of the (a) muon-spin relaxation rate and (b) precession-frequency shift in a silicon crystal with a phosphorus-impurity concentration of 1.6×10^{13} cm^{-3} (sample 1), measured in the absence of applied pressure (open circles) and under a pressure of 3 kbar (closed circles). The curves are drawn (a) by least squares and (b) as a guide to the eye.

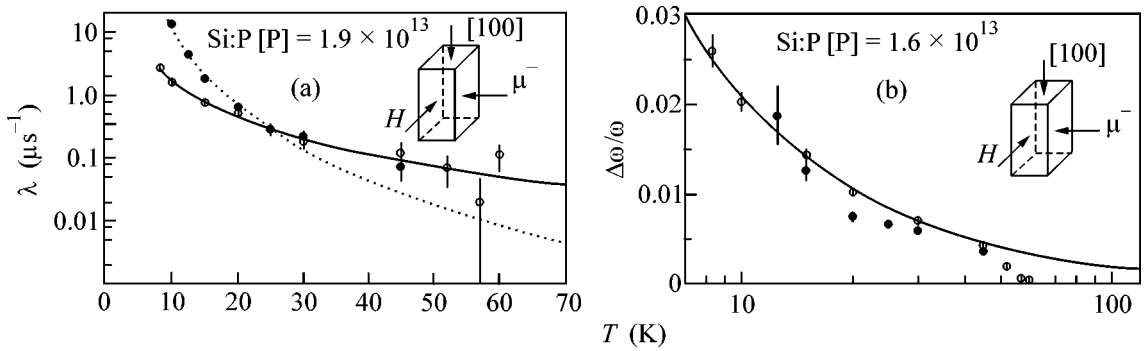

Fig. 2. Temperature dependences of the (a) muon-spin relaxation rate and (b) precession-frequency shift in silicon with a phosphorus-impurity concentration of 1.9×10^{13} cm^{-3} (sample 2), measured in the absence of applied pressure (open circles) and under a pressure of 1.7 kbar (closed circles). The curves are drawn by least squares.

proton accelerator of the Paul Scherrer Institute (PSI, Switzerland). Samples cut from silicon single crystals had the shape of a regular tetrahedral prism with a 9.5 × 9.5 mm base and a height of 22 mm. Two samples doped with phosphorus to 1.6×10^{13} cm^{-3} (sample 1) and 1.9×10^{13} cm^{-3} (sample 2) were studied. The samples were oriented so that a selected crystal axis ([111] and [100] in samples 1 and 2, respectively) was perpendicular to the base (to within ±1°). A uniform magnetic field applied to the samples was produced by Helmholtz coils. The magnetic field had a strength of 2.5 kG and a long-term stability no worse than 10^{-4}. It was oriented so that the field vector, selected crystal axis ([111] and [100] in samples 1 and 2, respectively), and the initial muon-spin polarization were mutually perpendicular.

The crystal samples were uniaxially stressed in a high-pressure cell. The cell was made of a heat-treated beryllium bronze and allowed a pressure of up to 5 kbar to be applied to the sample base. The applied pressure (i.e., the stress in the sample) was monitored using a tensoresistor of the EV001 P1-5-350B type (NIIFI, Penza). The pressure sensor was glued to one of the prism faces with a BF-2 glue, after which the glue was polymerized at a high-temperature. The cell with a fixed pressure was placed into a cryostat cooled by liquid helium vapor. The sample temperature in the range from 4 to 300 K was maintained with an accuracy of 0.1 K.

The time evolution of the muon polarization $P(t)$ in the sample was studied by measuring the decay electrons from the reaction $\mu^- \longrightarrow e^- + \bar{\nu}_e + \nu_\mu$. The time dependence of the number of detected electrons is described by the exponential modulated by the $P(t)$ function. The measurement technique and the procedure used for reconstructing the parameters of muon-spin polarization from the experimental μ^-SR spectra are described in detail in [1, 2].

RESULTS

Figures 1 and 2 show the experimentally measured temperature dependences of the relaxation rate λ and the shift $\Delta\omega/\omega_0$ of the muon-spin precession frequency for silicon crystals with a phosphorus-impurity concentration of 1.6×10^{13} cm^{-3} (sample 1) and 1.9×10^{13} cm^{-3}

(sample 2), respectively. The shift of the precession frequency was defined as the difference $\Delta\omega = \omega - \omega_0$ between the precession frequencies ω at a temperature T and at room temperature.

The arrows in the insets in Figs. 1 and 2 indicate the mutual orientation of the applied magnetic field, the crystal axis, and the initial muon polarization. The pressure was applied along the indicated crystal axis and amounted to 3.0 and 1.7 kbar for samples 1 and 2, respectively. The results of measurements for the samples under the applied static pressure are compared with the data obtained in the absence of loading.

As can be seen in Figs. 1 and 2, the application of an external pressure leads to a significant change in the muon-spin relaxation rate. Moreover, the character of the temperature dependence of relaxation rate also changes. In contrast to the relaxation rate, the effect of pressure on the shift of muon-spin precession frequency is insignificant in both samples. These results do not contradict the theoretical estimates [13], according to which the most pronounced effect of an external pressure on the frequency shift is expected for a silicon crystal compressed along the [011] axis.

According to [14], the following relationships hold between the quantities characterizing the time evolution of the muon-polarization vector at the 1*S* level of $_\mu$Al atom and the parameters characterizing the interaction of this AC in the silicon crystal lattice:

$$\frac{\Delta\omega}{\omega_0} = -\frac{g\mu_B}{2\mu_B^\mu}\frac{J(J+1)A}{3k_BT}, \quad (1)$$

$$\lambda = \frac{J(J+1)}{3}\left(\frac{(A/\hbar)^2}{\nu} + \frac{(A/\hbar)^2\nu}{\nu^2+\omega_e^2}\right). \quad (2)$$

Here, A is the hyperfine interaction constant between the muon and the AC electron shell; ν is the magnetic-moment relaxation rate of this center; $\hbar = h/2\pi$; h is Planck's constant; k_B is Boltzmann's constant; μ_B and μ_B^μ are the Bohr magneton for electron and muon, respectively; g is the AC g factor; $\omega_e = g\mu_B B/\hbar$ is the angular frequency of precession of the magnetic moment of the AC electron shell in magnetic field B; and T is temperature. For a shallow acceptor center in silicon, $J = 3/2$ [9] and $g = -1.07$ [15].

By fitting relation (1) to the experimental data on the muon-spin precession-frequency shift for sample 2 at $T \lesssim 50$ K, we obtained the hyperfine spitting constants $A/h = 32 \pm 0.9$ MHz in the absence and $A/h = 26.3 \pm 1.0$ MHz in the presence of external pressure. The curve in Fig. 1b corresponds to the best approximation of experimental data obtained in the absence of pressure.

The experimental temperature dependence of the muon spin-relaxation rate was approximated by Eq. (2), assuming [2] that the hyperfine splitting constant is $A/h = 26.5$ MHz and that the magnetic-moment relaxation rate of the acceptor center depends on the temperature as $\nu = CT^\alpha$. The values of the coefficient C and the parameter α for the samples studied are given in the table.

Parameters of the temperature dependence of the magnetic moment relaxation rate $\nu = CT^\alpha$ for an acceptor center in silicon

	Sample 1		Sample 2	
Pressure, kbar	0	3	0	1.7
C, μs^{-1}	4.4 ± 2.6	0.02 ± 0.01	60 ± 20	0.150.08
α	2.7 ± 0.2	4.8 ± 0.3	2.0 ± 0.1	3.80.2

For sample 1, the value of α in the absence of pressure is close to three, which is in good agreement with our previous results (see, e.g., [2]) for this sample. For sample 2 in the absence of external pressure, we obtained $\alpha \simeq 2$. It should be noted that, for more than ten n- and p-type silicon samples with impurity concentrations $\lesssim 2 \times 10^{17}$ cm^{-3} studied previously in the unloaded state, we obtained $\alpha \simeq 3$ [2]. The fact that the value of α for sample 2 in the unloaded state is close to two likely indicates that the relaxation rate ν depends on the mutual orientation of the crystal axis and the magnetic field.

One can see from the data in the table that the external static pressure leads to a decrease of more than two orders of magnitude in the value of the coefficient C in the expression for the magnetic-moment relaxation rate of the acceptor center, while the parameter α increases approximately by two units.

The observed dependence of the relaxation rate of the AC magnetic moment on the external pressure in silicon is quite understandable from a theoretical standpoint, although the quantitative calculations of this effect have not been performed so far (because of considerable computational difficulties). According to [9], a fourfold-degenerate state in the absence of strain

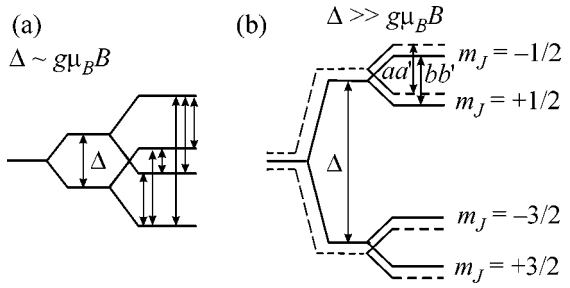

Fig. 3. Level splitting in the ground state of a shallow acceptor center in silicon in a magnetic field B (a) in the absence of compression and (b) in uniaxially compressed crystal with the strain energy Δ. Dashed lines in (b) show the additional splitting caused by the random internal stresses.

effectively interacts with the phonon field, causing a high relaxation rate of the AC magnetic moment even at low temperatures. Under pressure, the fourfold-degenerate state of this center splits into two Kramers doublets (Fig. 3). The interaction of these doublets with phonons is weak and, accordingly, the relaxation rate of the AC magnetic moment decreases.

CONCLUSION

We have demonstrated experimentally that the uniaxial static compression at temperatures below 50 K significantly modifies the temperature dependence of the relaxation rate of the AC magnetic moment in silicon. In order to gain more detailed information about the effect of an external pressure on the interaction between the acceptor impurity and the silicon crystal lattice, we are planning to study the dependence of the muon-spin relaxation rate and the precession-frequency shift on the external pressure and on the magnetic-field orientation about the crystal axis.

We are grateful to V.S. Egorov (Russian Research Center, Kurchatov Institute, Moscow) for providing the pressure sensor, to N.Ya. Minina (Moscow State University) for consulting on the use of tensoresistors for measuring the pressure in crystals, and to the direction of the Paul Scherrer Institute (Switzerland) for the opportunity to conduct measurements. This study was performed at the Dzhelepov Laboratory of Nuclear Problems (JINR) and supported by the Russian Foundation for Basic Research, project no. 02-02-16881.

REFERENCES

1. T. N. Mamedov, I. L. Chaplygin, V. N. Duginov, *et al.*, J. Phys.: Condens. Matter **11**, 2849 (1999).
2. T. N. Mamedov, A. V. Stoĭkov, and V. N. Gorelkin, Fiz. Élem. Chastits At. Yadra **33**, 1005 (2002) [Phys. Part. Nucl. **33**, 519 (2002)].
3. T. N. Mamedov, D. Herlach, V. N. Gorelkin, *et al.*, Physica B (Amsterdam) **326**, 97 (2003).
4. T. N. Mamedov, D. G. Andrianov, D. Herlach, *et al.*, Pis'ma Zh. Éksp. Teor. Fiz. **79**, 25 (2004) [JETP Lett. **79**, 21 (2004)].
5. T. N. Mamedov, D. Andreica, D. G. Andrianov, *et al.*, PSI Sci. Rep. **ILL**, 115 (2002).
6. T. N. Mamedov, D. Andreica, D. G. Andrianov, *et al.*, PSI Sci. Rep. **ILL**, 123 (2003).
7. Belita Koiller, Xuedong Hu, and S. Das Sarma, Phys. Rev. B **66**, 115201 (2002).
8. B. Golding and M. I. Dykman, cond-mat/0309147 (2003).
9. G. L. Bir and G. E. Pikus, *Symmetry and Strain-Induced Effects in Semiconductors* (Nauka, Moscow, 1972; Wiley, New York, 1975).
10. G. Feher, J. C. Hensel, and E. A. Gere, Phys. Rev. Lett. **5**, 309 (1960).
11. G. W. Ludwig and H. H. Woodbury, Bull. Am. Phys. Soc. **1**, 118 (1961).
12. R. Abela, C. Baines, X. Donath, *et al.*, Hyperfine Interact. **87**, 1105 (1994).
13. A. Baturin and V. N. Gorelkin, in *Proceedings of XXXVII School of St. Petersburg Institute of Nuclear Physics* (in press).
14. V. N. Gorelkin, T. N. Mamedov, and A. S. Baturin, Physica B (Amsterdam) **289–290**, 585 (2000).
15. H. Neubrand, Phys. Status Solidi B **86**, 269 (1978).

Translated by P. Pozdeev

JETP Letters, Vol. 80, No. 5, 2004, pp. 343–347. From Pis'ma v Zhurnal Éksperimental'noĭ i Teoreticheskoĭ Fiziki, Vol. 80, No. 5, 2004, pp. 389–394.

Quantum Phase Transition for the BEC–BCS Crossover in Condensed Matter Physics and CPT Violation in Elementary Particle Physics¶

F. R. Klinkhamer[1, *] and G. E. Volovik[2, 3, **]

[1] *Institute for Theoretical Physics, University of Karlsruhe (TH), 76128 Karlsruhe, Germany*
** e-mail: frans.klinkhamer@physik.uni-karlsruhe.de*
[2] *Low Temperature Laboratory, Helsinki University of Technology, FIN-02015 HUT, Finland*
[3] *Landau Institute for Theoretical Physics, Russian Academy of Sciences, Moscow, 117940 Russia*
*** e-mail: volovik@boojum.hut.fi*
Received July 23, 2004

We discuss the quantum phase transition that separates a vacuum state with fully gapped fermion spectrum from a vacuum state with topologically protected Fermi points (gap nodes). In the context of condensed-matter physics, such a quantum phase transition with Fermi point splitting may occur for a system of ultracold fermionic atoms in the region of BEC–BCS crossover, provided Cooper pairing occurs in the non-*s*-wave channel. For elementary particle physics, the splitting of Fermi points may lead to CPT violation, neutrino oscillations, and other phenomena. © *2004 MAIK "Nauka/Interperiodica".*

PACS numbers: 11.30.Er; 71.10.-w; 73.43.Nq

There are two major schemes for the classification of states in condensed matter physics and relativistic quantum field theory: classification by symmetry and by universality classes.

For the first classification method, a given state of the system is characterized by the symmetry group H, which is a subgroup of the symmetry group G of the relevant physical laws (see, e.g., [1] for symmetry classification of superconducting states). The thermodynamic phase transition between equilibrium states is usually marked by a change of the symmetry group H. The subgroup H is also responsible for topological defects, which are determined by the nontrivial elements of the homotopy groups $\pi_n(G/H)$ (cf. [2]).

The second classification method deals with the ground states of the system at zero temperature ($T = 0$), i.e., it is the classification of quantum vacua. The universality class determines the general features of the quantum vacuum, such as the linear response and the energy spectrum of fermionic excitations. For translation-invariant systems in which momentum is a well-defined quantity, these features of the fermionic quantum vacuum are determined by momentum-space topology. For (3 + 1)-dimensional systems, there are only three basic universality classes of fermionic vacua [3]: (i) vacua with fully gapped fermionic excitations, (ii) vacua with fermionic excitations characterized by Fermi points (the excitations behave as massless Weyl fermions close to the Fermi points), and (iii) vacua with fermionic excitations characterized by Fermi surfaces. (Fermi points $\mathbf{p}_n$ are points in three-momentum space at which the energy vanishes, $E(\mathbf{p}_n) = 0$, and similarly for Fermi surfaces S_n, with $E(\mathbf{p}) = 0$ for $\mathbf{p} \in S_n$.)

It may happen that, by changing some parameter q of the system, we transfer the vacuum state from one universality class to another without changing its symmetry group H. The point q_c, where this zero-temperature transition occurs, marks the quantum phase transition. For $T \neq 0$, the phase transition is absent, as the two states belong to the same symmetry class H. Hence, there is an isolated singular point $(q_c, 0)$ in the (q, T) plane. Two examples of a quantum phase transition are (i) the Lifshitz transition in crystals, at which the Fermi surface changes its topology or shrinks to a point, and (ii) the transition between states with different values of Hall (or spin-Hall) conductance in (2 + 1)-dimensional systems.

In this letter, we discuss the quantum phase transition between a vacuum with fully gapped fermionic excitations and a vacuum with Fermi points. At the transition point $q = q_c$, a topologically trivial Fermi point emerges from the fully gapped state. This marginal Fermi point then splits into two or more topologically nontrivial Fermi points (see figure). The topologically protected Fermi points give rise to anomalous properties of the system in the low-temperature regime (cf. Section 7.3.2 of [4] and Part IV of [3]).

These effects may occur in a system of ultracold fermionic atoms in the region of BEC–BCS crossover in a

¶ This article was submitted by the authors in English.

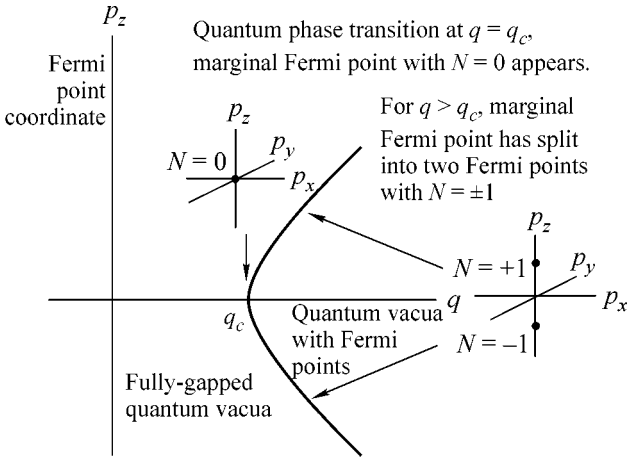

Quantum phase transition at $q = q_c$ between a fully gapped vacuum and a vacuum with topologically protected Fermi points (gap nodes). At $q = q_c$, there appears a marginal Fermi point with topological charge $N = 0$ (inset at the top). For $q > q_c$, the marginal Fermi point has split into two Fermi points characterized by nonzero topological invariants $N = \pm 1$ (inset on the right). For a system of ultracold fermionic atoms qualitatively described by Hamiltonians (1) and (9), the critical parameter is $q_c = 0$ [note that eight Fermi points emerge for the case of Hamiltonian (9)]. For Dirac fermions with CPT violation in Hamiltonian (6), the parameter q is chosen as $q \equiv |\mathbf{b}|$ and the critical parameter is $q_c = M$.

non-*s*-wave Cooper channel. Superfluidity in the BEC regime and the BEC–BCS crossover has been observed for ^{40}K and ^{6}Li atoms [5–9]. In these experiments, a magnetic-field Feshbach resonance was used to control the interactions in the *s*-wave channel. For the case of *s*-wave pairing, there are fully gapped vacua on both sides of the crossover and there is no quantum phase transition. If, however, the pairing occurs in a non-*s*-wave channel, a quantum phase transition may be expected between the fully gapped state and the state with Fermi points. It was reported recently [10, 11] that three *p*-wave Feshbach resonances were found for ^{6}Li atoms. This suggests the possibility of future observations of non-*s*-wave pairing and of the quantum phase transition associated with the splitting of Fermi points.

Here, we will discuss two examples of such a transition, using, for simplicity, *p*-wave spin-triplet pairing and their possible analogs in relativistic quantum field theory. We also argue in the following that a similar quantum phase transition characterized by Fermi point splitting may occur for the Standard Model of elementary particle physics [12], but refer the reader to [13–15] for further details. In fact, condensed-matter physics provides us with a broad class of quantum field theories not restricted by Lorentz invariance, which allows us to consider many problems in the relativistic quantum field theory of the Standard Model from a more general perspective. Just as for nonrelativistic systems, the basic properties of relativistic quantum field theories (including quantum anomalies) are determined by momentum-space topology, which classifies relativistic vacua according to the same three universality classes.

Since we are only interested in effects determined by the topology and the symmetry of the fermionic Green's function $G(p)$, we do not require a special form of the Green's function and can choose the simplest one with the required topology. First, consider the Bogoliubov–Nambu Hamiltonian, which qualitatively describes fermionic quasiparticles in the axial state of *p*-wave pairing. This Hamiltonian can be applied to both the Bardeen–Cooper–Schrieffer (BCS) and Bose-Einstein condensation (BEC) regimes, and also to superfluid ^{3}He–A [4]. Specifically, the Bogoliubov–Nambu Hamiltonian is given by

$$H = \begin{pmatrix} |\mathbf{p}|^2/2m - q & c_\perp \mathbf{p}\cdot(\hat{\mathbf{e}}_1 + i\hat{\mathbf{e}}_2) \\ c_\perp \mathbf{p}\cdot(\hat{\mathbf{e}}_1 - i\hat{\mathbf{e}}_2) & -|\mathbf{p}|^2/2m + q \end{pmatrix}, \quad (1)$$

and $G^{-1}(i\omega, \mathbf{p}) = i\omega - H(\mathbf{p})$, with $\hbar = 1$. Fermionic atoms of mass m with a given direction of the atomic spin are considered, assuming that only these atoms experience Feshbach resonance. The orthonormal triad ($\hat{\mathbf{e}}_1$, $\hat{\mathbf{e}}_2$, $\hat{\mathbf{l}} \equiv \hat{\mathbf{e}}_1 \times \hat{\mathbf{e}}_2$) and maximum transverse speed $c_\perp$ of the quasiparticles characterize the order parameter in the axial state of triplet superfluid. The unit vector $\hat{\mathbf{l}}$ corresponds to the direction of orbital momentum of the Cooper pair or the diatomic molecule. We further assume that the parameter q is controlled by the magnetic field in the vicinity of the Feshbach resonance.

The energy spectrum of these Bogoliubov–Nambu fermions is

$$E^2(\mathbf{p}) = \left(\frac{|\mathbf{p}|^2}{2m} - q\right)^2 + c_\perp^2(\mathbf{p}\times\hat{\mathbf{l}})^2. \quad (2)$$

The BCS regime occurs for $q > 0$, with the parameter q playing the role of a chemical potential. In this regime, there are two Fermi points, i.e., points in three-momentum space with $E(\mathbf{p}) = 0$. For energy spectrum (2), the Fermi points are $\mathbf{p}_1 = p_F\hat{\mathbf{l}}$ and $\mathbf{p}_2 = -p_F\hat{\mathbf{l}}$, with Fermi momentum $p_F = \sqrt{2mq}$.

For a general system, be it relativistic or nonrelativistic, the stability of the ath Fermi point is guaranteed by the topological invariant N_a, which can be written as a surface integral in frequency-momentum space. In terms of the fermionic propagator $G = G(p_0, p_1, p_2, p_3)$, for $p_\mu = (\omega, \mathbf{p})$, the topological invariant is [3]

$$N_a \equiv \frac{1}{24\pi^2}\epsilon_{\mu\nu\rho\sigma}\mathrm{tr}\oint_{\Sigma_a} dS^\sigma G\frac{\partial}{\partial p_\mu}G^{-1}G\frac{\partial}{\partial p_\nu}G^{-1}G\frac{\partial}{\partial p_\rho}G^{-1}, \quad (3)$$

where Σ_a is a three-dimensional surface around the isolated Fermi point $p_{\mu a} = (0, \mathbf{p}_a)$ and "tr" stands for the trace over the relevant spin indices.

For the case considered, the trace in Eq. (3) is over the Bogoliubov–Nambu spin and the two Fermi points $\mathbf{p}_1$ and $\mathbf{p}_2$ have nonzero topological charges $N_1 = +1$ and $N_2 = -1$. The density of states in this gapless regime is given by $\nu(E) \propto E^2$. At $q = 0$, these two Fermi points merge and form one topologically trivial Fermi point with $N = 0$. This intermediate state, which appears at the quantum phase transition ($q_c = 0$), is marginal: the momentum-space topology is trivial and cannot protect the vacuum against decay into one of the two topologically stable vacua. For $q < 0$, the marginal Fermi point disappears altogether and the spectrum becomes fully-gapped. In this topologically stable fully-gapped vacuum, the density of states is drastically different from that in the topologically stable gapless regime: $\nu(E) = 0$ for $E < |q|$. All this demonstrates that the quantum phase transition considered is of purely topological origin.

Note that, if a single pair of Fermi points appears in momentum space, the vacuum state has nonzero internal angular momentum along $\hat{\mathbf{l}}$, i.e., this quantum vacuum has the property of an orbital ferromagnet. Later, we will discuss an example with multiple Fermi points, for which the total orbital momentum is zero and the vacuum state corresponds to an orbital antiferromagnet.

We now turn to elementary particle physics [12]. It appears that the vacuum of the Standard Model above the electroweak transition (vanishing fermion masses) is marginal: there is a multiply degenerate Fermi point $\mathbf{p} = 0$ with topological charge $N = 0$. It is therefore the intermediate state between two topologically stable vacua, the fully gapped vacuum and the vacuum with topologically nontrivial Fermi points. In the Standard Model, this marginal Fermi point is protected by symmetries, namely the continuous electroweak symmetry (or the discrete symmetry discussed in Section 12.3.2 of [3]) and the CPT symmetry.

Explicit violation or spontaneous breaking of one of these symmetries transforms the marginal vacuum of the Standard Model into one of the two topologically stable vacua. If, for example, the electroweak symmetry is broken, the marginal Fermi point disappears and the fermions become massive. This is known to happen in the case of quarks and electrically charged leptons below the electroweak transition. If, on the other hand, the CPT symmetry is violated, the marginal Fermi point splits into topologically stable Fermi points. One can speculate that the latter happens for the Standard Model, in particular with the electrically neutral leptons, the neutrinos [13–15]. The splitting of Fermi points may also give rise to a CPT-violating Chern–Simons-like term in the effective gauge field action [16, 17], as will be discussed later.

Let us first consider this scenario for a marginal Fermi point describing a *single* pair of relativistic chiral fermions, that is, one right-handed fermion and one left-handed fermion. These are Weyl fermions with Hamiltonians $H_{\text{right}} = \boldsymbol{\sigma} \cdot \mathbf{p}$ and $H_{\text{left}} = -\boldsymbol{\sigma} \cdot \mathbf{p}$, where $\boldsymbol{\sigma}$ denotes the triplet of Pauli matrices and natural units are employed with $c = \hbar = 1$. Each of these Hamiltonians has a topologically stable Fermi point, $\mathbf{p} = 0$. The corresponding inverse Green's functions are given by

$$\begin{aligned} G^{-1}_{\text{right}}(i\omega, \mathbf{p}) &= i\omega - \boldsymbol{\sigma} \cdot \mathbf{p}, \\ G^{-1}_{\text{left}}(i\omega, \mathbf{p}) &= i\omega + \boldsymbol{\sigma} \cdot \mathbf{p}. \end{aligned} \tag{4}$$

The positions of the Fermi points coincide—$\mathbf{p}_1 = \mathbf{p}_2 = 0$—but their topological charges (3) are different. For this simple case, the topological charge equals the chirality of the fermions, $N_a = C_a$ (i.e., $N = +1$ for the right-handed fermion and $N = -1$ for the left-handed one). The total topological charge of the Fermi point $\mathbf{p} = 0$ is therefore zero.

The splitting of this marginal Fermi point can be described by the Hamiltonians $H_{\text{right}} = \boldsymbol{\sigma} \cdot (\mathbf{p} - \mathbf{p}_1)$ and $H_{\text{left}} = -\boldsymbol{\sigma} \cdot (\mathbf{p} - \mathbf{p}_2)$, with $\mathbf{p}_1 = -\mathbf{p}_2 \equiv \mathbf{b}$ from momentum conservation. The real vector $\mathbf{b}$ is assumed to be odd under CPT, which introduces CPT violation into the physics. The 4×4 matrix of the combined Green's function has the form

$$G^{-1}(i\omega, \mathbf{p}) = \begin{pmatrix} i\omega - \boldsymbol{\sigma} \cdot (\mathbf{p} - \mathbf{b}) & 0 \\ 0 & i\omega + \boldsymbol{\sigma} \cdot (\mathbf{p} + \mathbf{b}) \end{pmatrix}. \tag{5}$$

Equation (3) shows that $\mathbf{p}_1 = \mathbf{b}$ is the Fermi point with topological charge $N = +1$ and $\mathbf{p}_2 = -\mathbf{b}$ the Fermi point with topological charge $N = -1$.

Let us now consider the more general situation with both the electroweak and CPT symmetries broken. The Hamiltonian has, then, an additional mass term,

$$\begin{aligned} H &= \begin{pmatrix} \boldsymbol{\sigma} \cdot (\mathbf{p} - \mathbf{b}) & M \\ M & -\boldsymbol{\sigma} \cdot (\mathbf{p} + \mathbf{b}) \end{pmatrix} \\ &= H_{\text{Dirac}} - \mathbf{I}_2 \otimes (\boldsymbol{\sigma} \cdot \mathbf{b}). \end{aligned} \tag{6}$$

This Hamiltonian is the typical starting point for investigations of the effects of CPT violation in the fermionic sector (see, e.g., [18, 19] and references therein). The energy spectrum of Hamiltonian (6) is

$$E^2_{\pm}(\mathbf{p}) = M^2 + |\mathbf{p}|^2 + q^2 \pm 2q\sqrt{M^2 + (\mathbf{p} \cdot \hat{\mathbf{b}})^2}, \tag{7}$$

with $\hat{\mathbf{b}} \equiv \mathbf{b}/|\mathbf{b}|$ and $q \equiv |\mathbf{b}| \geq 0$.

Allowing for a variable parameter q, one finds a quantum phase transition at $q_c = M$ between fully gapped vacua for $q < M$ and vacua with two Fermi points for $q > M$. These Fermi points are given by

$$\begin{aligned} \mathbf{p}_1 &= +\hat{\mathbf{b}}\sqrt{q^2 - M^2}, \\ \mathbf{p}_2 &= -\hat{\mathbf{b}}\sqrt{q^2 - M^2}. \end{aligned} \tag{8}$$

Equation (3), now with a trace over the indices of the 4×4 Dirac matrices, shows that $\mathbf{p}_1$ is the Fermi point

with topological charge $N = +1$ and $\mathbf{p}_2$ the Fermi point with topological charge $N = -1$ [see figure, for $\hat{\mathbf{b}} = (0, 0, 1)$]. The magnitude of the splitting of the two Fermi points is given by $2\sqrt{q^2 - M^2}$. At the quantum phase transition $q_c = M$, the Fermi points with opposite charge annihilate each other and form a marginal Fermi point $\mathbf{p}_0 = 0$. The momentum-space topology of this marginal Fermi point is trivial (topological invariant $N = +1 - 1 = 0$).

The full Standard Model contains *eight* pairs of chiral fermions per family and a quantum phase transition can be characterized by the appearance and splitting of multiple marginal Fermi points. For systems of cold atoms, an example is provided by another spin-triplet *p*-wave state, the so-called α-phase with orbital antiferromagnetism. The Bogoliubov–Nambu Hamiltonian, which qualitatively describes fermionic quasiparticles in the α-state, is given by [1, 4]:

$$H = \begin{pmatrix} |\mathbf{p}|^2/2m - q & (\Sigma \cdot \mathbf{p})c_\perp/\sqrt{3} \\ (\Sigma \cdot \mathbf{p})^\dagger c_\perp/\sqrt{3} & -|\mathbf{p}|^2/2m + q \end{pmatrix}, \quad (9)$$

with $|\mathbf{p}|^2 \equiv p_x^2 + p_y^2 + p_z^2$ and $\Sigma \cdot \mathbf{p} \equiv \sigma_x p_x + \exp(2\pi i/3)\sigma_y p_y + \exp(-2\pi i/3)\sigma_z p_z$.

On the BEC side ($q < 0$), fermions are again fully gapped, while, on the BCS side ($q > 0$), there are eight Fermi points, $\mathbf{p}_a$ ($a = 1, \ldots, 8$), situated at the vertices of a cube in momentum space [1]. The fermionic excitations in the vicinity of these points are left- and right-handed Weyl fermions. In terms of the Cartesian unit vectors ($\hat{\mathbf{x}}$, $\hat{\mathbf{y}}$, $\hat{\mathbf{z}}$), the four Fermi points with right-handed Weyl fermions ($C_a = +1$, for $a = 1, \ldots, 4$) are given by

$$\begin{aligned} \mathbf{p}_1 &= p_F(+\hat{\mathbf{x}} + \hat{\mathbf{y}} + \hat{\mathbf{z}})/\sqrt{3}, \\ \mathbf{p}_2 &= p_F(+\hat{\mathbf{x}} - \hat{\mathbf{y}} - \hat{\mathbf{z}})/\sqrt{3}, \\ \mathbf{p}_3 &= p_F(-\hat{\mathbf{x}} - \hat{\mathbf{y}} + \hat{\mathbf{z}})/\sqrt{3}, \\ \mathbf{p}_4 &= p_F(-\hat{\mathbf{x}} + \hat{\mathbf{y}} - \hat{\mathbf{z}})/\sqrt{3}, \end{aligned} \quad (10)$$

while the four Fermi points with the left-handed Weyl fermions ($C_a = -1$, for $a = 5, \ldots, 8$) have opposite vectors.

Since the quantum phase transition between the BEC and BCS regimes of ultracold fermionic atoms and the quantum phase transition for Dirac fermions with CPT violation are described by the same momentum-space topology, we can expect common properties. An example of such a common property would be the axial or chiral anomaly. For quantum anomalies in (3 + 1)-dimensional systems with Fermi points and their reduction to (2 + 1)-dimensional systems, see, e.g., [3, 20] and references therein.

One manifestation of the anomaly is the topological Wess–Zumino–Novikov–Witten (WZNW) term in the effective action. The general expression for the WZNW term is represented by the following sum over Fermi points (see, for example, Eq. (6a) in [21]):

$$\begin{aligned} S_{\text{WZNW}} &= (12\pi^2)^{-1} \sum_a N_a \\ &\times \int d^3x dt d\tau \mathbf{p}_a \cdot (\partial_\tau \mathbf{p}_a \times \partial_t \mathbf{p}_a). \end{aligned} \quad (11)$$

Here, N_a is the topological charge of the ath Fermi point and $\tau \in [0, 1]$ is an additional coordinate which parametrizes a disc, with the usual spacetime at the boundary $\tau = 1$.

In the Standard Model, Eq. (11) can be seen to give rise to an anomalous Chern–Simons-like action term in the gauge-field sector. Start, for simplicity, from the spectrum of a single electrically charged Dirac fermion (charge e) and again set $c = \hbar = 1$. In the presence of the vector potential $\mathbf{A}$ of a $U(1)$ gauge field, the minimally coupled version of Hamiltonian (6) is

$$H = \begin{pmatrix} \boldsymbol{\sigma} \cdot (\mathbf{p} - e\mathbf{A} - \mathbf{b}) & M \\ M & -\boldsymbol{\sigma} \cdot (\mathbf{p} - e\mathbf{A} + \mathbf{b}) \end{pmatrix}. \quad (12)$$

The positions of the Fermi points for $q \equiv |\mathbf{b}| > M$ are then shifted due to the gauge field,

$$\mathbf{p}_a \equiv \mathbf{p}_a^{(0)} + e\mathbf{A} = \pm \hat{\mathbf{b}}\sqrt{q^2 - M^2} + e\mathbf{A}, \quad (13)$$

with a plus sign for $a = 1$ and a minus sign for $a = 2$. This result follows immediately from Eq. (8) by the minimal substitution $\mathbf{p}_a \longrightarrow \mathbf{p}_a - e\mathbf{A}$, consistent with the gauge principle. For relativistic quantum field theory and with different charges e_a at the different Fermi points, one has the general expression $\mathbf{p}_a = \mathbf{p}_a^{(0)} + e_a\mathbf{A}$.

Next, insert these Fermi points into formula (11) and assume the charges to be τ dependent, so that $\mathbf{p}_a = \mathbf{p}_a^{(0)} + e_a(\tau)\mathbf{A}$. Specifically, we use a parameterization for which the charges $e_a(\tau)$ are zero at the center of the disc, $e_a(0) = 0$, and equal to the physical charges at the boundary of the disc, $e_a(1) = e_a$. From Eq. (11), one then obtains the general form for the Abelian Chern–Simons-like term

$$S_{\text{CS-like}} = (24\pi^2)^{-1} \sum_a N_a e_a^2 \int d^3x dt \mathbf{p}_a^{(0)} \cdot (\mathbf{A} \times \partial_t \mathbf{A}). \quad (14)$$

This result has the "relativistic" form

$$S_{\text{CS-like}} = \int d^4x k_\mu \epsilon^{\mu\nu\rho\sigma} A_\nu(x) \partial_\rho A_\sigma(x), \quad (15)$$

with gauge field $A_\mu(x)$, Levi–Civita symbol $\epsilon^{\mu\nu\rho\sigma}$, and a purely spacelike "vector" k_μ,

$$k_\mu = (0, \mathbf{k}) = \left(0, (24\pi^2)^{-1}\sum_a \mathbf{p}_a^{(0)} e_a^2 N_a\right). \quad (16)$$

Note that only gauge invariance has been assumed in the derivation of Eq. (16). As shown in the Appendix of [13], Chern–Simons vector (16) can be written in the form of a momentum-space topological invariant.

Returning to the case of a single Dirac fermion with charge e and using Eqs. (8) and (16), one finds that the CPT-violating Chern–Simons parameter $\mathbf{k}$ can be expressed in terms of the CPT-violating parameter $\mathbf{b}$ of the fermionic sector,

$$\mathbf{k} = \frac{e^2}{12\pi^2}\theta(q - M)\hat{\mathbf{b}}\sqrt{q^2 - M^2}. \quad (17)$$

This particular contribution to $\mathbf{k}$ comes from the splitting of a marginal Fermi point, which requires $|\mathbf{b}| \equiv q > M$, as indicated by the step function on the right-hand side [$\theta(x) = 0$ for $x \le 0$ and $\theta(x) = 1$ for $x > 0$].

In the context of relativistic quantum field theory, the existence of such a nonanalytic contribution to $\mathbf{k}$ has also been found by Perez-Victoria [22] and Andrianov *et al.* [23] using standard regularization methods, but with a prefactor larger by a factor of 3 and 3/2, respectively. The result (17), on the other hand, is determined by the general topological properties of the Fermi points [13] and applies to nonrelativistic quantum field theory as well. In condensed-matter quantum field theory, the result has been obtained without ambiguity, since the microphysics is known at all scales and regularization occurs naturally.

For the "ferromagnetic" quantum vacuum of Hamiltonian (6), the Chern–Simons vector $\mathbf{k}$ obtained from Eq. (16) by summation over all Fermi points (8) is nonzero and given by Eq. (17). For the "antiferromagnetic" α-phase vacuum of Hamiltonian (9), the vector $\mathbf{k}$ vanishes, because $e_a^2 = 1$ for the fermion charges $e_a = \pm 1$ and $\mathbf{p}_1 + \mathbf{p}_2 + \mathbf{p}_3 + \mathbf{p}_4 = 0$ for the tetrahedron (10). A similar situation may occur for the Standard Model: antiferromagnetic splitting of the Fermi point without induced Chern–Simons-like term [13]. The antiferromagnetic splitting may, however, lead to other observable effects, such as neutrino oscillations [14, 15].

In conclusion, one may expect quantum phase transitions in systems of ultracold fermionic atoms, provided the pairing occurs in the non-*s*-wave channel. The quantum phase transition separates an anomaly-free fully gapped vacuum on the BEC side and a gapless superfluid state on the BCS side, which is characterized by Fermi points and quantum anomalies. This phenomenon is general and may occur in many different systems, including the vacuum of the relativistic quantum field theory relevant to elementary particle physics.

The work of G.E.V. is supported in part by the Russian Foundation for Fundamental Research (grant no. 02-02-16218) and by the Russian Ministry of Education and Science (Leading Scientific School grant no. 2338.2003.2) and the Research Program "Cosmion." This work is also supported by the European Science Foundation COSLAB Program.

REFERENCES

1. G. E. Volovik and L. P. Gorkov, Sov. Phys. JETP **61**, 843 (1985).
2. N. D. Mermin, Rev. Mod. Phys. **51**, 591 (1979).
3. G. E. Volovik, *The Universe in a Helium Droplet* (Clarendon Press, Oxford, 2003).
4. D. Vollhardt and P. Wölfle, *The Superfluid Phases of Helium 3* (Taylor and Francis, London, 1990).
5. C. A. Regal, M. Greiner, and D. S. Jin, Phys. Rev. Lett. **92**, 040403 (2004); cond-mat/0401554.
6. M. Greiner, C. A. Regal, and D. S. Jin, Nature **426**, 537 (2003); cond-mat/0311172.
7. M. W. Zwierlein, C. A. Stan, C. H. Schunck, *et al.*, Phys. Rev. Lett. **92**, 120403 (2004); cond-mat/0403049.
8. J. Kinast, S. L. Hemmer, M. E. Gehm, *et al.*, Phys. Rev. Lett. **92**, 150402 (2004); cond-mat/0403540.
9. M. Bartenstein, A. Altmeyer, S. Riedl, *et al.*, Phys. Rev. Lett. **92**, 120401 (2004); cond-mat/0401109.
10. J. Zhang, E. G. M. van Kempen, T. Bourdel, *et al.*, quant-ph/0406085.
11. C. H. Schunck, M. W. Zwierlein, C. A. Stan, *et al.*, cond-mat/0407373.
12. S. Weinberg, Phys. Rev. Lett. **19**, 1264 (1967); A. Salam, in *Elementary Particle Theory*, Ed. by N. Svartholm (Almqvist, Stockholm, 1968), p. 367; S. L. Glashow, J. Iliopoulos, and L. Maiani, Phys. Rev. D **2**, 1285 (1970); C. Bouchiat, J. Iliopoulos, and P. Meyer, Phys. Lett. B **38**, 519 (1972); D. J. Gross and R. Jackiw, Phys. Rev. D **6**, 477 (1972).
13. F. R. Klinkhamer and G. E. Volovik, hep-th/0403037.
14. F. R. Klinkhamer, JETP Lett. **79**, 451 (2004); hep-ph/0403285.
15. F. R. Klinkhamer, hep-ph/0407200.
16. S. M. Carroll, G. B. Field, and R. Jackiw, Phys. Rev. D **41**, 1231 (1990).
17. C. Adam and F. R. Klinkhamer, Nucl. Phys. B **607**, 247 (2001); hep-ph/0101087.
18. M. Perez-Victoria, J. High Energy Phys. **0104**, 032 (2001); hep-th/0102021.
19. R. Lehnert, J. Math. Phys. **45**, 3399 (2004); hep-ph/0401084.
20. M. Stone and R. Roy, Phys. Rev. B **69**, 184511 (2004); cond-mat/0308034.
21. G. E. Volovik and V. A. Konyshev, JETP Lett. **47**, 250 (1988).
22. M. Perez-Victoria, Phys. Rev. Lett. **83**, 2518 (1999); hep-th/9905061.
23. A. A. Andrianov, P. Giacconi, and R. Soldati, J. High Energy Phys. **0202**, 030 (2002); hep-th/0110279.

JETP Letters, Vol. 80, No. 5, 2004, pp. 348–350. Translated from Pis'ma v Zhurnal Éksperimental'noĭ i Teoreticheskoĭ Fiziki, Vol. 80, No. 5, 2004, pp. 395–397.

Iron at High Negative Pressures

S. V. Razorenov*, G. I. Kanel, and V. E. Fortov

Institute of Problems of Chemical Physics, Chernogolovka Branch, Russian Academy of Sciences, Chernogolovka, Moscow region, 142432 Russia

Institute of High Energy Densities, Russian Academy of Sciences, Moscow, 125412 Russia

**e-mail: razsv@ficp.ac.ru*

Received July 23, 2004

With the object of verifying the presence of a region of anomalous iron compressibility at negative pressures, as predicted by the *ab initio* calculations, the reflection of compression pulses from the surfaces of iron single crystals was detected. No evidence of the expected formation of rarefaction shock waves was observed in the range of attained tensile stresses up to 7.6 GPa. The breaking stresses achieved 25–50% of the theoretical iron ultimate strength for a load duration of ~10^{-8} s. The dependence of breaking strength on the extension rate did not reveal any singularities in the region of assumed anomaly in iron compressibility. © *2004 MAIK "Nauka/Interperiodica".*

PACS numbers: 62.20.Mk; 62.50.+p; 64.30.+t

The modern technique used in the experiments with shock waves allows the properties of materials to be studied at negative pressures down to –15…–20 GPa and lower [1–3]. In this case, the analysis of the states of a substance in the tension region is based only on the fundamental conservation laws with the extrapolation of the data on the equations of state at large compressions. At present, the *ab initio* calculations provide a more reliable and objective estimate of the equation of state for a substance at high (up to the spinodal) negative pressures. For example, the aluminum zero isotherm was calculated in [4] using the density functional theory with the generalized gradient corrections. It has no singularities and has a minimum at a pressure of –11.2 GPa. The extrapolation of the aluminum Hugoniot curve gives the close value of –13.4 GPa for the pressure at the minimum. First attempts at measuring the compressibility at negative pressures have been undertaken for solids [5] and liquids [6], but the applicability range of the suggested methods is as yet limited.

Recent *ab initio* calculations of the iron zero isotherm [7] have revealed its anomalous behavior in the negative pressure range. The computational results shown in Fig. 1 demonstrate the jump in volume caused by the rearrangement of the crystal energy spectrum at a pressure of –3.4 GPa and the presence of a minimum at –13.4 GPa. The extrapolation of the α-iron [8] Hugoniot curve gives a minimum at –31.6 GPa, which differs by 2.3 times from the *ab initio* results.

The presence of a region of anomalous compressibility in the vicinity of –3.4 GPa should give rise to the shocks upon the propagation of expansion waves in iron, thereby providing the possibility of experimental verification of the existence of such an anomaly. For this purpose, a set of experiments was carried out, and the corresponding results are presented in this work.

The tensile stresses (negative pressures) were produced in the plane iron samples upon the reflection of submicrosecond one-dimensional compression pulses from the sample surfaces. A 0.8-mm-thick iron sheet of 99.98% purity contained arbitrarily oriented grains with transverse sizes up to 5–8 mm. The samples 0.2–0.75 mm thick and 12–15 mm in diameter were cut in such a way that they contained one coarse grain in the central region. This precluded the premature initiation of the destruction at the intergrain boundaries in the

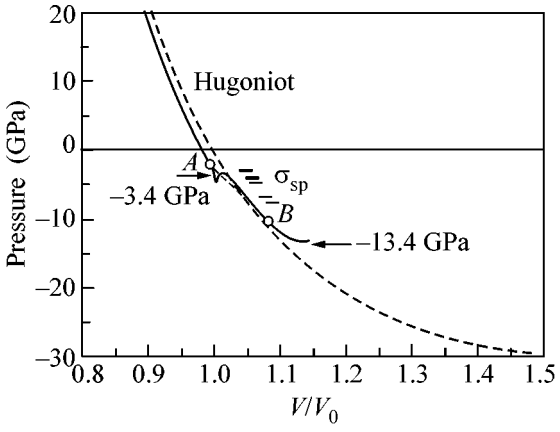

Fig. 1. The calculated [7] zero isotherm (solid line) and the extrapolated Hugoniot adiabate of α iron (dashed line). V_0 is the specific volume at 293 K and zero pressure. Dashes indicate the measured destructing stresses (spall strength) in iron for various shock-loading durations. *AB* is the region of anomalous compressibility, where one expects the formation of the rarefaction shock wave.

0021-3640/04/8005-0348$26.00 © 2004 MAIK "Nauka/Interperiodica"

controlled central region of the sample. The compression pulses were generated by the impact of an aluminum plate that was accelerated using an explosive device [3]. The thickness of the impactor was varied from 50 to 400 μm; the impact velocity was equal to 650 ± 50 or 1200 ± 50 m/s. In the experiments, the velocity u_{fs} of the free rear surface of the sample was measured as a function of time t. Measurements were carried out using a Doppler laser velocimeter VISAR [3, 8] with a time resolution of 0.4 ns.

Examples of the velocity profiles measured for the free sample surfaces are shown in Fig. 2 for two impact load durations differing by a factor of ten. One can see that the elastoplastic compression wave and a portion of the ensuing expansion wave emerge at the surface wave profiles. After the reflection of the compression pulse from the free surface, the tensile stresses are generated inside the sample to initiate its destruction (spalling). This is accompanied by the relaxation of tensile stresses and formation of a compression wave (spall pulse), whose emergence at the surface causes the second increase in the surface velocity. Under the given loading conditions, the damping of the surface velocity upon its decrease from the maximum to the value ahead of the front of the spall pulse is proportional to the breaking stress. The subsequent surface-velocity oscillations are caused by the multiple wave reflections inside the spalled layer of the sample between its rear and breaking surfaces.

On the whole, the free-surface velocity profiles measured for the iron samples were similar to those obtained for other metals [3] and gave no evidence of the formation of rarefaction shocks. An analysis of the wave profiles allows the breaking stresses (spall strength) to be determined with a high accuracy. The spall strength σ_{sp} was calculated on the basis of the analysis of the interaction between the incident and reflected waves [3, 9]. It was defined as a decrease in the surface velocity Δu_{fs} from its maximum value to the value ahead of the front of the spall pulse. In the acoustic approximation,

$$\sigma_{sp} = \frac{1}{2}\rho_0 c_b(\Delta u_{fs} + \delta),$$

where ρ_0 is the density of a material, δ is the correction for the velocity-profile distortion due to a difference between the velocity (c_l) of the spall-pulse front propagating over the stretched material and the velocity (c_b) of the plastic portion of the incident unloading wave ahead of it. In this work, the breaking stresses were determined with allowance for the nonlinear compressibility of a material [3], for which reason its equation of state was extrapolated to the tension region. The corresponding negative breaking pressures differ from σ_{sp} by 2/3 of the yield stress. The difference between the breaking pressure and stress did not exceed 10%.

The measurement results are summarized in Fig. 3 in the form of a dependence of the iron spall strength on the extension rate $\dot{V}/V_0$ in the incident shock-load pulse, calculated as

$$\dot{V}/V_0 = \dot{u}_1/2c_b,$$

where $\dot{u}_1$ is the measured free-surface velocity gradient in the unloading portion of the incident compression pulse. In actuality, these values of the deformation rates are equal, except for a constant factor on the order of few units, to the growth rate of a discontinuity volume in the material at the initial stage of its spall breaking [3].

With an increase in the extension rate from ~10^5 to ~5×10^6 s^{-1}, the breaking strength increases from 2.9 to

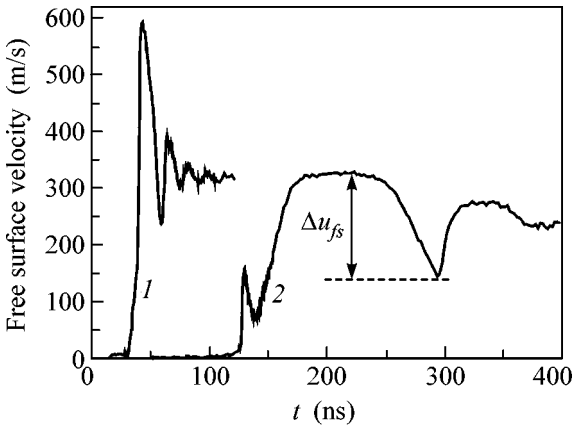

Fig. 2. Free-surface velocity profiles of high-purity iron plates of thicknesses (*1*) 0.19 and (*2*) 0.77 mm after the impact by the 0.05- and 0.04-mm-thick aluminum plates with velocities of 1200 and 650 m/s, respectively.

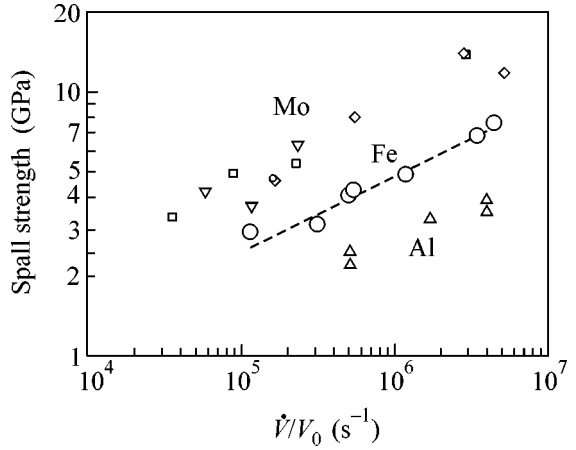

Fig. 3. Dependence of the spall strength on the deformation rate. Dashes correspond to the approximation $\sigma_{sp} = 0.89(\dot{V}/V_0)^{0.29}$. The results of analogous measurements for molybdenum single crystals with different orientations [1] and aluminum [2] are given for comparison.

7.6 GPa, and the spall thickness decreases from –400 to 40 μm. In this range, the measurement results can be approximated by the function $\sigma_{sp} = 0.89(\dot{V}/V_0)^{0.29}$ GPa, shown by dashes in Fig. 3. The comparison with similar data on the molybdenum [1] and aluminum [2] single crystals demonstrates the similarity of the spall-strength dependences on the extension rate and does not reveal any singularities in the region of the presumed anomaly in the iron compressibility.

One can see in Fig. 1 that the range of attained tensile stresses fully covers the anomaly region on the calculated iron zero isotherm. Inasmuch as the topological electronic transitions [7] should be virtually inertialess, it seems improbable that the compressibility associated with these transitions does not reveal itself because of a short duration of the action of negative pressures. At the same time, the electronic structure of iron crystals was calculated in [7] for 0 K, whereas the experiments presented in this work were performed at room temperature. It is conceivable that the anomaly of iron compressibility occurs only at low temperatures and disappears with heating. In this case, the instability of crystal structure may be one of the factors that are responsible for the cold-iron brittleness phenomenon.

The spinodal position in the condensed phase of a substance determines the theoretical ultimate or "ideal" tensile strength of a material. If the iron 0 K isotherm really has a minimum at –13.4 GPa, as follows from the *ab initio* calculations [7], then, according to the measurements, ~55% of the iron ultimate strength is realized during $\sim 10^{-8}$ s of the action of tensile stresses. At the same time, a comparison of the maximal measured spall breaking strength with the estimated ultimate strength via extrapolating the Hugoniot adiabate suggests that ~24% of iron ideal strength was realized in our experiments. Similar estimates for molybdenum [1] and aluminum [2] gave 25 and 29%, respectively.

Thus, our room-temperature shock-wave experiments have not confirmed the existence of a compressibility anomaly for iron in the negative pressure range, as was predicted by the *ab initio* calculations. We intend to continue our experimental study at low temperatures. For a shock load of a duration of $\sim 10^{-8}$ s, the breaking stresses are comparable with the theoretical iron ultimate strength.

We are grateful to G.V. Sin'ko and N.A. Smirnov for proving the *ab initio* results on iron compressibility before their publication. This work was supported by the Russian Foundation for Basic Research (project no. 03-02-16379) and the program for basic research of the Presidium of the Russian Academy of Sciences "Thermal Physics and Mechanics of Intense Energetic Actions."

REFERENCES

1. G. I. Kanel, S. V. Razorenov, A. V. Utkin, *et al.*, J. Appl. Phys. **74**, 7162 (1993).
2. G. I. Kanel, S. V. Razorenov, K. Baumung, *et al.*, J. Appl. Phys. **90**, 136 (2001).
3. T. Antoun, L. Seaman, D. R. Curran, G. I. Kanel, S. V. Razorenov, and A. V. Utkin, *Spall Fracture* (Springer, New York, 2003).
4. G. V. Sin'ko and N. A. Smirnov, Pis'ma Zh. Éksp. Teor. Fiz. **75**, 217 (2002) [JETP Lett. **75**, 184 (2002)].
5. G. S. Bezruchko, G. I. Kanel', and S. V. Razorenov, Teplofiz. Vys. Temp. **42**, 262 (2004) [High Temp. **42**, 234 (2004)].
6. A. D. Alvarenga, M. Grimsditch, and R. J. Bodnar, J. Chem. Phys. **98**, 8392 (1993).
7. G. V. Sin'ko and N. A. Smirnov, Pis'ma Zh. Éksp. Teor. Fiz. **79**, 665 (2004) [JETP Lett. **79**, 537 (2004)].
8. L. M. Barker and R. E. Hollenbach, J. Appl. Phys. **45**, 4872 (1974).
9. G. I. Kanel', Prikl. Mekh. Tekh. Fiz. **42**, 194 (2001).

Translated by V. Sakun

JETP Letters, Vol. 80, No. 5, 2004, pp. 351–354. Translated from Pis'ma v Zhurnal Éksperimental'noĭ i Teoreticheskoĭ Fiziki, Vol. 80, No. 5, 2004, pp. 398–402.

Modification of the Energy Spectrum and Magnetic Breakdown in a System of 2D Holes at the GaAs/$Al_{0.5}Ga_{0.5}As$ Heterojunction upon Uniaxial Compression

W. Kraak[1], A. M. Savin[2], N. Ya. Minina[3,*], A. A. Il'evskii[3], and A. V. Polyanskii[3]

[1] *Institute of Physics, Humboldt University, D-12489 Berlin, Germany*

[2] *Laboratory of Low Temperatures, Technological University of Helsinki, P.O.B. 2200, FIN-02015 HUT, Finland*

[3] *Faculty of Physics, Moscow State University, Vorob'evy gory, Moscow, 119992 Russia*

**e-mail: min@mig.phys.msu.ru*

Received July 14, 2004; in final form, July 26, 2004

Uniaxial compression of the *p*-type GaAs/$Al_{0.5}Ga_{0.5}As$ heterostructures induces magnetic breakdown between the spin-split ground-state subbands of two-dimensional heavy holes. This phenomenon serves as direct experimental evidence of a strong qualitative modification of the energy spectrum of these structures upon uniaxial deformation. This modification has been revealed by numerical calculations, and, according to it, the subband spin splitting decreases upon compression, while the contours of the hole Fermi surface in both subbands touch one another in the compression direction in a pressure range of 2.5 kbar. © *2004 MAIK "Nauka/Interperiodica".*

PACS numbers: 73.21.Fg; 73.40.Kp

Magnetic breakdown is one of the phenomena that most clearly demonstrate the quantum nature of charge-carrier motion in solids and represents the electron (hole) tunneling in a magnetic field through the classically forbidden regions of momentum space at the sites of close approach of the electron (hole) orbits. Since its discovery, it has been studied both as a fundamental phenomenon and as a tool for revealing the special features of the carrier energy spectra in metals and semiconductors. For instance, a change in the isoenergy surface connectivity accompanied by the intraband magnetic breakdown observed in single-crystal $Bi_{1-x}Sb_x$ alloys upon uniaxial compression [1] allowed one to unambiguously establish the presence of a saddle point in the energy spectrum of the $Bi_{1-x}Sb_x$ alloys with $x \geq 0.2$. In this work, the development of magnetic breakdown is observed in a system of two-dimensional (2D) holes at the *p*-GaAs/$Al_{0.5}Ga_{0.5}As$ heterojunction upon uniaxial compression. This phenomenon is direct experimental evidence of the compression-induced Fermi-surface (FS) modification in these structures that was revealed in our previous work [2]. The calculations in [2] and the experimental study in this work were performed for heterostructures with the same configuration, layer sequence, and carrier concentration in a quantum well (QW).

The *p*-type GaAs/$Al_{0.5}Ga_{0.5}As$ structures were grown from molecular beam epitaxy at the Niels Bohr Institute, University of Copenhagen, on a GaAs substrate in the [001] direction with the following layer sequence: a 1-μm pure GaAs; a 70-Å undoped $Al_{0.5}Ga_{0.5}As$ spacer; a 500-Å active layer of Be-doped (5×10^{17} cm^{-3}) $Al_{0.5}Ga_{0.5}As$; and a 50-Å capping layer of Be-doped (1×10^{18} cm^{-3}) GaAs. Samples with sizes $3.0 \times 0.8 \times 0.5$ mm were split off from a disk along the natural glide planes with the long side directed along [110], and a mesa in the Hall configuration was etched in the central part of the sample. The termination pads were formed by the diffusion of the Au:Zn alloy, and 20-μm gold wires were sealed to them by the ultrasound method. The quantum Shubnikov–de Haas (SdH) oscillations, whose frequency determines the 2D-hole cross sections and the corresponding concentrations, were studied at a temperature of 1.5 K in magnetic fields up to 6 T. The total hole concentration was also determined from the Hall effect and found to be $N_s = 7.6 \times 10^{11}$ cm^{-2} at normal pressure $P = 0$.

The uniaxial compression was performed in a complex system [3, 4] consisting of an elastic ring made from a nonmagnetic 40KhNYu steel and a rectangular sample rigidly fixed in it by low-temperature epoxy resin (Fig. 1). The ring converts the stretching force applied along the *z* axis into the compressive force along the *y* axis (along the sample). The stretching force is applied to the ring at liquid helium temperatures using a special device and is determined from the elongation of a calibrated steel spring comprising a part of this device. The advantages of this method are as follows: (1) a rigid fixation of the sample carefully adjusted to the ring allows one to circumvent the requirement that its end faces be strictly plane-parallel, which is necessary in the traditional methods of com-

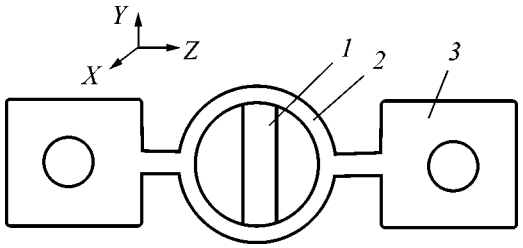

Fig. 1. Elastic element converting tension into uniaxial compression of the sample: (*1*) sample, (*2*) ring, (*3*) "ears" for the fixation in the stretching device.

pression in anvils; and (2) the central symmetry of a load applied to the sample removes the requirement that the sample axis in anvils be strictly oriented along the compressive force, since otherwise only a small deviation from this orientation leads to premature sample destruction. In this work, uniaxial compression up to 5 kbar was performed along the sample length in the [110] direction.

According to the calculation of the energy spectrum, only the ground state of heavy holes is occupied in the *p*-GaAs/$Al_{0.5}Ga_{0.5}As$ heterostructures with the indicated geometry and carrier concentration [2]. Because of the lack of inversion symmetry in a triangular QW at a single heterojunction, this state is split into two spin-nondegenerate subbands. The dispersion law for such subbands is strongly nonparabolic, and the spin splitting at the Fermi level is ε_g = 2.14 meV in the [110] direction and ε_g = 1.65 meV in the [100] direction. After applying uniaxial compression, the spin splitting of the subbands is reduced [2], and the Fermi surface (FS) undergoes strong qualitative transformation for both subbands (Fig. 2). The 2D FS contours for subband 0 with a higher effective mass and for "light" subband 1 (the corresponding FS sections are S_0 and S_1) transform in the momentum space into elongated ellipses that touch one another in the compression direction [110] at the critical pressure P_{cr} = 2.5 kbar. The energy gap between the subbands ε_g = 0 in this direction remains very small in the vicinity of P_{cr}. A further buildup of pressure to 5 kbar removes the degeneracy at the Fermi level in the [110] direction, although the proximity of the S_0 and S_1 orbits in this direction still plays a large role.

The SdH oscillation frequencies F_0 and F_1 are proportional to the FS sections in the spin subbands S_0 and S_1, and the corresponding hole concentrations are $n_0 = eF_0/hc$ and $n_1 = eF_1/hc$. The experimental dependence of these parameters on the uniaxial compression is shown in Fig. 3. Whereas the frequencies F_1 in light subband 1 can be calculated directly from the oscillatory dependences at low magnetic fields, the frequencies F_0 for heavy subband 0 are determined from the Fourier spectra of magnetoresistance oscillations (Fig. 4). The concentration n_0 can also be determined as $n_0 = N_h - n_1$, where N_h is the total hole concentration determined from the Hall effect. Against the background of an overall decrease in the total concentration of 2D holes in the QW, the carriers are rearranged among the spin subbands, as a result of which n_0 decreases and n_1 increases (Fig. 3). This result is in agreement with our previous data obtained in [5] for the *p*-GaAs/$Al_{0.5}Ga_{0.5}As$ heterostructures with a higher hole concentration. The spectral composition of the quantum SdH oscillations is rather simple at P = 0 and becomes more complicated under uniaxial compression, as can be seen both directly from the magnetic-field dependences of magnetoresistance oscillations (Fig. 4b) and from the corresponding Fourier spectra (Fig. 4a).

Before proceeding to the analysis, it is worth noting that the smallness of the subband spin splitting ε_g in the structures studied hampers the observation of the tran-

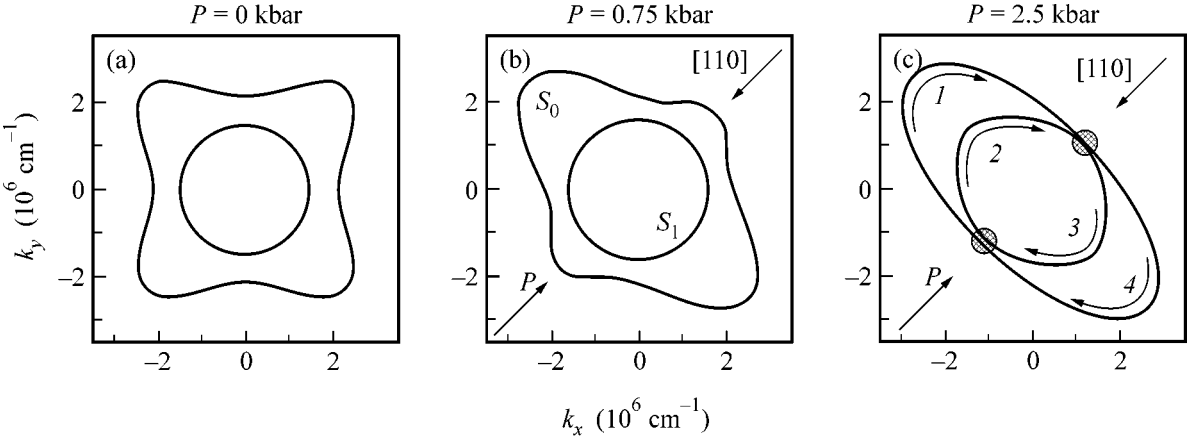

Fig. 2. The FS contours S_0 and S_1 in two spin-split subbands of 2D heavy holes at different pressures along the [110] direction. For P = 2.5 kbar, the magnetic-breakdown regions are hatched, and the numerals *1*, *2*, *3*, and *4* correspond to the different segments of the magnetic-breakdown orbits.

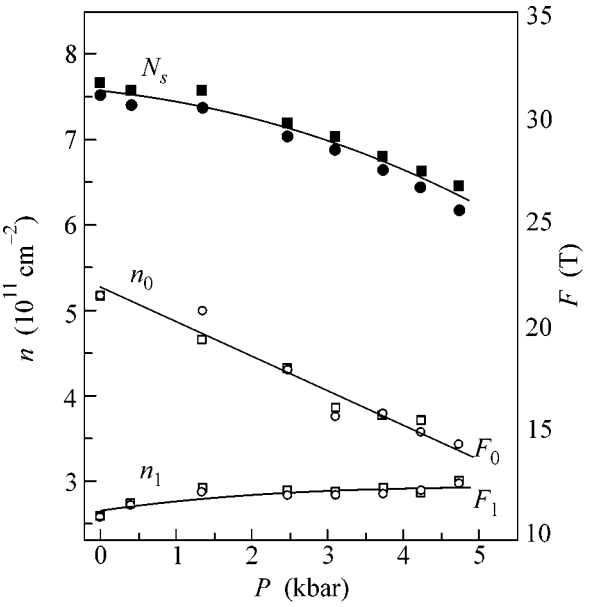

Fig. 3. Dependences of the (left scale) concentration and the (right scale) SdH frequency on the uniaxial compression: N_s is the total hole concentration in the QW; n_0 and n_1 are the concentrations in the spin-split subbands 0 and 1, respectively. Different symbols correspond to different samples.

sition from the weak-field regime, where the interband magnetic breakdown is absent, to the strong-field regime, where it occurs and, in the available magnetic fields of 6 T, can be observed in our samples even in the absence of uniaxial compression. The breakdown field is $H_B \approx \varepsilon_g^2/\varepsilon_F\mu$, where $\mu = e\hbar/m^*c$, and the breakdown probability is $W = e^{-H_B/H}$ [6], so that, according to estimates, the magnetic breakdown can occur with the probability $W = 0.4$ even in fields $H \geq H_B \approx 3$–4 T. In Fig. 5, the Fourier transforms of the SdH oscillations at $P = 0$ are shown in various magnetic-field ranges. At fields below 4 T, only a single frequency F_1 corresponding to the S_1 section for holes with the smallest effective mass $m_1^* = 0.22m_0$ [2] is, in effect, present in the Fourier spectrum, whereas the amplitude of oscillations with frequency F_0 (section S_0 for the holes with mass $m_1^* \sim 0.9m_0$) is still small in this range of magnetic fields, and the corresponding peak is hardly visible. However, at $H > 4$ T, both fundamental frequencies F_1 and F_0, as well as their sum $F_0 + F_1$ suggesting the nonzero probability of magnetic breakdown between the subbands, are seen in the Fourier spectrum in Fig. 5. The fact that all Fourier spectra in Fig. 4a correspond to

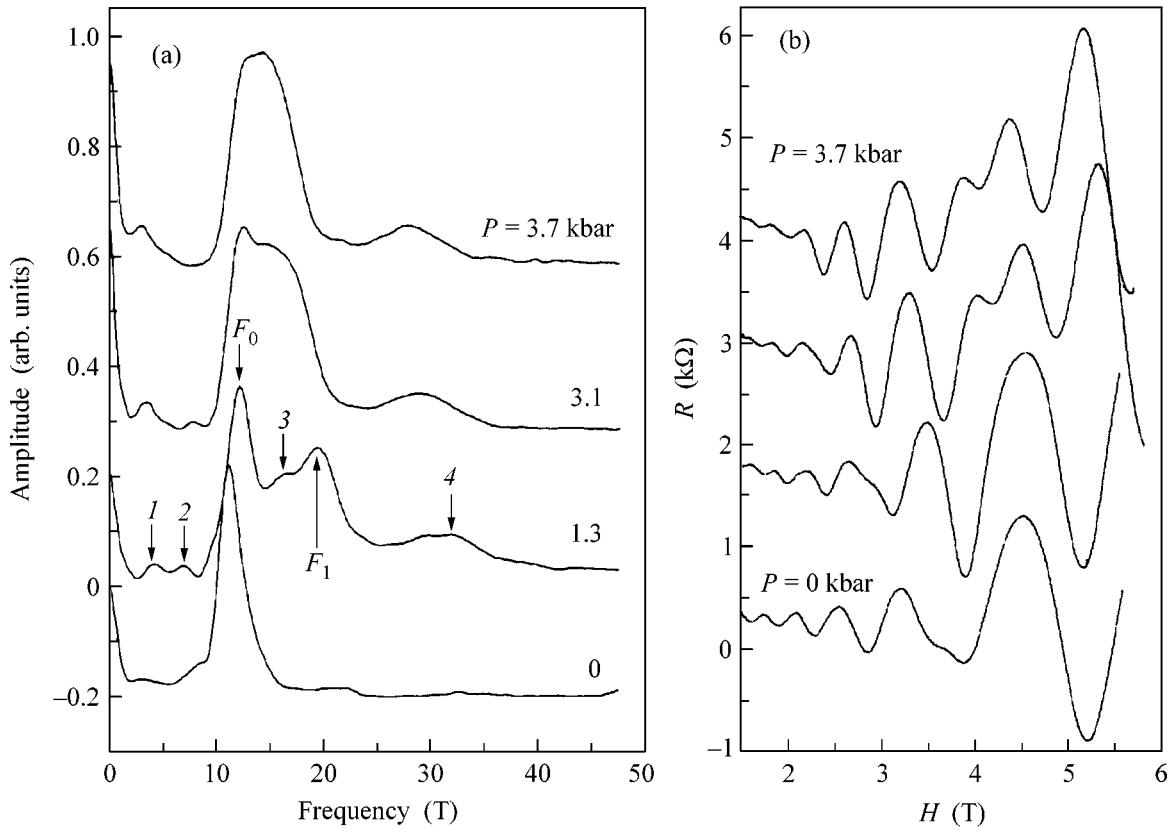

Fig. 4. (a) Fourier spectra and (b) the corresponding SdH quantum oscillations for different uniaxial compressions. F_0 and F_1 are the fundamental frequencies. The magnetic-breakdown frequencies are numbered for $P = 1.3$ kbar: (*1*) $(F_0 - F_1)/2$, (*2*) $(F_0 + F_1)/4$, (*3*) $(F_0 + F_1)/2$, and (*4*) $F_0 + F_1$.

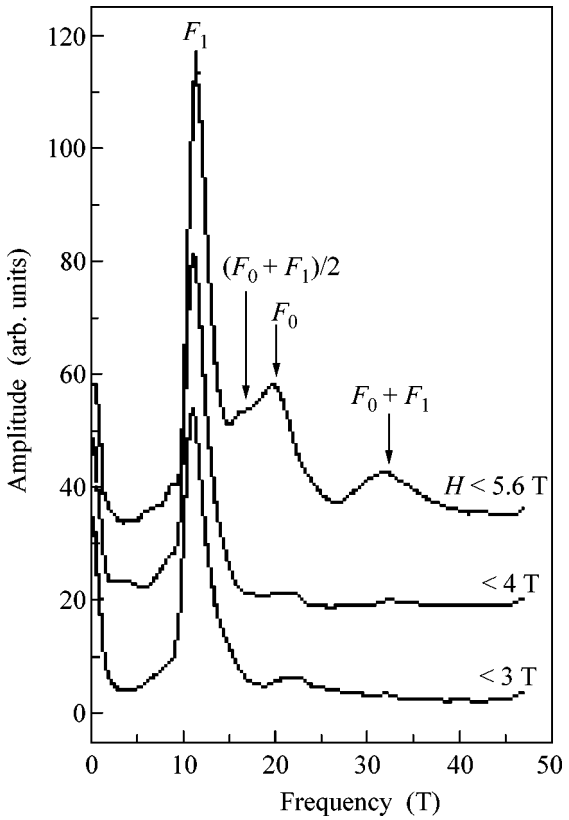

Fig. 5. Fourier spectra of the SdH oscillations for different regions of magnetic field in the absence of compression.

the Fourier transforms of the SdH oscillations in magnetic fields $H < 4$ T (Fig. 4b) counts in favor of the unambiguous interpretation of the magnetic breakdown as a consequence of the uniaxial compression.

At $P \geq 1.3$ kbar (Fig. 4a), the Fourier spectra become more complicated because of a change in the FS of 2D holes upon uniaxial compression (Fig. 2). The possibility of transition from one quasi-classical orbit to the other under the magnetic-breakdown condition affects the dynamics of charge-carrier motion, and, for the FS depicted in Fig. 2c, orbits *1–3* and *2–4* ($(F_0 + F_1)/2$ frequency and its $F_0 + F_1$ harmonic, respectively) appear, apart from the classical orbits consisting of the *1–4* (S_0 section; F_0 frequency) and *2–3* (S_1 section; F_1 frequency) segments. In this case, the fundamental frequencies F_0 and F_1, according to the data in Fig. 3, approach each other under pressure, as do also the conditions for their observation, so that these frequencies are not resolved in the Fourier spectra at the maximal pressures. Of greatest interest, from the viewpoint of the theory of magnetic breakdown, is the appearance of the difference frequency $(F_0 - F_1)/2$ that can be related to the areas of "segments" *1–2* and *3–4* in Fig. 2c. Such orbits are not allowed in the quasi-classical picture of magnetic breakdown, while the corresponding difference frequencies are the result of quantum interference and are not associated with the oscillations of the charge-carrier density of states. If the magnetic breakdown is phase-coherent, the magnetic-breakdown-paired trajectories (of types *1–2* in Fig. 2c) going in the same direction represent a specific "quantum interferometer" whose base is formed by the sections between the trajectories [6]. Such different interference frequencies were previously observed while studying the magnetic breakdown both in three-dimensional materials (e.g., niobium [7]) and, recently, in 2D organic conductors [8].

In closing, we note that the magnetic breakdown is developed upon uniaxial compression between two FSs belonging to different spin-split subbands of the heavy-hole ground state in a system of 2D holes in an asymmetrical triangular QW at the $GaAs/Al_{0.5}Ga_{0.5}As$ heterojunction. The complication of the Fourier spectra of SdH quantum oscillations under pressure serves as an indicator of the magnetic breakdown. Apart from the fundamental frequencies characterizing the real FS sections in the momentum space, the combination and difference frequencies and their harmonics appear in the spectra. The observed phenomenon is direct experimental evidence of the strong anisotropic modification of the 2D-hole FS upon uniaxial compression, as was predicted previously by the numerical calculations. According to the calculation, the subband spin splitting at the Fermi level decreases to zero in the uniaxial compression direction at $P_c = 2.5$ kbar, which serves as a basis for the development of the interband magnetic breakdown.

We are grateful to K.B. Sorensen for growing the structures and sample preparation and to O.P. Hansen for assistance. This work was supported by the Russian Foundation for Basic Research (project no. 04-02-16861) and Scientific Schools (project no. 1786.2003.2).

REFERENCES

1. N. B. Brandt, M. Yu. Lavrenyuk, N. Ya. Minina, and A. M. Savin, Zh. Éksp. Teor. Fiz. **94** (6), 235 (1988) [Sov. Phys. JETP **67**, 1220 (1988)].
2. K. J. Kolokolov, A. M. Savin, S. D. Beneslavski, *et al.*, Phys. Rev. B **59**, 7537 (1999).
3. N. B. Brandt, V. S. Egorov, M. Yu. Lavrenyuk, *et al.*, Sov. Phys. JETP **62**, 1303 (1985).
4. N. B. Brandt, N. Ya. Minina, M. Yu. Lavrenyuk, and A. M. Savin, Inventor's Certificate No. 1259138; Otkrytiya, Izobret., No. 35 (1986).
5. O. P. Hansen, J. S. Olsen, W. Kraak, *et al.*, Phys. Rev. B **54**, 1533 (1996).
6. *The Conduction Electrons*, Ed. by M. I. Kaganov and V. S. Édel'man (Nauka, Moscow, 1985) [in Russian].
7. N. E. Alekseevskiĭ, K.-H. Bergel, V. I. Nizhankovskiĭ, *et al.*, Zh. Éksp. Teor. Fiz. **73**, 700 (1977) [Sov. Phys. JETP **46**, 366 (1977)].
8. Ju. H. Kim, S. Y. Han, and J. S. Brooks, Phys. Rev. B **60**, 3213 (1999).

Translated by V. Sakun

JETP Letters, Vol. 80, No. 5, 2004, pp. 355–358. From Pis'ma v Zhurnal Éksperimental'noĭ i Teoreticheskoĭ Fiziki, Vol. 80, No. 5, 2004, pp. 403–407.

Dynamics of Cubic–Tetragonal Phase Transition in $KNbO_3$ Perovskite¶

S. N. Gvasaliya[1, 2], B. Roessli[1], R. A. Cowley[3], S. G. Lushnikov[2], A. Choubey[4], and P. Günter[4]

[1] *Laboratory for Neutron Scattering, ETHZ & Paul Scherrer Institut, CH-5232, Villigen, PSI, Switzerland*
[2] *Ioffe Physicotechnical Institute, St. Petersburg, 194021 Russia*
[3] *Clarendon Laboratory, Oxford University, Parks Road, Oxford OX1 3PU, UK*
[4] *Nonlinear Optics Laboratory, ETH Hönggerberg, CH-8093, Zürich, Switzerland*

Received July 27, 2004

The low-energy part of the vibration spectrum of $KNbO_3$ was studied by cold neutron inelastic scattering in the cubic phase. In addition to acoustic phonons, we observe strong diffuse scattering, which consists of two components. The first one is quasistatic and has a temperature-independent intensity. The second component appears as quasielastic scattering in the neutron spectrum, indicating a dynamic origin. From analysis of the inelastic data, we conclude that the quasielastic component and the acoustic phonon are mutually coupled. The susceptibility associated with the quasielastic component grows as the temperature approaches T_C. © *2004 MAIK "Nauka/Interperiodica".*

PACS numbers: 61.12.-q; 63.50.+x; 64.60.-i; 77.80.-e

ABO_3 perovskites form a class of important materials, in part because of potential technical applications but also due to fundamental interest in the physics of phase transitions [1, 2]. At sufficiently high temperatures, many of these perovskites have O_h^1 cubic symmetry, and structural phase transitions can take place as the temperature is lowered. Well-known examples are, e.g., the cubic–tetragonal phase transition in $SrTiO_3$ ($T_C \approx 105$ K) or in $BaTiO_3$ ($T_C \approx 425$ K) (for a review, see [3]). There are, however, ABO_3 perovskites, which have been less studied. An example is the first-order cubic–tetragonal phase transition in $KNbO_3$ which occurs at $T_C \approx 683$ K when cooling the crystal from above the transition temperature [4].

The mechanism of the cubic–tetragonal (C–T) phase transition in $KNbO_3$ is still controversial. Whereas well-defined soft phonon modes with frequency varying with temperature have been detected in many materials close to T_C [1–3], only an overdamped excitation has been observed in cubic $KNbO_3$ with neutron scattering, and it has been suggested that the nature of the C–T phase transition in that compound is similar to the displacive C–T transition in $BaTiO_3$ [5, 6]. On the other hand, two coexisting and essentially uncoupled modes are inferred from analysis of optical data in the cubic phase of $KNbO_3$: a relaxation mode and a soft phonon, with the relaxation process driving the C–T phase transition [7].

We reinvestigated the low-energy part of the vibration spectrum in $KNbO_3$ under improved resolution conditions, first, to try to elucidate the mechanism of the phase transition in this crystal and, second, to check whether the diffuse scattering found in [8] is of static or dynamic origin. The inelastic cold-neutron scattering measurements reported here were performed with the three-axis TASP spectrometer located at the neutron spallation source SINQ (Paul Scherrer Institute, Switzerland). A large single crystal of $KNbO_3$ (~20 cm^3, mosaic ~80′) was mounted into an ILL-type furnace. To decrease the level of incoherent background, the sample holder was made from pure niobium. The crystal was aligned in the (*hk*0) scattering plane. The measurements were performed in the temperature range 727–1030 K. The (002) reflection of pyrolytic graphite (PG) was used to monochromate and analyze the incident and scattered neutron beams, respectively. The spectrometer was operated in the constant final-energy mode with $k_f = 1.97$ Å^{-1}. A PG filter was used to remove higher-order wavelengths. The horizontal collimation was 10′/Å–80′–80′–80′. With that configuration, the energy resolution at zero-energy transfer is ~0.4 meV. By monitoring the position and intensity of the (1, 1, 0) Bragg peak, the temperature of the cubic–tetragonal phase transition upon cooling was found at $T_C = 684 \pm 2$ K, in close agreement with published data [4, 6]. The temperature of the sample was controlled by two thermocouples. The temperature gradient through the sample did not exceed 15 K.

¶ This article was submitted by the authors in English.

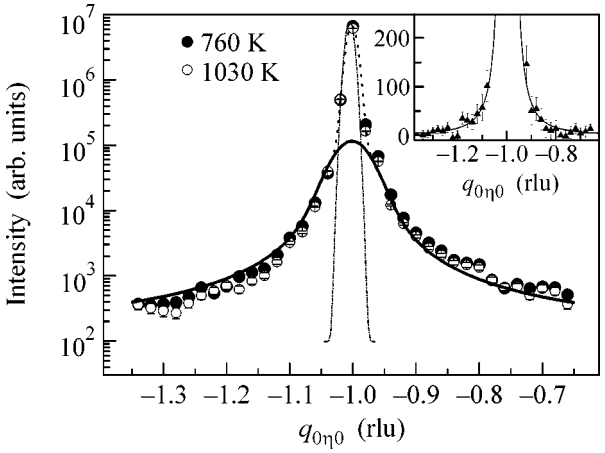

Fig. 1. Profiles of elastic scans in the (0η0) direction at T = 760 and 1030 K. Raw data are shown by circles. The dotted line is the result of fits as described in the text. The bold line shows the Lorentzian profile. The dash-dotted line stands for the intense and narrow Bragg peak. The intensity is given in a logarithmic scale. The insert shows the difference of the elastic scans $I(T = 760\ \text{K}) - I(T = 1030\ \text{K})$ fitted with Eq. (1). 1 rlu corresponds to 1.57 Å^{-1}.

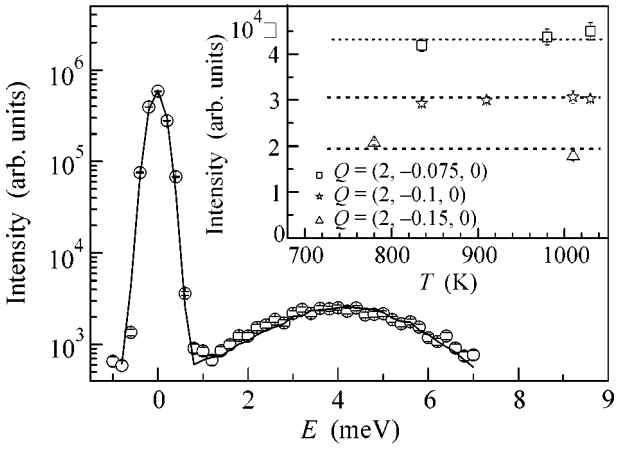

Fig. 2. Neutron scattering spectrum from $KNbO_3$ at 1030 K. Raw data are shown by open circles. The solid line is the result of fit as described in the text. The intensity is given in a logarithmic scale. The apparent width of the phonon peak is due to the resolution effects. The insert shows the temperature and the q dependences of the intensity of the central peak. 1 rlu = 1.567 Å^{-1}.

Before analyzing the inelastic neutron spectra quantitatively, it is convenient to address the q-dependence of the elastic neutron response. Figure 1 shows representative elastic scans along the (1, 1 ± q, 0) direction at T = 760 and 1030 K, respectively. This intense and broad scattering is similar to the diffuse scattering observed in $KNbO_3$ by Guinier *et al.* [8] using X-rays and reflects the presence of atomic disorder in the perovskite cell. In $KNbO_3$, atomic disorder yields diffuse scattering along the [100] direction both in the X-ray and neutron diffraction patterns. Here, we approximate the line-shape of the neutron diffuse scattering intensity by a Lorentzian profile:

$$A(q) = \frac{1}{\pi}\frac{I_0}{(q-q_0)^2+\kappa^2}, \qquad (1)$$

where q_0 is the position in reciprocal space, κ is the inverse of the correlation length ξ, and I_0 yields the integrated intensity. From a fit to the elastic data at T = 1030 K, we obtain ξ = 64 ± 6 Å. It turns out that the shape and intensity of the diffuse scattering measured in the (2, 0, 0) Brillouin zone (BZ) do not depend on temperature (see insert of Fig. 2). This is in agreement with the results of [8], where the intensity of the diffuse scattering is found to be temperature-independent in the cubic phase and to decrease abruptly by ~30% immediately below T_C. On the other hand, it turns out that the intensity of the diffuse scattering measured along (1, 1 ± q, 0) slowly decreases when increasing the temperature from T_C. This suggests that, in this BZ and for temperatures relatively close to T_C, the diffuse scattering consists of two Lorentzian components (see inset of Fig. 1).

We now turn to the analysis of the inelastic neutron scattering spectra. Figure 2 shows an example of a constant-q scan taken at **Q** = (2, –0.1, 0) and T = 1030 K. The spectrum contains an inelastic peak at $\hbar\omega$ = 4 meV from the transverse acoustic (TA) phonon and a narrow peak centered around zero-energy transfer. To analyze the data quantitatively, we, hence, modeled the neutron scattering intensity $I(\mathbf{Q}, \omega)$ in the following way:

$$I(\mathbf{Q}, \omega) = S(\mathbf{Q}, \omega) \otimes R(\mathbf{Q}, \omega) + B. \qquad (2)$$

The symbol ⊗ stands for the 4D convolution with the spectrometer resolution function $R(\mathbf{Q}, \omega)$ [9]; B denotes the background level; and $S(\mathbf{Q}, \omega)$ is the neutron scattering function, which is related to the imaginary part of the dynamical susceptibility $\chi''(\mathbf{Q}, \omega)$ through

$$S(\mathbf{Q}, \omega) = \frac{[n(\omega)+1]}{\pi}\chi''(\mathbf{Q}, \omega), \qquad (3)$$

with the temperature factor $[n(\omega) + 1] = [1 - \exp(-\omega/T)]^{-1}$. We approximate the central peak by a δ-function in energy

$$S_{CP} = A(q)\delta(\omega), \qquad (4)$$

with $A(q)$ given by Eq. (1). The line-shape of the acoustic phonon is given by the usual damped-harmonic oscillator (DHO),

$$\chi_{\text{DHO}}(\mathbf{q}, \omega) = (\Omega_q^2 - i\gamma_q\omega - \omega^2)^{-1}. \qquad (5)$$

In Eq. (5), γ_q is the damping and $\Omega_q = \sqrt{\omega_q^2 + \gamma_q^2}$ with $\omega_q = cq$ [10] is the renormalized frequency of the acoustic phonons. For small values of momentum transfers **q**, a linear dispersion for the acoustic phonon branch is a reasonable approximation and the phonon damping approximately follows a dq^2-dependence

[11]. The scattering function used to fit the neutron data then reads

$$S(\mathbf{Q}, \omega) = S_{CP}(\mathbf{Q}, \omega) + \frac{[n(\omega)+1]}{\pi} f_1^2 \chi''_{\mathrm{DHO}}(\mathbf{Q}, \omega), \quad (6)$$

where $\mathbf{Q} = \mathbf{q} + \tau$ is the neutron scattering vector, τ is a reciprocal lattice vector, and f_1 is the structure factor of the acoustic phonon. As shown in Fig. 2, Eqs. (1)–(6) parametrize the experimental data in the (2, 0, 0) BZ well. The central peak is resolution-limited and temperature-independent. The acoustic phonon branch has a stiffness $c = 28 \pm 1.3$ meV Å^2, and the damping is small at low q, $\gamma_q = dq^2$ with $d = 55 \pm 6$ meV Å^2 ($0.05 < q < 0.15$ (rlu)). In the temperature range 750 K $< T <$ 1030 K, no qualitative change in the dispersion of the acoustic phonon was observed for data taken along (2, q, 0) ($|q| < 0.15$ (rlu)).

On the contrary, for temperatures below $T = 1030$ K, an additional component is observed in the inelastic spectra for constant-$\mathbf{q}$ scans in the (1, 1, 0) BZ. For means of comparison, Fig. 3 shows two representative neutron scattering spectra measured in the (1, 1, 0) BZ at $T = 1030$ and 727 K, respectively. At $T = 1030$ K, the spectrum consists of two components: a central peak (CP) and a phonon response around $\hbar\omega = 4$ meV. However, as the temperature is lowered to $T = 727$ K, additional quasielastic scattering (QE) appears along the (1, $1 \pm q$, 0) direction. The intensity of this quasielastic scattering grows when approaching T_C. From the above discussion, we conclude that, in the (1, 1, 0) BZ, the inelastic neutron spectra consist of three contributions: a central peak, quasielastic, and phonon scattering. To describe the quasielastic scattering, we introduce a Debye-like relaxation function,

$$\chi_{q-el}(\mathbf{q}, \omega) = \frac{\chi(0, T)}{1 + q^2/\kappa^2}(1 - i\omega/\Gamma_q)^{-1}, \quad (7)$$

where $\chi(0, T)$ is the temperature-dependent static susceptibility, κ is the inverse of the correlation length, and $\Gamma_q = \Gamma_0 + Dq^2$. Taking into account the quasielastic scattering modifies the neutron cross section to

$$S(\mathbf{Q}, \omega) = S_{CP}(\mathbf{Q}, \omega) + \frac{[n(\omega)+1]}{\pi}[f_1^2 \chi''_{\mathrm{DHO}}(\mathbf{Q}, \omega) + f_2^2 \chi''_{q-el}(\mathbf{Q}, \omega)]. \quad (8)$$

However, the scattering function given in Eq. (8) fails in reproducing the experimental data in the (1, 1, 0) BZ for $T < 1030$ K. For example, Fig. 3 shows an inelastic spectrum at $T = 727$ K and $\mathbf{Q} = (1, 1.075, 0)$, where a qualitative change in the phonon line-shape accompanied by a shift in the position of the phonon peak is observed. These two effects suggest that coupling between the quasielastic component and the acoustic phonons becomes important as the temperature approaches T_C.

The dynamical susceptibility for two coupled excitations was considered in details in [3, 12, 13] and is given by

$$\chi_{CM}(\mathbf{Q}, \omega) = \frac{f_1^2 \chi_1 + f_2^2 \chi_2 + 2\lambda f_1 f_2 \chi_1 \chi_2}{1 - \lambda^2 \chi_1 \chi_2}, \quad (9)$$

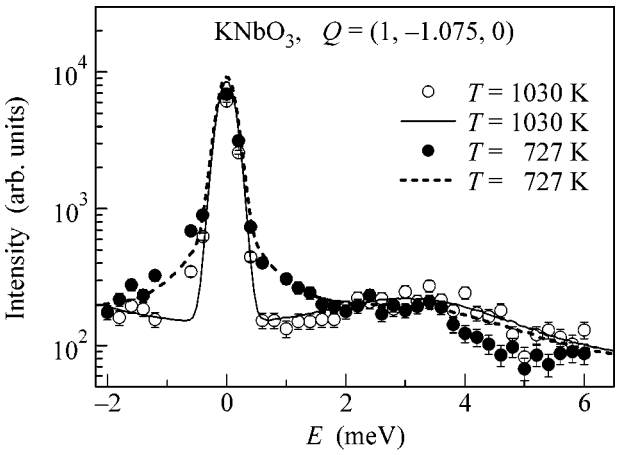

Fig. 3. Neutron scattering spectrum from $KNbO_3$ at $T = 1030$ and 727 K, respectively. The solid and dashed lines are the results of fit as described in the text. To emphasize the QE component, the intensity is given in a logarithmic scale. Note the pronounced change in the phonon line-shape at lower temperature.

where $\chi_i \equiv \chi_i(\mathbf{Q}, \omega)$, $i = 1, 2$ are the dynamical susceptibilities of the uncoupled phonon and QE component, respectively. In the following, we take f_i as real constants, since in $KNbO_3$, all the atoms are situated on centers of symmetry. The interaction term is $\lambda \equiv \lambda(q, \omega) = (g_r + i\omega g_i)q^2$. Finally, the scattering function reads

$$S(\mathbf{Q}, \omega) = S_{CP}(\mathbf{Q}, \omega) + \frac{[n(\omega)+1]}{\pi}\chi''_{CM}. \quad (10)$$

In order to obtain a good agreement between Eq. (10) and the neutron spectra, it was necessary to fit the complete set of data ($0 < q < 0.2$) taken at a given temperature simultaneously. Figures 4 and 5 show the results of such calculations for $T = 727$ and 760 K. We obtain $g_r = 20 \pm 3$ meV^2 Å^2 and $g_i = 95 \pm 6$ meV^2 Å^2. Introduction of a coupling between the QE and acoustic modes has two consequences. First, Eq. (9) yields a better description of the line-shape of the inelastic neutron spectra. Second, $\chi''_{CM}(\mathbf{Q}, \omega)$ is enhanced at low-energy transfers. Further, we obtained $\Gamma_0 = 0.19 \pm 0.05$ meV and $D = 44 \pm 4$ meV Å^2 for the damping of the QE component. As discussed above, both the CP and the line-shape of the acoustic phonons are temperature-independent in the (2, 0, 0) BZ. Hence, to fit the data measured in the (1, 1, 0) BZ as a function of temperature, we fixed the parameters of the CP and the acoustic phonons. The only parameter left to describe the temperature dependence of the neutron spectra is the susceptibility of QE scattering $\chi(0, T)$. As shown in Fig. 5, the intensity of the quasielastic component is a maximum close to T_C and decreases continuously with increasing temperature. The temperature dependence of $\chi(0, T)$ follows approximately the Curie–Weiss law $\propto 1/(T - T_0)$ with $T_0 = 615 \pm 23$ K in good agreement with the value deduced from dielectric measurements

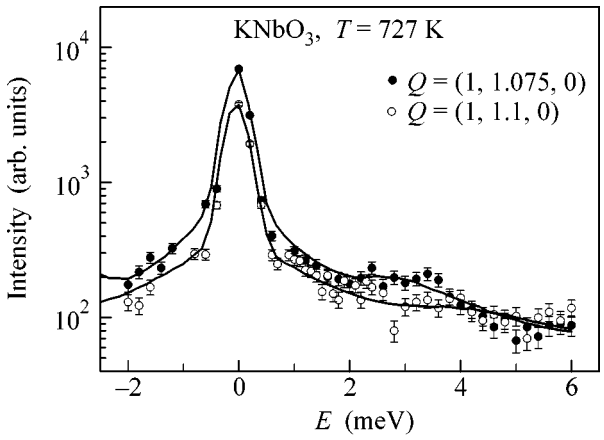

Fig. 4. Observed and fitted inelastic neutron intensities taken in the (1, 1, 0) BZ at $T = 727$ K. Fitted curves were obtained with Eq. (10). Intensity is given in a logarithmic scale.

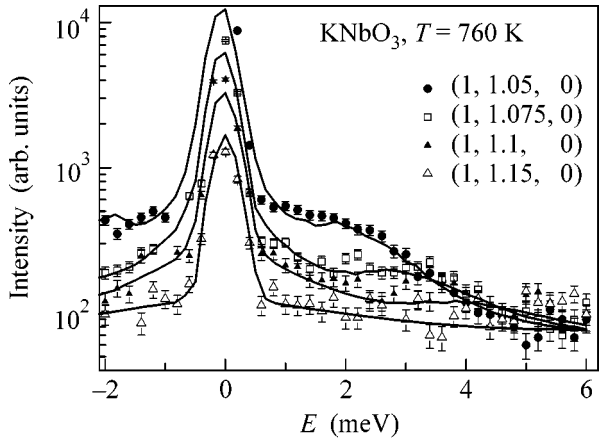

Fig. 5. Observed and fitted inelastic neutron intensities taken in the (1, 1, 0) BZ at $T = 760$ K. Fitted curves were obtained with Eq. (10). Intensity is given in a logarithmic scale.

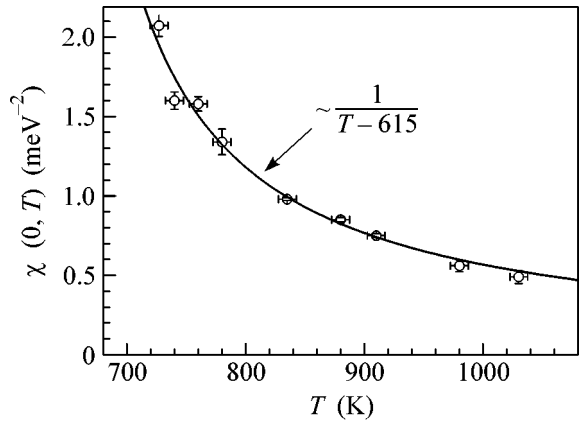

Fig. 6. Temperature dependence of the susceptibility of the QE component. The solid line is a fit to the data as explained in the text.

$T_0 = 633 \pm 5.9$ K [14] and $T_0 = 615$ K [15]. This suggests that the cubic–tetragonal transition in $KNbO_3$ is driven by the quasielastic relaxational excitation. The intensity of the quasielastic component is strong in the (1, 1, 0) zone and has a small intensity in the (2, 0, 0) Brillouin zone, which indicates that the relaxation mode is due to correlated atomic motion of optical character. However, at all q and temperatures, we did not observe that the relaxation mode evolves into an underdamped optic phonon branch. Thus, we conclude that QE scattering in $KNbO_3$ is not due to a usual overdamped soft phonon but is related to disorder in the lattice.

To summarize, we measured the low-energy part of the vibration spectrum of $KNbO_3$ in the cubic phase with inelastic neutron scattering. We find a coexistence of a static and a quasielastic component. The static component appears to correspond with static disorder in the cubic cell and is temperature-independent in agreement with X-ray results [5]. The quasielastic component is coupled with the acoustic phonon branch, and its intensity follows the Curie–Weiss law well.

This work was performed at the spallation neutron source SINQ, Paul Scherrer Institut, Villigen (Switzerland) and was partially supported by the Russian Foundation for Basic Research, grant no. 02-02-17678. P. Günter and A. Choubey acknowledge partial support by the Swiss National Science Foundation.

REFERENCES

1. G. A. Smolenskiĭ, V. A. Bokov, V. A. Isupov, N. N. Krainik, R. E. Pasynkov, and M. S. Shur, *Ferroelectrics and Related Materials* (Nauka, Leningrad, 1971; Gordon and Breach, New York, 1984).
2. M. E. Lines and A. M. Glass, *Principles and Applications of Ferroelectrics and Related Materials* (Clarendon Press, Oxford, 1977; Mir, Moscow, 1981).
3. A. D. Bruce and R. A. Cowley, *Structural Phase Transitions* (Taylor and Francis, London, 1981; Mir, Moscow, 1984).
4. G. Shirane, H. Danner, A. Pavlovic, and R. Pepinsky, Phys. Rev. **93**, 672 (1954).
5. A. C. Nunes, J. D. Axe, and G. Shirane, Ferroelectrics **2**, 291 (1971).
6. M. Holma and Haydn Chen, J. Phys. Chem. Solids **57**, 1465 (1996).
7. M. D. Fontana, A. Ridah, G. E. Kugel, and C. Carabatos-Nedelec, J. Phys. C **21**, 5853 (1988).
8. R. Comes, M. Lambert, and A. Guinier, Acta Crystallogr. A **26**, 244 (1970).
9. M. Popovichi, Acta Crystallogr. A **31**, 507 (1975).
10. B. Fåk and B. Dorner, Physica B (Amsterdam) **234**, 1107 (1997).
11. A. A. Maradudin and A. E. Fein, Phys. Rev. **128**, 2589 (1962).
12. R. K. Wehner and E. F. Steigmeier, RCA Rev. **36**, 70 (1975).
13. G. J. Coombs and R. A. Cowley, J. Phys. C **6**, 121 (1973).
14. S. Triebwasser, Phys. Rev. **101**, 993 (1956).
15. V. K. Yanovskii, Sov. Phys. Solid State **22**, 1284 (1980).

JETP Letters, Vol. 80, No. 5, 2004, pp. 359–362. From Pis'ma v Zhurnal Éksperimental'noĭ i Teoreticheskoĭ Fiziki, Vol. 80, No. 5, 2004, pp. 408–411.

Unexpected Negative Nonmonotonic Magnetoresistance of the Two-Dimensional Electrons in Si in a Parallel Magnetic Field¶

V. M. Pudalov[1, *], A. S. Kirichenko[1], N. N. Klimov[2, 3], M. E. Gershenson[3], and H. Kojima[3]

[1] *Lebedev Physics Institute, Russian Academy of Sciences, Moscow, 119991 Russia*

** e-mail: pudalov@lebedev.ru*

[2] *Lebedev Physics Research Center, Moscow, 119991 Russia*

[3] *Department of Physics and Astronomy, Rutgers University, New Jersey 08854, United States*

Received July 29, 2004

We report observation of the unexpected *negative* and *nonmonotonic* magnetoresistance of 2D electrons in Si-MOSFET subjected to a varying in-plane magnetic field superimposed on a constant perpendicular field component. We show that this nonmonotonic magnetoresistance is irrelevant to the energy spectrum of mobile 2D electrons. We also observed variations of the density of mobile electrons with the in-plane field. We argue that both variations of the negative magnetoresistance and of the density of mobile electrons originate from the band of localized states. The latter coexist and interact with mobile electrons even at relatively high density, a factor of 1.5 higher than the critical density of the apparent metal-insulator transition. © *2004 MAIK "Nauka/Interperiodica".*

PACS numbers: 71.10.Ay; 71.30.1h; 72.10.2d; 73.40.Qv

The properties of the dilute strongly interacting two-dimensional (2D) electron liquid, and, in particular, the apparent metal-insulator transition (MIT) in 2D remain challenging [1, 2]. One of the main problems here is to understand the individual roles of two major driving forces, disorder and electron–electron (e–e) interactions. Purely interaction effects between mobile 2D electrons have been intensely studied both theoretically [3–9] and experimentally [10–14]; the role of disorder in these studies is limited to scattering of mobile electrons solely.

In contrast, the interplay of disorder and interactions, particularly interaction between localized and mobile electrons, is considered much rarely [15–17]; experimental investigations of it are rare. One might expect that the interplay should become more and more important as electron density decreases and approaches the critical density of the 2D MIT.

Usually, the presence of the localized states does not reveal itself in 2D transport, which is dominated by mobile electrons. The in-plane magnetic field, in a first approximation, does not couple to orbital motion, affecting only spins of mobile and localized electrons; for this reason, the in-plane field is a useful tool for studying localized states. Correspondingly, the influence of the localized states on magnetotransport have been detected in [18–20] in the strong in-plane field $g\mu B_{\|} \sim 2E_F$: under such conditions, the magnetoresistance (MR) and the field of its saturation have been found to depend on disorder (e.g., on sample mobility) and deviate from the behavior predicted for purely mobile electrons [5, 6].

In the current paper, we report an observation of the negative and nonmonotonic MR in weak in-plane fields $g\mu B_{\|} \ll 2E_F$, which arises when perpendicular component $B_{\perp}$ of the field is superimposed onto in-plane component $B_{\|}$. Measurements have been made with a high-quality Si-MOS sample (peak mobility 2.4 m^2/Vs at $T \approx 0.1$ K) in ^{3}He/^{4}He dilution refrigerator. The perpendicular and in-plane components of the magnetic field were independently controlled using a crossed-field set-up with two superconducting coils [10].

Figure 1 shows the MR versus perpendicular field for different fixed $B_{\|}$ values. Starting the field of ~0.3 T (right after the weak localization suppression), on the top of the interaction-induced monotonic MR $\delta\rho_{xx}(B_{\perp}) \propto -(\omega_c\tau)^2$ [6], one can see conventional Shubnikov-de Haas (SdH) oscillations. Density values n quoted in the paper were determined from the period of these oscillations in perpendicular field. The oscillatory component $\rho_{xx}(B_{\perp})$ is in a qualitative agreement with conventional theory of quantum oscillations.

In the purely in-plane field, for the density range studied, $(1.1–2.2) \times 10^{11}$ cm^{-2}, the MR grows monotonically ($\propto B_{\|}^2$ in low fields) [11] in a qualitative agreement with the interaction-induced MR [5, 6]. However,

¶ This article was submitted by the authors in English.

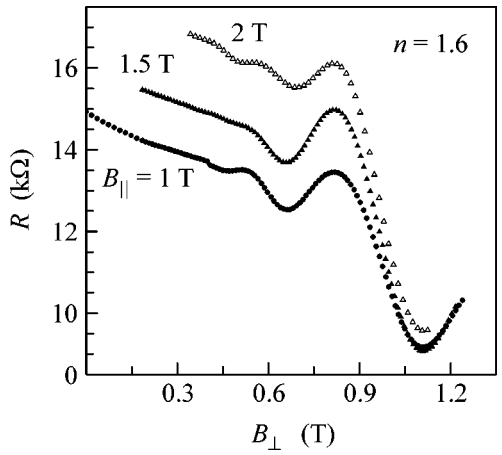

Fig. 1. Shubnikov-de Haas oscillations in a perpendicular field for three values of the in-plane field $B_{||}$. Density is indicated in units of 10^{11} cm^{-2}.

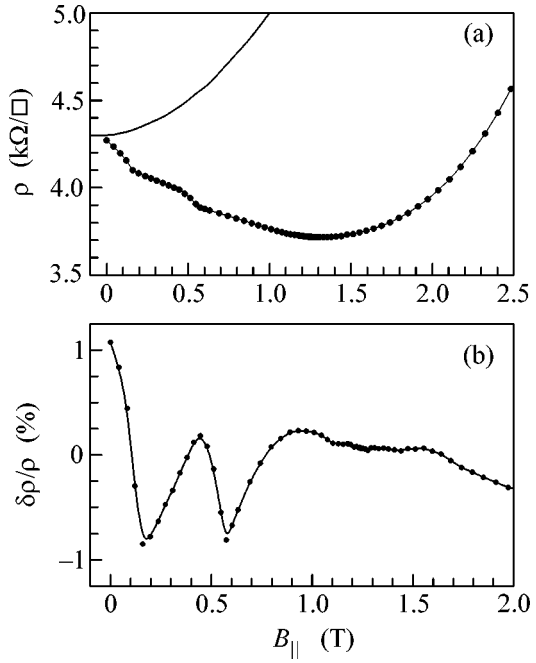

Fig. 2. (a) Typical $\rho(B_{||})$ dependence in the presence of the $B_\perp$ field (dots); $\rho(B_{||})$ calculated according to Eqs. (1) and (2). (b) Oscillations $\delta\rho/\rho$ vs. $B_{||}$. Electron density $n = 1.6 \times 10^{11}$ cm^{-2}, temperature $T = 0.2$ K, $B_\perp = 1.14$ T.

when a fixed perpendicular field is applied and the in-plane field is swept, the MR varies in unexpected non-monotonic fashion, as shown in Fig. 2. First, the resistance decreases, passes through a minimum and, then, starts rising as anticipated [5, 6]. For $n = 1.6 \times 10^{11}$ cm^{-2}, the minimum occurs at $B_{||} \approx 1.3$ T, as shown in Fig. 2a. Second, the resistance exhibits weak oscillations; the oscillations are enlarged in Fig. 2b by subtracting the monotonic background (fitted with the second order polynomial). The field-positions of the two $\rho(B_{||})$ minima in Fig. 2 depend on electron density and on $B_\perp$ field. We note that, at higher densities and higher $k_F l \gg 1$ values, these effects are not seen and the field dependence of $\rho_{xx}(B_{||})$ measured on these same samples becomes monotonic [11].

The *monotonic* negative magnetoresistance versus $B_{||}$ might be a result of the interaction-induced corrections to σ_{xx} [5, 6]:

$$\frac{\delta\rho_{xx}(B_{||})}{\rho_D} \approx -[1-(\omega_\perp\tau)^2]\frac{\delta\sigma_{xx}^{ee}(B_{||})}{\sigma_D}, \qquad (1)$$

where $\omega_\perp$ is the cyclotron frequency in the $B_\perp$-field and $\delta\sigma_{xx}^{ee}(B_{||})$ is *negative* and caused by the magnetic field switching-off of the spin-exchange processes in the triplet channel [5]:

$$\delta\sigma_{xx}^{ee} \approx \frac{k_B T\tau}{\hbar}\left[\frac{8F_0^a}{1+F_0^a}K_b(x) + K_d(x, F_0^a)\right], \qquad (2)$$

where the K_b and K_d are functions of $x = g^*\mu B_{||}/k_B T$, as given in [5]. The line in Fig. 2 shows the theoretical dependence calculated according to Eqs. (1) and (2), using the measured [10] value $F_0^a = -0.45$ for this density. The calculated dependence appears to be much stronger. Moreover, it describes a *positive* (rather than *negative*) MR, because, for the given value $\omega_c\tau \equiv \mu B_{||} = 0.76 < 1$, the square bracket in Eq. (1) is positive.

We conclude, therefore, that, for low densities and low $k_F l \sim 1$ values, the MR in $B_{||}$ field is governed by mechanisms different from purely interaction corrections [5, 6]; this conclusion is in accord with our earlier observations [19, 18]. In attempt to identify the origin of the $\rho(B_{||})$ oscillations, for each electron density, we have calculated the energy spectrum using the experimentally determined [10] renormalized m^* and g^*-factor values. Figure 3 represents an example of the calculated energy spectrum for one density and $B_\perp$ field value. In this plot, the energy levels vary as

$$E_n{\downarrow\uparrow} = \left(n+\frac{1}{2}\right)\hbar\omega_c^* \pm \frac{1}{2}g^*\mu\sqrt{B_\perp^2 + B_{||}^2}. \qquad (3)$$

For simplicity, we have neglected: (i) the quantum oscillations of the Fermi energy, (ii) $B_\perp$- and $B_{||}$-field dependences of the effective mass and g-factor, and (iii) the valley splitting. We also presumed that $E_F(0) = n\pi\hbar^2/g_v m^*$, with m^* being the renormalized effective mass [10].

Considering the energy spectrum of mobile electrons calculated with the above reasonably admitted assumptions, we find that it cannot produce either a negative MR or its oscillations. Indeed, the $B_\perp$ field of 1.14 T is chosen so that E_F lies in the middle of the energy gap; this is confirmed by Fig. 1, where this field

corresponds to the resistivity minimum. As $B_\parallel$ increases, the Fermi energy remains within the same energy gap until ≈4 T (see Fig. 3); therefore, no oscillations can be anticipated until $B_\parallel = 4$ T. In order to test whether or not the presence of a *fixed* in-plane field causes unforeseen changes to the energy spectrum, we have made similar calculations of the energy spectra at a varying $B_\perp$ field for each curves shown in Fig. 1 (i.e., for $B_\parallel = 1$, 1.5, and 2 T); the calculated spectra agree with the SdH oscillations. We conclude, therefore, that the observed features in $R(B_\parallel)$ are not (solely) related with the energy spectrum of mobile 2D electrons.

In order to elucidate the origin of the anomalous oscillatory and negative MR (Fig. 2), we plot, in Fig. 4, the typical density n of mobile electrons versus the $B_\parallel$ field as determined from fitting the SdH oscillations [10] at fixed gate voltage value. The perpendicular field in these SdH measurements varied from 0.2 to 1 T to provide sufficiently high number of filled Landau levels (>8) and a weak amplitude of the oscillations $\delta\rho/\rho \ll 1$. As Fig. 4 shows, the density of mobile electrons *increases* slightly with the in-plane field; this does not correlate with either the energy spectrum (Fig. 3) or with a weak monotonic dependence of the effective mass (and, hence, the Fermi energy) on $B_\parallel$ [21, 22, 14] (note that the frequency of SdH oscillations does not depend on m^* being dependent solely on the Landau level's degeneracy). Since the total charge in the Si-MOSFET (which is a plane capacitor) does not vary with $B_\parallel$, we conclude that there is an exchange of electrons of a few percent between the reservoirs of 2D-mobile and localized states.

The effects of exchange of electrons are natural if the localized electrons fill the upper Hubbard band [15, 16]; the latter will float up toward the Fermi energy as density decreases. The upper Hubbard band is expected to be narrow [16]; therefore, the in-plane magnetic field should quickly polarize it. The spin-polarization and motion of the band of localized states in the $B_\parallel$ field may thus be the reason for the dependence of n on $B_\parallel$ shown in Fig. 4. The latter dependence, in its turn, explains semiquantitatively the unexpected monotonic negative MR, $\Delta\rho$, as observed in the $B_\parallel$ field [see Fig. 2a]: $\Delta\rho = (d\rho/dn)\Delta n(B_\parallel)$. With the experimentally determined value $d\rho(B = 0)/dn = 11.5k\Omega/\square$ per 10^{11} cm^{-2} (for this same gate voltage) and $\Delta n(B_\parallel) = 5 \times 10^9$ cm^{-2} (see Fig. 4), we anticipate a decrease in $\rho(B_\parallel) = 0.6k\Omega/\square$ in the field range $B_\parallel = 0$–1.5 T, which agrees well with the monotonic negative magnetoresistance, shown in Fig. 2.

The nonmonotonic variation of the MR may also result from the peaked structure of the Hubbard band. The role of the $B_\perp$-field in this picture is to produce a ladder structure of the density of states in the band of mobile electrons, Eq. (1); this ladder moves with the in-plane field relative to the peaked Hubbard band. Therefore, the nonmonotonic MR is not seen in a purely in-plane field, though the localized band contributes a sample-dependent monotonic part to the in-plane field magnetoresistance [19, 11, 18]. An interesting question is whether or not the density of mobile electrons varies solely with a $B_\parallel$ or with a $B_\perp$ field; however, answering this question poses a difficult technical challenge.

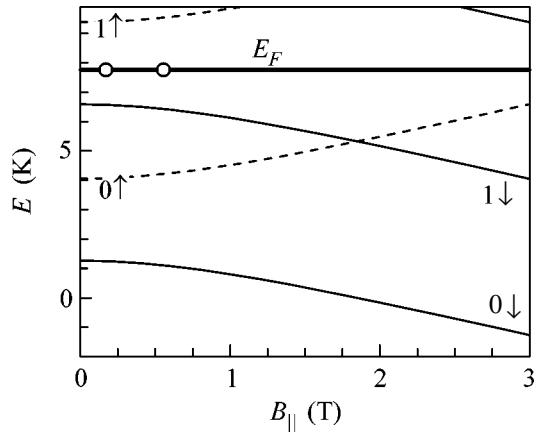

Fig. 3. Energy spectrum of mobile 2D-electrons calculated for $n = 1.6 \times 10^{11}$ cm^{-2} and $B_\perp = 1.14$ T, with the renormalized m^* and g^*-factor measured in [10]. Bold dots mark field positions of the measured MR minima. Bold line shows Fermi energy E_F, and thin lines show energy levels for spin down (↓) and spin up (↑) electrons. The levels are doubly degenerate, due to the two valley-spectrum.

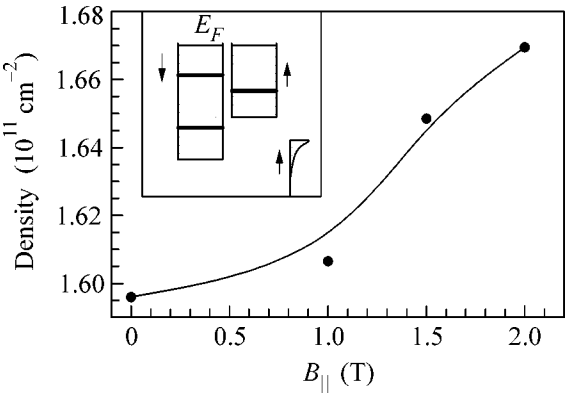

Fig. 4. Typical dependence of the density of mobile electrons on the in-plane magnetic field, determined from the Shubnikov-de Haas oscillations period. Inset shows schematic energy diagram of the spin up, spin down and impurity bands, and direction of their motion with $B_\parallel$ field. Energy spectrum corresponds to $B_\perp = 1.14$ T and $B_\parallel = 1$ T.

To *summarize*, for the low-density 2D electron liquid in Si ($n \sim 10^{11}$ cm^{-2}; close to but noticeably larger than the critical density), we observed an unexpected negative and oscillatory magnetoresistance in the in-plane magnetic field when a weak perpendicular component of the field is superimposed onto the in-plane

field. Analysis of MR features shows that the negative MR and its oscillations are irrelevant to the energy spectrum of mobile electrons. We also observed a concomitant weak variation of the density of mobile electrons with $B_{\|}$. The density variation is likely to cause the unexpected negative MR. We believe that the observed effects hint at the involvement of the localized states in the transport at low densities; the latter may supply electrons to and from the band of extended states even at a density as high as 60% larger than the critical density of the M-I transition. In other words, the observed effects are evidence for the hybridization of mobile and localized carriers in the vicinity of a 2D MIT. As electron density decreases and approaches the critical value of the MIT, the interaction between the localized and extended states is expected to grow. The interaction between the mobile and localized states, which is often ignored, may play an essential role in the overall phenomenon of 2D MIT.

The work was partially supported by the NSF, ARO MURI, INTAS, RFBR, and Russian programs "Strongly Correlated Electrons," "Physics of Nanostructures," "Quantum and Nonlinear Processes," and "Integration," and a State Support for Leading Scientific Schools program.

REFERENCES

1. E. Abrahams, S. Kravchenko, and M. P. Sarachik, Rev. Mod. Phys. **73**, 251 (2001).
2. B. L. Altshuler, D. L. Maslov, and V. M. Pudalov, Physica E (Amsterdam) **9**, 209 (2001).
3. B. L. Altshuler and A. G. Aronov, in *Electron–Electron Interactions in Disordered Systems*, Ed. by A. L. Efros and M. A. Pollak (Elsevier, Amsterdam, 1985); P. A. Lee and T. V. Ramakrishnan, Rev. Mod. Phys. **57**, 287 (1985).
4. S. Das Sarma and E. H. Hwang, Phys. Rev. Lett. **83**, 164 (1999).
5. G. Zala, B. N. Narozny, and I. L. Aleiner, Phys. Rev. B **64**, 214204 (2001); cond-mat/0109531; Phys. Rev. B **65**, 20201R (2002).
6. I. V. Gornyi and A. D. Mirlin, Phys. Rev. B **69**, 045313 (2004).
7. A. M. Finkelstein, in *Soviet Scientific Review*, Ed. by I. M. Khalatnikov (Harwood Academic, London, 1990), Vol. 14, p. 3.
8. C. Castellani, Phys. Rev. B **30**, 527 (1984); C. Castellani, G. Kotliar, and P. A. Lee, Phys. Rev. Lett. **59**, 323 (1987); C. Castellani, C. DiCastro, H. Fukuyama, *et al.*, Phys. Rev. B **33**, 7277 (1986); C. Castellani, C. Di Castro, and P. A. Lee, Phys. Rev. B **57**, R9381 (1998).
9. A. Punnoose and A. M. Finkelstein, Phys. Rev. Lett. **88**, 016802 (2002).
10. V. M. Pudalov, M. Gershenson, H. Kojima, *et al.*, Phys. Rev. Lett. **88**, 196404 (2002).
11. V. M. Pudalov, M. Gershenson, H. Kojima, *et al.*, Phys. Rev. Lett. **91**, 126403 (2003).
12. S. A. Vitkalov, K. James, B. N. Narozhny, *et al.*, Phys. Rev. B **67**, 113310 (2003).
13. Y. Y. Proskuryakov, A. K. Savchenko, S. S. Safonov, *et al.*, Phys. Rev. Lett. **89**, 076406 (2002).
14. J. Zhu, H. L. Stormer, L. N. Pfeiffer, *et al.*, Phys. Rev. Lett. **90**, 056805 (2003).
15. N. F. Mott, *Metal–Insulator Transitions* (Taylor and Francis, London, 1974; Nauka, Moscow, 1979).
16. V. I. Kozub and N. V. Agrinskaya, Phys. Rev. B **64**, 245103 (2001).
17. T. M. Klapwijk and S. Das Sarma, Solid State Commun. **110**, 581 (1999).
18. V. M. Pudalov, G. Brunthaler, A. Prinz, and G. Bauer, Phys. Rev. Lett. **88**, 076401 (2002).
19. V. M. Pudalov, G. Brunthaler, A. Prinz, and G. Bauer, cond-mat/0103087.
20. V. M. Pudalov, M. E. Gershenson, and H. Kojima, cond-mat/0201001.
21. F. Stern, Phys. Rev. Lett. **21**, 1687 (1968).
22. E. Tutuc, E. Melinte, E. P. De Poortere, *et al.*, Phys. Rev. B **67**, 241309 (2003).

JETP Letters, Vol. 80, No. 5, 2004, pp. 363–366. From Pis'ma v Zhurnal Éksperimental'noĭ i Teoreticheskoĭ Fiziki, Vol. 80, No. 5, 2004, pp. 412–415.

Absolute Negative Conductivity and Zero-Resistance States in Two-Dimensional Electron Systems: A Plausible Scenario¶

V. Ryzhii[1], A. Chaplik[1, 2], and R. Suris[3]

[1] *University of Aizu, Aizu-Wakamatsu, Ikki-machi 965-8580, Japan*

[2] *Institute of Semiconductor Physics, Russian Academy of Sciences, Novosibirsk, 630090 Russia*

[3] *Ioffe Physical-Technical Institute, Russian Academy of Sciences, St. Petersburg, 194121 Russia*

Received July 29, 2004

We present a model that provides a plausible explanation of the effect of zero-resistance and zero-conductance states in two-dimensional electron systems subjected to a magnetic field and irradiated with microwaves observed in a number of experiments and of the effect's main features. The model is based on the concept of absolute negative conductivity associated with photon-assisted scattering of electrons on impurities. It is shown that the main features of the effect can be attributed to the interplay of different electron scattering mechanisms.
© *2004 MAIK "Nauka/Interperiodica".*

PACS numbers: 73.40.-c; 73.43.-f; 78.67.n

1. INTRODUCTION

The possibility of states in which the dissipative electric current in a nonequilibrium electron system (a system in which the majority of electrons have negative effective mass) flows in the direction opposite to the electric field, i.e., the usual (or absolute) conductivity of the system is negative, was discussed by Kroemer in the late 1950s [1]. Rather realistic mechanisms of such an absolute negative conductivity (ANC) in two- and three-dimensional substantially nonequilibrium electron systems (2DESs and 3DESs) in magnetic field were considered more than three decades ago [2–4]. At the same time, the mechanism of ANC in a 2DES subjected to a magnetic field and irradiated with microwaves associated with impurity scattering of 2D electrons accompanied by the absorption of microwave photons was proposed by one of us [5]. It was shown that the dissipative conductivity is an oscillatory function of the ratio of microwave frequency Ω to electron cyclotron frequency Ω_c. At Ω somewhat exceeding Ω_c or a multiple of Ω_c, the photon-assisted impurity scattering of 2D electrons with their transitions between the Landau levels (LLs) results in a contribution to the dissipative current flowing opposite to the electric field. At sufficiently strong microwave radiation, this scattering mechanism can dominate, leading to ANC when $\Omega \gtrsim N\Omega_c$, where $N = 1, 2, 3, \ldots$. The transformation of the dissipative current versus electric field characteristic is schematically shown in Fig. 1. The effect of vanishing electrical resistance (in the Hall bar configuration) and of vanishing electrical conductance (in the Corbino configuration) in a 2DES in magnetic field irradiated with microwaves has recently been observed by Mani *et al.* [6], Zudov *et al.* [7], and Yang *et al.* [8]. Anderson and Brinkman [9], Andreev *et al.* [10], and Volkov and coworkers [11] suggested that this effect, i.e., the appearance of ZR-states (and ZC-states), is attributed to ANC associated with photon-assisted impurity scattering of 2D electrons (put forward in [5, 12]) and an instability of homogeneous states in a conductive media with ANC. The latter was noted by Zakharov [13] and discussed in early papers on ANC in 2DESs (see, for example, [4]). The structure of the electric-field distributions corresponding to ZR- and ZC-states that arose as a result of the instability is determined by the shape of the current-voltage characteristic (in particular, by the value of E_0) and the features of the diffusion processes. Recent experimental findings [6–8] have stimulated a surge of experimental (for example, [14–17]) and theoretical papers (for example, [18–24]). Preliminary brief overviews can be found in [25, 26]. In particular, the results of early theoretical studies of ANC caused by photon-assisted impurity scattering

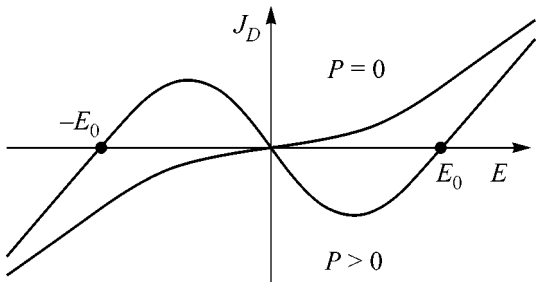

Fig. 1. Schematic view of dissipative current-voltage characteristics $J_D = J_D(E)$ without ($P = 0$) and with ($P > 0$) microwave irradiation.

¶ This article was submitted by the authors in English.

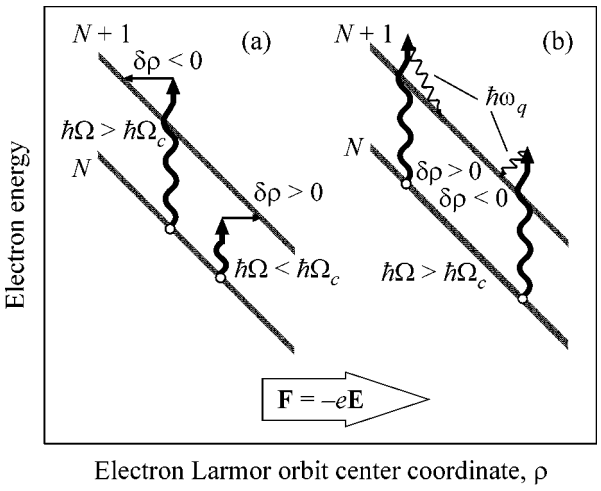

Fig. 2. Inter-LL electron transitions: (a) photon-assisted impurity for both $\Omega > \Omega_c$ and $\Omega < \Omega_c$ and (b) photon-assisted acoustic phonon scattering mechanisms (only transitions for $\Omega > \Omega_c$ are shown).

were generalized by the inclusions of the LL broadening and high microwave power effects [18–20]. A quasiclassical model that is valid at large filling factors and sufficiently strong electric field (or when a long-range disorder determines the dissipative current) was developed by Vavilov and Aleiner [21]. A possible role of photon-assisted acoustic phonon scattering was discussed in [22–24].

A theoretical model for ZR- and ZC-states should explain at least the following details that are observed experimentally: (a) the phase of the magnetic-field dependence of the resistance (dissipative conductivity), i.e., the positions of maxima and minima; (b) very slow dependence of the magnitude of the dissipative conductivity maxima and minima on the microwave power (tending to saturation in the range of elevated powers); (c) steep decrease in the maxima and minima magnitude resulting in vanishing of ANC and, hence, in vanishing ZR- and ZC-states with increasing temperature; and (d) relatively small magnitude of the minima and maxima in 2DESs with moderate electron mobility that makes impossible the attainment of ANC and its consequences.

In this letter, we discuss a scenario for the appearance of zero-resistance (ZR) as well as zero-conductance (ZC) states in 2DESs invoking the concept of ANC associated with photon-assisted impurity scattering complicated by electron–electron interaction and photon-assisted acoustic phonon scattering. The proposed scenario provides plausible explanations of the main experimental facts.

2. ANC DUE TO PHOTON-ASSISTED SCATTERING

The effect of ANC in a 2DES system in magnetic field under microwave irradiation is associated with the following [5, 12]. The dissipative electron transport in the direction parallel to the electric field and perpendicular to the magnetic field is due to hops of the electron Larmor orbit centers caused by scattering processes. These hops result in a change in the electron potential energy, $\delta\epsilon = -F\delta\rho$. Here, F is the dc electric force acting on an electron that is determined by the net in-plane dc electric field, including both the applied and the Hall components, and $\delta\rho$ is the displacement of the electron orbit center. If the electron orbit center displaces in the direction of the electric force ($\delta\rho > 0$ and $\delta\epsilon < 0$), the electron potential energy decreases. In equilibrium, the electron orbit center hops in this direction are dominant, so the dissipative electron current flows in the direction of the net dc electric field. However, in some cases, the displacements of the electron orbit centers in the direction opposite to the electric force (with $\delta\rho < 0$ and, hence, $\delta\epsilon > 0$) can prevail, resulting, in the dissipative current flowing opposite to the electric field. Indeed, if an electron absorbs a photon and transfers to a higher LL, a portion of the absorbed energy $N\hbar\Omega_c$ ($\hbar$ is the Planck constant) goes to increase of the electron kinetic energy, hence, the change in the electron potential energy is $\delta\epsilon = \hbar(\Omega - N\hbar\Omega_c)$. If $(\Omega - N\hbar\Omega_c) > 0$, so that $\delta\rho < 0$ (see Fig. 2a), the potential energy of electrons increases with each act of their scattering.

3. PHASE OF THE DISSIPATIVE CONDUCTIVITY OSCILLATIONS

Summarizing the results of previous calculations [5, 12, 21] (see also [20, 22]), the variation of the dissipative dc current under the effect of microwave radiation (photocurrent) can be presented as

$$J_{\rm ph} \propto \sum_{N,M} \Theta_N I_N^M \frac{(N\Omega_c - M\Omega)}{[(\Lambda\Omega_c - M\Omega)^2 + \Gamma^2]^2}, \qquad (1)$$

if $FL \ll \hbar\Gamma$,

$$J_{\rm ph} \propto \sum_{N,M} \Theta_N I_N^M (N\Omega_c - M\Omega) \exp\left[-\frac{\hbar^2(N\Omega_c - M\Omega)^2}{2F^2L^2}\right], \qquad (2)$$

when $FL > \hbar\Gamma$ and $L > d_i$, and

$$J_{\rm ph} \propto \sum_{N,M} \Theta_N I_N^M (N\Omega_c - M\Omega) K_0\left(\frac{|N\Omega_c - M\Omega| d_i}{v_H}\right), \qquad (3)$$

when $FL > \hbar\Gamma$ and $L \ll d_i$ (smooth disorder). Here, e is the electron charge, Γ is the LL broadening; L is the magnetic length; d_i is the spacing between 2DES and the donor sheet; v_H is the Hall drift velocity, $K_0(z)$ is the McDonald function; and $\Theta_N = 1 - \exp(-N\hbar\Omega_c/T)$,

where T is the electron temperature. The factor Θ_N is due to the contribution of scattering processes with both absorption and emission of microwave photons. The coefficients I_N^M are determined by the matrix elements of photon-assisted interaction of electrons with impurities (remote ones and those in a 2DES) and surface roughness as well as by the amplitude of the ac microwave electric field $\mathscr{E}$ and the electron distribution function. As follows from (1)–(3), the microwave photocurrent reaches a maxima at $N\Omega_c - M\Omega = \Delta^{(+)}$ and minima at $N\Omega_c - M\Omega = -\Delta^{(-)}$ with $\Delta^{(+)} \simeq \Delta^{(-)} \sim \max\{\Gamma, FL/\hbar\}$. According to (1)–(3), the net dissipative current approximately coincides with its dark value at the resonances $N\Omega_c = M\Omega$. At $N\Omega_c - M\Omega = -\Delta^{(-)}$ and sufficiently strong microwave radiation (when $|J_{ph}| > J_{dark}$), the net dissipative dc current $J_D = J_{dark} + J_{ph}$ becomes directed opposite to the electric field, resulting in instability. This pattern of the oscillatory behavior of the microwave photocurrent is in line with the qualitative reasoning in the previous section. It is consistent with the experimental results [6–8, 14–16].

As shown, the photon-assisted acoustic phonon scattering processes (see Fig. 2b) also lead to an oscillatory dependence of the microwave photoconductivity. However, the phase of these oscillations is opposite to that in the case of photon-assisted impurity scattering [23, 24]. This can add complexity to the microwave photoconductivity oscillations and can even result in their suppression, particularly at elevated temperatures (see Section 6).

4. POWER NONLINEARITY

The dependence of the factor I_N^M microwave field is given by $J_M^2(\xi_\Omega)$, where $J_M(z)$ is the Bessel function and $\xi_\Omega \propto \mathscr{E}$ is proportional to the amplitude of classical oscillations of the electron orbit center in the microwave field (see, for example, [19, 20]). The terms with $M > 0$ correspond to the transitions with the absorption and emission of M real microwave photons. Thus, the magnitudes of the microwave photoconductivity maxima and minima, $\max\sigma_{ph}$ and $|\min\sigma_{ph}|$, where $\sigma_{ph} = J_{ph}/E$, are generally nonlinear functions of the microwave power $P \propto |\mathscr{E}|^2$. This is due to the effect of virtual photon absorption and emission on the electron scattering processes. At low microwave powers, $\max\sigma_{ph} \propto P$ and $|\min\sigma_{ph}| \propto P$. However, when $\xi_\Omega \propto \mathscr{E}$ approaches b_M, where b_M corresponds to the maximum value of $J_M(z)$, the magnitude of $\max\sigma_{ph}$ fairly slowly increases with microwave power P in line with the experimental observations in [6, 7] and others. This occurs at such powers that the amplitude of classical oscillations of the electron orbit center in the microwave field becomes on the order of L. The pertinent characteristic power P_{max} increases with Ω approximately as $P_{max} \propto \Omega^3$ [19]. Another consequence of the nonlinear mechanism in question is that, at high microwave powers, the magnitudes of maxima and minima corresponding to higher resonances ($\Omega \sim N\Omega_c$ with $N > 1$) are not too small compared to those near the cyclotron resonance ($\Omega \sim \Omega_c$).

Slowing down of the increase in $\max\sigma_{ph}$ and $|\min\sigma_{ph}|$ with increasing microwave power can be also associated with some heating of the 2DES. As shown below, an increase in the electron temperature leads to broadening of the LL and, consequently, to smearing of the resonances.

5. TEMPERATURE EFFECTS

As seen from (1), the microwave photoconductivity σ_{ph} markedly decreases due to the processes with emission of microwave photons. This effect becomes essential when the electron temperature increases from $T < N\hbar\Omega_c \sim \hbar\Omega$ to $T > N\hbar\Omega_c \sim \hbar\Omega$. The microwave photoconductivity maxima and minima also strongly depend on the LL broadening. The latter can be rather sensitive to the temperature. In particular, at moderate microwave powers P, for a Lorentzian shape of the LLs, one obtains the following temperature dependence:

$$\frac{\max\sigma_{ph}}{\sigma_{dark}} \simeq \frac{|\min\sigma_{ph}|}{\sigma_{dark}} \propto P\frac{1-e^{-\hbar\Omega/T}}{\Gamma^3(T)}. \qquad (4)$$

Here, the dark conductivity and photoconductivity stem from scattering processes involving impurities, while the value σ_{ph} depends on the sharpness of the resonances and, hence, on the net LL broadening. The net LL broadening is determined by the impurity (and roughness) scattering processes and by the electron–electron interaction. The LL broadening due to electron–electron interaction steeply increases with the electron temperature. Taking into account that, in the experimental situation, the 2DES Fermi energy $E_F \gg \hbar\Omega_c$, one can use the following temperature dependence [27]: $\Gamma_e(T) \propto (T/E_F)^2\ln(\sqrt{E_F Ry^*}/T)$, where Ry^* is the effective Rydberg. For $f = \Omega/2\pi = 50$ GHz, the factor associated with the emission of microwave photons in (4) reduces approximately by half with temperature increasing from 1 to 3–4 K. Setting $E_F = 10$ meV, we find that $\Gamma_e|_{T=3\,K}/\Gamma_e|_{T=1\,K} \simeq 9$. Hence, according to (4), in a 2DES with high electron mobility (in the absence of magnetic field) in which Γ is determined primarily by the electron–electron scattering so that $\Gamma \simeq \Gamma_e$, the span of the dissipative conductivity oscillations, i.e., the values $\max\sigma_{ph}$ and $|\min\sigma_{ph}|$ can decrease by several orders of magnitude when the temperature increases by a few K. However, in 2DESs with moderate electron mobility (limited, say, by residual impurities and interface roughness) in which $\Gamma_i \gtrsim \Gamma_e$, an increase in Γ with increasing temperature and, hence, a

decrease in $\max\sigma_{ph}$ and $|\min\sigma_{ph}|$ can be less pronounced, as is confirmed by experimental data.

Since photon-assisted acoustic phonon scattering provides the microwave photoconductivity maxima and minima at $N\Omega_c \lesssim M\Omega$ and $N\Omega_c \gtrsim M\Omega$, respectively, i.e., approximately at the point where photon-assisted impurity scattering yields, on the contrary, the microwave photoconductivity minima and maxima, the former mechanism can interfere with the latter, modifying the oscillations and even effectively suppressing them. This is possible if photon-assisted acoustic phonon scattering becomes essential with increasing temperature [23, 24]. A marked intensification of this mechanism occurs when $T \gtrsim \hbar s/L = T_{ac}$, where s is the speed of sound. In the experimental situations, $T_{ac} \simeq 0.5$ K.

6. EFFECT OF HIGH ELECTRON MOBILITY

Although the oscillations of microwave photoconductivity as a function of the cyclotron frequency (i.e., the magnetic field) were observed in 2DESs with electron mobility in a rather wide range, sufficiently deep microwave photoconductivity minima that can result in ANC were observed only in the samples with fairly high electron mobility. In the framework of the model under consideration, this can be explained as follows. The relative amplitude of the microwave photoconductivity oscillations is very sensitive to the LL broadening. In sufficiently perfect 2DESs with weak scattering of electrons on residual impurities immediately in the 2DES and on the interface roughness, the LL broadening is determined primarily by the electron–electron interaction. Indeed, when electron sheet concentration Σ_e is about the sheet concentration of remote impurities Σ_i, the ratio of quantities Γ_i and Γ_e can be estimated roughly as $\Gamma_i/\Gamma_e \propto (\Sigma_i/\Sigma_e)\exp(-2d_i/L)$. The exponential factor in this formula is due a spatial separation of electrons and donors, which gives rise to an exponential decrease in the matrix element of electron-impurity interaction. Hence, at $d_i > L$, one obtains $\Gamma_i \ll \Gamma_e$. In the experiments with 2DESs having high electron mobility, $d_i/L \simeq 1.4$, so that the latter exponential factor is about 0.06. Since the electron–electron scattering processes are effectively suppressed with decreasing temperature [27], the microwave maxima and, which is more important, minima are well pronounced and can surpass the dark conductivity at low temperatures and when microwave radiation is strong enough. This leads to ANC in some ranges of a magnetic field when certain relations between Ω and Ω_c are met. In contrast, in samples with moderate electron mobility, a significant contribution to the LL broadening is provided by residual impurities and interface roughness. This prevents the attainment of a sufficiently large ratio $|\min\sigma_{ph}|/\sigma_{dark}$, which is necessary for ANC.

We believe that main experimental facts on ZR- and ZC-states and related effects can be explained in the framework of the concept based on ANC caused by photon-assisted impurity scattering of electrons and affected by electron-electron and photon-assisted acoustic phonon interactions.

REFERENCES

1. H. Kroemer, Proc. IRE **47**, 231 (1959).
2. V. I. Ryzhii, JETP Lett. **7**, 28 (1968).
3. V. F. Elesin, Zh. Éksp. Teor. Fiz. **55**, 799 (1968) [Sov. Phys. JETP **28**, 410 (1969)].
4. A. D. Gladun and V. I. Ryzhii, Zh. Éksp. Teor. Fiz. **57**, 978 (1969) [Sov. Phys. JETP **30**, 534 (1970)].
5. V. I. Ryzhii, Fiz. Tverd. Tela (Leningrad) **11**, 2577 (1969) [Sov. Phys. Solid State **11**, 2078 (1970)].
6. R. G. Mani, J. H. Smet, K. von Klitzing, *et al.*, Nature **420**, 646 (2002).
7. M. A. Zudov, R. R. Du, L. N. Pfeiffer, and K. W. West, Phys. Rev. Lett. **90**, 046807 (2003).
8. C. L. Yang, M. A. Zudov, T. A. Knuuttila, *et al.*, Phys. Rev. Lett. **91**, 096803 (2003).
9. P. W. Anderson and W. F. Brinkman, cond-mat/0302129 (2003).
10. A. V. Andreev, I. L. Aleiner, and A. J. Millis, Phys. Rev. Lett. **91**, 056803 (2003).
11. F. S. Bergeret, B. Huckestein, and A. F. Volkov, Phys. Rev. B **67**, 241303 (2003).
12. V. I. Ryzhii, R. A. Suris, and B. S. Shchamkhalova, Fiz. Tekh. Poluprovodn. **20**, 2078 (1986) [Sov. Phys. Semicond. **20**, 1299 (1986)].
13. A. L. Zakharov, Zh. Éksp. Teor. Fiz. **38**, 665 (1960) [Sov. Phys. JETP **11**, 478 (1960)].
14. S. I. Dorozhkin, JETP Lett. **77**, 577 (2003).
15. S. A. Studenikin, M. Potemski, P. T. Coleridge, *et al.*, Solid State Commun. **129**, 314 (2003).
16. R. G. Mani, J. H. Smet, K. von Klitzing, *et al.*, Phys. Rev. B **69**, 161306 (2004).
17. R. L. Willett, L. N. Pfeiffer, and K. W. West, Phys. Rev. Lett. **93**, 026804 (2004).
18. A. C. Durst, S. Sachdev, N. Read, and S. M. Girvin, Phys. Rev. Lett. **91**, 086803 (2003).
19. V. Ryzhii and R. Suris, J. Phys.: Condens. Matter **15**, 6855 (2003).
20. X. C. Lei and S. Y. Liu, Phys. Rev. Lett. **91**, 226805 (2003).
21. M. G. Vavilov and I. L. Aleiner, Phys. Rev. B **69**, 035303 (2004).
22. V. Shikin, JETP Lett. **77**, 236 (2003).
23. V. Ryzhii and V. Vyurkov, Phys. Rev. B **68**, 165406 (2003).
24. V. Ryzhii, Phys. Rev. B **68**, 193402 (2003).
25. R. Fitzgerald, Phys. Today **56**, 24 (2003).
26. A. C. Durst and S. M. Girvin, Science **304**, 1752 (2004).
27. A. V. Chaplik, Zh. Éksp. Teor. Fiz. **60**, 1845 (1971) [Sov. Phys. JETP **33**, 997 (1971)].

JETP Letters, Vol. 80, No. 5, 2004, pp. 367–370. From Pis'ma v Zhurnal Éksperimental'noĭ i Teoreticheskoĭ Fiziki, Vol. 80, No. 5, 2004, pp. 416–419.

State-Dependent Dynamical Variables in Quantum Theory¶

P. Leifer

Cathedra of Informatics, Crimea State Engineering and Pedagogical University, Simferopol, Crimea, 95015 Ukraine

Received March 18, 2004; in final form, July 22, 2004

State-dependent local dynamical variables (LDVs) sharply differ from the ordinary operators of quantum mechanics. The N-level model system shows the physical importance of such operators in the complex projective Hilbert state space $CP(N-1)$. The process of quantum measurement in terms of LDVs is described. © *2004 MAIK "Nauka/Interperiodica".*

PACS numbers: 03.65.-w

In our macroscopic experience, we have a solid pseudo-Euclidian space-time structure. The physical conservation laws have rid us from doubts about the identifying the macroscopic system. The identification of the quantum system at very short and at cosmic distances is not so simple. How may one be sure that, say, a right helicity photon has been send by Alice? Physically, this question may be formulated as follows: what is an objective criterion for the identity of a quantum system, or, what is the physical mechanism of the self-identification (self-conservation) of a quantum system? We can no longer rely upon space-time symmetries, since it is just these properties that should be established in some approximation *a posteriori*. In such a situation, one should have conservation laws relying upon the geometry of the intrinsic transformation groups and its submanifolds.

I formulate the covariant dynamics of an N-level quantum system and corresponding local dynamical variables (LDVs) based purely on the $SU(N)$ geometry. Since the quantum states are rays, in fact, only transformations from the coset submanifold $G/H = U(N)/U(1) \times U(N-1) = CP(N-1)$ act effectively on the rays of states. However, LDVs (defined in terms of tangent vectors to $CP(N-1)$) being expressed in terms of local quantum coordinates ($\pi^1 = \Psi^1/\Psi^0, \ldots, \pi^{N-1} = \Psi^{N-1}/\Psi^0$) are subject to the action of the whole $SU(N)$ group. Hence, we may assume that $SU(N)$ transformations of the N-level quantum system are locally equivalent to a definite motion of the LDVs in $CP(N-1)$ (the "superrelativity" principle [1]). Therefore parallel transport in $CP(N-1)$ is the method of N-level quantum system identification, expressing the conservation law of the LDV, should be observable and curvature-dependent.

1. I would like attract attention to the global property of the internal symmetries in quantum mechanics. They have been realized mostly in imitation of the form of space-time symmetries; namely, their operators give a linear representation of the corresponding groups. To my mind, the nonlinear realization seems to be actually capable of shedding light on the measurement as an objective process [2].

In fact, nonlinear group realizations have been already used in the framework of the phenomenological Lagrangians method in QFT [3] and in the theory of spin wave interaction [4]. The breakdown of the "chiral" dynamical group $SU(N)$ up to the isotropy group $H = U(1) \times U(N-1)$ has been proposed [1], but in an abstract form without clear physical argumentation. I will now show that, in simple optical measurements, the state-dependent LDVs play the key role in the objective interpretation of quantum theory.

My aim is to calculate the phase difference accumulated during the parallel transport of LDVs corresponding to light polarization along different paths in $CP(1)$. Let me describe the polarization optics measurement in terms of LDVs. The model setup providing the unitary evolution of the polarization state of light is simple. A fixed Cartesian reference frame (O, x, y, z) in physical space will be used. Initially, one has a beam of light in a linear polarization state in the x-direction $|x\rangle = \frac{1}{\sqrt{2}}(|R\rangle + |L\rangle) = \frac{1}{\sqrt{2}}(1, 1)^T$ propagating along the z-axis. Then the polarization states in the y-direction is $|y\rangle = \frac{-i}{\sqrt{2}}(|R\rangle - |L\rangle) = \frac{1}{\sqrt{2}}(-i, i)^T$ and, then, $|R\rangle = (1, 0)^T$, $|L\rangle = (0, 1)^T$. The coherent superposition state will be denoted, as usual, as $|\Psi\rangle = (\Psi^0, \Psi^1)^T$. The Poincaré sphere refers to the coordinates (o, s_1, s_2, s_3) in the isospace of the polarization. In general, the coherence vector lies on the isotropy "light cone" $s_0^2 - s_1^2 - s_2^2 - s_3^2 = 0$, where $s_0^2 = I^2 = \langle\Psi|\Psi\rangle$ is the square of the beam intensity. It means the coherence vector may fall into the Poincaré sphere under nonunitary evolution. I will restrict myself to the unitary one.

The initial state $|x\rangle$ is modulated passing through an optically active medium (say using the Faraday effect

¶ This article was submitted by the author in English.

in YIG film magnetized along the main axes in the *z*-direction by a harmonic magnetic field with frequency Ω and angle amplitude β). Formally, this process may be described by the action of the unitary matrix $\hat{h}_{os_3}$ belonging to the isotropy group of $|R\rangle$ [1]. Then, the coherence vector will oscillate along the equator of the Poincaré sphere. The next step is the dragging of the oscillating state $|x'(t)\rangle = \hat{h}_{os_3}|x\rangle$ with frequency ω up to the "north pole" corresponding to the state $|R\rangle$. In fact, this is the motion of the coherence vector. This may be achieved by the variation of the azimuth of the linear polarized state from $\theta/2 = -\pi/4$ up to $\pi/4$ with help of a dense flint of appropriate length embedded into the sweeping magnetic field. Further, this beam should pass the $\lambda/4$ plate. This process of variation of the ellipticity of the polarization ellipse may be described by the unitary matrix $\hat{b}_{os'_1}$ belonging to the coset homogeneous submanifold $U(2)/U(1) \times U(1) = CP(1)$ of the dynamical group $U(2)$ [1]. This dragging without modulation leads to the evolution of the initial state along the geodesic of $CP(1)$, and the trace of the coherent vector is the meridian of the Poincaré sphere between the equator and one of the poles. The modulation deforms both the geodesic and the corresponding trace of the coherence vector on the Poincaré sphere during such unitary evolution.

The action of the $\lambda/4$ plate depends upon the state of the incoming beam state (the relative orientation of the fast axes of the plate and the polarization of the beam). Furthermore, only relative phases and amplitudes of photons in the beam have a physical meaning for the $\lambda/4$ plate. Neither the absolute amplitude (intensity of the beam) nor the general phase affect the polarization character of the outgoing state. It means that the device action depends only upon the local coordinates $\pi^1 = \Psi^1/\Psi^0 \in CP(1)$. Small relative re-orientation of the $\lambda/4$ plate leads to a small variation of the outgoing state. This means that the $\lambda/4$ plate reorientation generates the tangent vector to $CP(1)$. It is natural to discuss the two components of such a vector: velocities of the variations of the ellipticity and of the azimuth (inclination) angle of the polarization ellipse. These are examples of LDVs. The comparison of such dynamical variables for different coherent states requires that affine parallel transport agrees with the Fubini-Study metric. The deep reason for this is as follows.

2. Let us assume that the initial state is $(\pi_A^1, \ldots, \pi_A^{N-1})$ and the final state is $(\pi_B^1, \ldots, \pi_B^{N-1})$. The state $(\pi_B^1, \ldots, \pi_B^{N-1})$ may be reached from any different state $(\pi_{A'}^1, \ldots, \pi_{A'}^{N-1})$. In order to know the source of this state, there should be some mark or "key." This may be achieved by establishing a set of constraints that an observer agrees are "good enough" for the identification. Here, we have a subjective factor. But this may be avoided if we chose *intrinsic invariants* of the $CP(N-1)$ geometry. Then, the subjective element will disappear and, hence, one will have an objective criterion for the identification. Formally, it is based upon Cartan's method of moving a frame, which eliminates the necessity of a "second particle" as a reference frame for the "first" one [5]. Generally, the "minimally full" description of the quantum state in $CP(N-1)$ requires the adjoint representation of $SU(N)$ in the R^{N^2-1} field parameter space. In fact, these effective multipole fields describe the intensity of the device's action. The tangent vector fields (differential operators) $D_\alpha = \Phi_\alpha^i \dfrac{\partial}{\partial \pi^i} +$ c.c., where Φ_α^i, are as follows:

$$\Phi_\sigma^i = \lim_{\varepsilon \to 0} \varepsilon^{-1} \left\{ \frac{[\exp(i\varepsilon\lambda_\sigma)]_m^i \Psi^m}{[\exp(i\varepsilon\lambda_\sigma)]_m^j \Psi^m} - \frac{\Psi^i}{\Psi^j} \right\} = \lim_{\varepsilon \to 0} \varepsilon^{-1} \{\pi^i(\varepsilon\lambda_\sigma) - \pi^i\}. \quad (1)$$

These vector fields replace, in my approach, the Pauli matrices of $AlgSU(2)$, the Gell–Mann matrices of $AlgSU(3)$, etc. [1]. The LDVs are state-dependent, i.e., local in $CP(N-1)$, and their expectation values (the scalar product in the sense of the Fubini-Study metric) are not bilinear in general. Such expectation values are similar to an expectation value in the modified quantum mechanics of Weinberg [6]. The path-dependent parallel transport of the LDV in the affine connection

$$\Gamma_{mn}^i = \frac{1}{2} G^{ip^*} \left(\frac{\partial G_{mp^*}}{\partial \pi^n} + \frac{\partial G_{p^*n}}{\partial \pi^m} \right) = -\kappa \frac{\delta_m^i \pi^{n^*} + \delta_n^i \pi^{m^*}}{1 + \kappa \sum |\pi^s|^2} \quad (2)$$

agrees with the Kählerian metric (Fubini-Study metric)

$$G_{ik^*} = \frac{(1 + \kappa \sum |\pi^s|^2)\delta_{ik} - \kappa \pi^{i^*} \pi^k}{(1 + \kappa \sum |\pi^s|^2)^2}, \quad (3)$$

as will be shown in the case of $CP(1)$. Here, $\kappa = r^{-2}$ is the curvature of the sphere serving as a model of $CP(N-1)$ through the stereographic projection. I will assume, temporarily and for simplicity, that $r = 1$.

The essential differences between my approach and, say, the approach of Anandan and Pati [7] are, first, that I use the parallel transport of dynamical variables local in $CP(1)$ instead of the quantum state parallel transport. Second, the geometric frequency I use is local and applicable to any superposition state, whereas the Anandan–Pati "reference section" of the state is bilocal and singular for the orthogonal initial and final states. Note that Berry's [8, 9] and the Aharonov–Anandan [10, 11] "parallel transport" laws of the quantum state are defined in original Hilbert space. This kind of parallel transport is not an object of the intrinsic geometry of a parameter space (Berry) or the projective Hilbert

state spaces (Aharonov–Anandan); see, for example, the explanation in [12]. Such a definition discards the dynamical phase shift and extracts the pure topological consequences of the rotations of polarizers, $\lambda/4$ plates, etc. However, there are some reasons to keep dynamics with geometry [10, 1, 13]. In particular, the fundamental importance of the complex projective geometry of the state space $CP(N-1)$ [11, 14, 2, 1, 15, 13] strongly suggests working in the intrinsic geometry of $CP(N-1)$ associated with quantum dynamics.

3. Now, I introduce parallel transport of real dynamical variable $T = T^1 \frac{\partial}{\partial \pi^1} + T^{1*} \frac{\partial}{\partial \pi^{1*}}$, $T^{1*} = (T^1)^*$, assuming that T^1 obeys the equations

$$\frac{dT^1}{dt} + \Gamma^1_{11} T^1 \frac{d\pi^1}{dt} = 0, \quad \text{c.c.} \tag{4}$$

These equations have exact solutions along a geodesic of $CP(1)$: $T^1(s) = \xi(1 + \tan^2(\omega t)) + i\eta(1 + \tan^2(\omega t))$. The scalar product $G_{ik*} T^i(s) T^{k*}(s) = \xi^2 + \eta^2$ is the invariant of the parallel transport.

The modulation of the polarization plane orientation deforms the geodesic $\gamma(t)$ to $f(t)$. Equations (4) have, for such a path of parallel transport, only the numerical solutions, which we shall call $\Xi^1(t)$, c.c. Allow me to show the difference between the parallel transported vectors $T^1(s)$ along the geodesic $\gamma(t)$ and the vector $S^1 = \Xi^1 - \Gamma^1_{11} \Xi^1 d\pi^1$ pointwise "shifted" from the deformed path $f(t)$ to the "reference" geodesic $\gamma(t)$ where $d\pi^1 = \pi^1(f(t)) - \pi^1(\gamma(t))$. It means all local tensors and Γ^p_{in} were calculated on the "reference" geodesic. The angle between these two vectors along the "reference" geodesic will be expressed through $\cos\chi(t)$:

$$\cos\chi(t) = \frac{\left| G_{ik*} T^i(\gamma(t)) S^{k*}(f(t)) \right|}{\|T\| \|S\|}. \tag{5}$$

The cosine of the angle between the exact solution of the equation $T^i(\gamma(t))$ and the numerical solution $\Xi^{k*}(f(t))$ for the parallel transport along the deformed geodesic is shown in Fig. 1.

The result is very interesting: *all parallel vectors transported along different paths look like a smoothly opening "umbrella" along the geodesic. At $\theta = \pi/2$, the parallel transported dynamical variable along one of the deformed geodesies f(t) are orthogonal (in the sense of the Fubini-Study metric) to the "handle" of the "umbrella"; the parallel transported vector along the geodesic. In fact this means that the result of the parallel transport is local: this is uniquely defined by the geodesic issuing from the initial point and by the dynamical variable (tangent vector). It seems to be a preliminary conclusion, like a "decoherence process" in the projective Hilbert state space.*

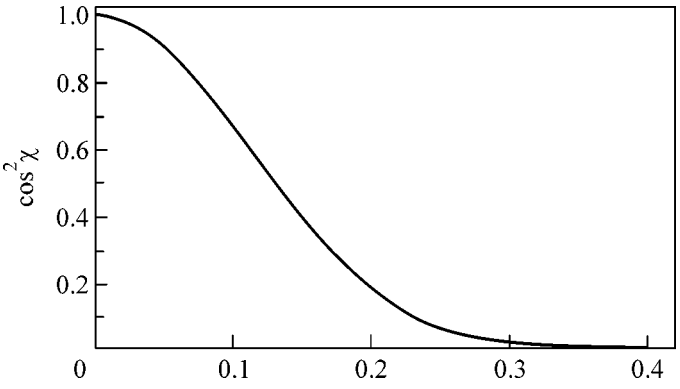

Fig. 1. The square of the cosine of the observable angle between two parallel transported vectors along the geodesic $\gamma(0, \pi/2)$ and deformed geodesic $f(0, \pi/2)$ against the angle length in radians of the geodesic. The relationship between frequencies is as follows: $\Omega = 10\pi$ radians/s, $\omega = \pi$ rad/s.

Let me briefly consider the expected phase modulation shift accumulated during the parallel transport of the velocities of the ellipticity and the inclination angle in the real experiment described in Section 1. The key role belongs to the curvature κ, which I put equal to 1 in previous formulas. Now, I assume that curvature of the state space $CP(N-1)$ is the measure of the correlations between the different LDVs. Volkov *et al.* used sphere curvature as a phenomenological constant of spin wave interaction [4]. I set the curvature as the fine structure constant $\kappa = e^2/\hbar c \approx 0.007$. The reason for this choice will be discussed elsewhere. If the modulation frequency $\Omega = 4000\pi$ radians/s has the angle amplitude $\beta = 0.017$ radians and the dragging frequency $\omega = 10\pi$ rad/s, the behavior of the velocities of the ellipticity and the azimuth angle is shown in Figs. 2 and 3.

All the LDVs discussed assume that the velocity of ellipticity ϵ variation is measurable. Since, now, $\frac{d\epsilon}{dt}$ is curvature-dependent, it differs from the "flat" parallel transport. Then, the instant frequency (the speed of the modulation phase variation) is a function of θ and ϵ and it should contain, besides the frequencies ω and $\beta\Omega$, the frequency $\kappa\beta\Omega$. It would be interesting to measure it in an experiment. The modulation frequency to this aim should be essentially higher than I used in my calculations.

The topological character of the Berry [8, 9], Aharonov–Anandan [10, 11],and Wilczek–Zee [16] phases arises as a macroscopic environmental reaction on the quantum dynamics of an "immersed" quantum system. The anholonomies of the "parallel transport" of the state vector are expressed as some effective gauge fields reflecting the topological character of the transformation groups of orientations of macroscopic elements (polarizers, $\lambda/4$ plates, etc.) of the quantum setup. Therefore, it is not so strange that there are close classical analogies of the topological phases in classical

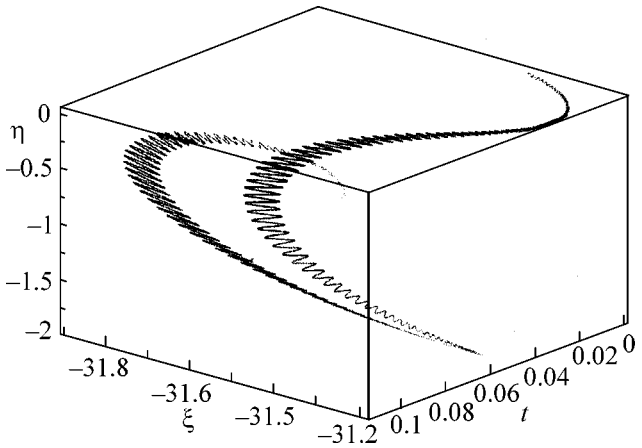

Fig. 2. The time dependence of the ellipticity velocity. Initial conditions: $\xi = \Re(d\epsilon/dt) = -31.4$ radians/s and $\eta = \Im(d\epsilon/dt) = 0$.

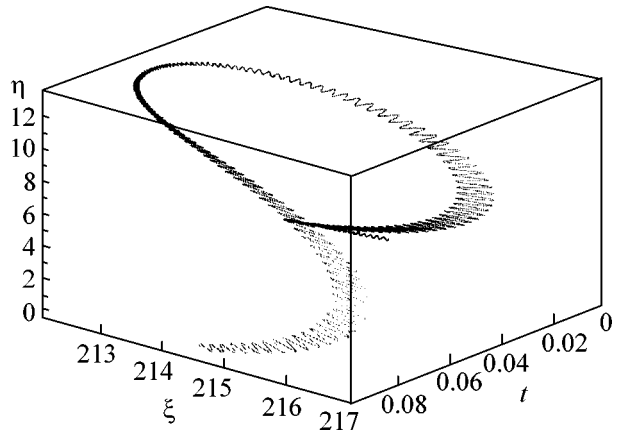

Fig. 3. The time dependence of the azimuth angle velocity. Initial conditions: $\xi = \Re(d\theta/dt) = 213.5$ rad/s and $\eta = \Im(d\theta/dt) = 0$.

physics (e.g., the Hannay angle [9]). This is the reason the dynamic phase should be discarded in order to get a definite geometric (topological) phase. Therefore, in general, it is impossible, of course, to define these gauge fields in some fundamental sense. But such gauge fields may be truly fundamental in two important cases of the complex projective state space $CP(N-1)$. First, since we believe that rays of quantum states are the fundamental notions at any level. Second, $CP(1)$ may be treated as the Qubit coherent state space under quantum information processing. In these cases, there arises a new geometro-dynamics phase that relates to the affine gauge field. The corresponding gauge fields associated with the curvature of $CP(N-1)$ are state-dependent and realize the local gauge transformation of the moving quantum frame in $CP(N-1)$ [1, 15, 13, 17]. They are akin to the Wilczek–Shapere gauge fields related to the problem of a deformable body in fluid [18].

I sincerely thank Yakir Aharonov for the discussion of nonlinear modification of quantum theory and Larry Horwitz for numerous useful discussions and notes.

REFERENCES

1. P. Leifer, Found. Phys. **27**, 261 (1997).
2. K. R. W. Jones, Aust. J. Phys. **48**, 1055 (1995).
3. S. Coleman, I. Wess, and B. Zumino, Phys. Rev. **177**, 2239 (1969).
4. D. V. Volkov, A. A. Zjeltuchin, and Yu. P. Blioch, Solid State Phys. **13**, 1668 (1971).
5. Y. Aharonov *et al.*, quant-ph/9708043 v2.
6. S. Weinberg, Ann. Phys. (N.Y.) **194**, 336 (1989).
7. J. S. Anandan and A. K. Pati, Phys. Lett. A **231**, 29 (1997).
8. M. V. Berry, Proc. R. Soc. London, Ser. A **392** (2), 45 (1984).
9. M. V. Berry, in *Geometric Phases in Physics*, Ed. by A. Shapere and F. Wilczek (World Sci., Singapore, 1989), pp. 7–28.
10. Y. Aharonov and J. Anandan, Phys. Rev. Lett. **58**, 1593 (1987).
11. J. Anandan and Y. Aharonov, Phys. Rev. D **38**, 1863 (1988).
12. J. Anandan and L. Stodolsky, quant-ph/9908046.
13. P. Leifer, gr-qc/0201039.
14. L. P. Hughston, Proc. R. Soc. London, Ser. A **452**, 953 (1996).
15. P. Leifer, Found. Phys. Lett. **11**, 233 (1998).
16. F. Wilczek and A. Zee, Phys. Rev. Lett. **52**, 2111 (1984).
17. P. Leifer, physics/0404136.
18. A. Shapere and F. Wilczek, J. Fluid Mech. **198**, 557 (1989).